



UPPSALA
UNIVERSITET

*Digital Comprehensive Summaries of Uppsala Dissertations
from the Faculty of Science and Technology 2222*

Designing multicomponent alloy coatings for corrosion protection

LEÓN ZENDEJAS MEDINA



ACTA
UNIVERSITATIS
UPSALIENSIS
UPPSALA
2023

ISSN 1651-6214
ISBN 978-91-513-1670-3
URN urn:nbn:se:uu:diva-489916

Dissertation presented at Uppsala University to be publicly examined in Polhemsalen, Ångströmlaboratoriet, Lagerhyddsvägen 1, Uppsala, Friday, 3 February 2023 at 09:15 for the degree of Doctor of Philosophy. The examination will be conducted in English. Faculty examiner: Professor Zoe Barber (Downing College, Cambridge, UK).

Abstract

Zendejas Medina, L. 2023. Designing multicomponent alloy coatings for corrosion protection. *Digital Comprehensive Summaries of Uppsala Dissertations from the Faculty of Science and Technology* 2222. 117 pp. Uppsala: Acta Universitatis Upsaliensis. ISBN 978-91-513-1670-3.

This thesis explores the design of metallic coatings for corrosion protection. The subject of the study was the new class of materials multicomponent alloys (MCAs, also known as high entropy alloys). They consist of near-equal concentrations of many (four or more) metals and are often reported to form a single phase with a simple crystal structure. Due to the complexity and range of possible MCA compositions, there is a need for design principles as guidelines for how the alloying elements can be chosen and combined. This work aimed at finding such principles through the systematic study of the synthesis and properties of three MCA systems. Their compositions were carefully chosen to answer fundamental questions about the materials class and the synthesis method and to generate conclusions that could be generalized to a larger group of MCAs. All three systems were based on the elements Cr, Fe, and Ni, and can therefore be considered an extension of stainless steels.

The first alloy was CoCrFeMnNi, which is well-known as a single-phase bulk MCA. A systematic exploration of the synthesis parameters showed that there are fundamental differences in the phase formation of CoCrFeMnNi through magnetron sputtering compared to typical bulk synthesis. Literature studies revealed that this conclusion can be generalized; single-phase MCAs should not necessarily be expected from magnetron sputtering. It was also shown that the choice of substrate and even the crystal orientation of the individual substrate grains strongly influenced the outcomes of synthesis, including the phase formation, growth rate, morphology, and the formation of stacking fault structures.

Two novel alloy systems were also explored: CrFeNiTa and CrFeNiW. Ta and W were added to achieve an alloy with higher corrosion resistance than stainless steels and more generally, to examine the interplay between passivating elements in MCAs during corrosion. Based on geometrical considerations, it was predicted that equal amounts of Ta and W would be needed to protect alloys from corroding (less than 20 at%). It was found that the prediction was only valid for the CrFeNiTa alloy system. The reason behind this was explored and a new criterion was then proposed: In an MCA, each passivating element should have similar electrochemical nobility.

Further design possibilities were demonstrated by adding up to 50 at% carbon to the alloys. Thermodynamic calculations predicted decomposition into multiple metallic and carbide phases. However, the limited diffusion during magnetron sputtering suppressed the segregation. At lower carbon contents, the carbon-containing alloys were single-phase and amorphous. At higher carbon contents they formed alloy/amorphous carbon nanocomposites. The addition of carbon made the alloys stronger, more corrosion resistant, and more crack resistant.

Keywords: corrosion, thin films, coatings, magnetron sputtering, high entropy alloy, percolation theory, mechanical tests

León Zendejas Medina, Department of Chemistry - Ångström, Inorganic Chemistry, Box 538, Uppsala University, SE-751 21 Uppsala, Sweden.

© León Zendejas Medina 2023

ISSN 1651-6214

ISBN 978-91-513-1670-3

URN urn:nbn:se:uu:diva-489916 (<http://urn.kb.se/resolve?urn=urn:nbn:se:uu:diva-489916>)

*Till Helena V. och Anna-Lena R. L.,
mina bästa lärare*

List of Papers

This thesis is based on the following papers, which are referred to in the text by their Roman numerals.

- I Phase formation in magnetron sputtered CrMnFeCoNi high entropy alloy**
León Zendejas Medina, Lars Riekehr, Ulf Jansson
Surface and Coatings Technology, 403:126323, 2020
- II Magnetron sputtering of the high entropy alloy CoCrFeMnNi on 316L: Influence of substrate grain orientation**
Anna Jansson, **León Zendejas Medina**, Lisa Lautrup, Ulf Jansson
In manuscript
- III Extending the passive region of CrFeNi-based high entropy alloys by including Ta or W**
León Zendejas Medina, Live Mølmen, Eirini-Maria Paschalidou, Olivier Donzel-Gargand, Peter Leisner, Ulf Jansson, Leif Nyholm
In manuscript
- IV Elemental distribution in carbon-supersaturated high entropy alloy coatings: A synchrotron-based study**
León Zendejas Medina, Olivier Donzel-Gargand, Kristina von Fieandt, Erik Lewin, Ulf Jansson, Rebecka Lindblad
In manuscript
- V Enhancing corrosion resistance, hardness, and crack resistance in sputtered high entropy CoCrFeMnNi coatings by adding carbon**
León Zendejas Medina, Marcus V. Tavares da Costa, Eirini-Maria Paschalidou, Greta Lindwall, Lars Riekehr, Markus Korvela, Stefan Fritze, Szilárd Kolozsvári, E. Kristoffer Gamstedt, Leif Nyholm, Ulf Jansson
Materials & Design 205, 109711, 2021

VI Corrosion studies on multicomponent CoCrFeMnNi (C) thin films in acidic environments

Eirini-Maria Paschalidou, Rebecka Lindblad, **Leon Zendejas Medina**, Dennis Karlsson, Ulf Jansson, Leif Nyholm.

Electrochimica Acta 404, 139756, 2022

VII High entropy alloy/carbon nanocomposites: Influence of carbon on the mechanical properties and corrosion resistance

León Zendejas Medina, Marcus V. Tavares da Costa, Olivier Donzel-Gargand, E. Kristoffer Gamstedt, Leif Nyholm, Ulf Jansson

In manuscript

Comments on my contributions to the papers

The results presented in this thesis are the products of teamwork. I was responsible for some of the theoretical work, including the thermodynamic calculations and calculations based on the percolation theory. I synthesized all the included samples and performed most of the characterization including the data analysis. I also performed and analyzed parts of the mechanical and corrosion tests. In Papers **I**, **III**, **V**, and **VII**, I was responsible for planning the study, performing most of the experiments and writing the manuscript. In Papers **II** and **IV**, I planned the study, executed the work, and wrote the article in collaboration with a co-author. Finally, in Paper **VI**, I provided the samples, took part in the discussions, contributed with some analysis, and wrote part of the article.

Comments on the unpublished manuscripts

In Paper **VII**, the mechanical model will be refined to better describe the behavior of the nanocomposite coatings. Papers **II**, **III** and **IV** are in their final form and ready for submitting.

Disclaimer: Parts of the thesis are based on my licentiate thesis entitled *Magnetron sputtered high entropy alloy coatings and the effects of adding carbon* (Uppsala University, 2021)

Papers not included in the thesis

1. **Accurate high-resolution depth profiling of magnetron sputtered transition metal alloy films containing light species: A multi-method approach.**
Marcos Moro, Radek Holeňák, **León Zendejas Medina**, Ulf Jansson, Daniel Primetzhofer
Thin Solid Films, 686:137416, 2019
2. **Combined in-situ ion beam analysis and thermal desorption spectroscopy for studying deuterium retention in tungsten**
K Kantre, PS Szabo, Marcos V Moro, C Cupak, R Stadlmayr, **L Zendejas Medina**, F Aumayr, Daniel Primetzhofer
Physica Scripta 96 (12), 124004, 2021
3. **Hard x-ray photoelectron spectroscopy: a snapshot of the state-of-the-art in 2020**
Curran Kalha, Nathalie K Fernando, Prajna Bhatt, Fredrik OL Johansson, Andreas Lindblad, Håkan Rensmo, **León Zendejas Medina**, Rebecka Lindblad, Sebastian Siol, Lars PH Jeurgens, Claudia Cancellieri, Kai Rossnagel, Katerina Medjanik, Gerd Schönhense, Marc Simon, Alexander X Gray, Slavomír Nemšák, Patrick Lömker, Christoph Schlueter, Anna Regoutz
Journal of Physics: Condensed Matter 33 (23), 233001, 2021

Contents

| | |
|--|----|
| Chapter 1. Introduction | 13 |
| Chapter 2. Magnetron sputter deposition..... | 15 |
| Chapter 3. Multicomponent materials..... | 17 |
| 3.1 High entropy alloys | 17 |
| 3.1.1 Criteria for single-phase formation..... | 18 |
| 3.1.2 Multi-phase and amorphous high entropy alloys..... | 18 |
| 3.1.1 Notes on the definition of high entropy alloys | 21 |
| 3.2 The Cantor alloy and 3d transition metal MCAs..... | 21 |
| 3.3 Adding carbon to MCAs | 23 |
| 3.4 Why should we study MCA coatings? | 24 |
| Chapter 4. Aim and scope..... | 26 |
| Chapter 5. Methods..... | 29 |
| 5.1 Thermodynamic calculations | 29 |
| 5.2 Synthesis..... | 29 |
| 5.3 Materials characterization | 30 |
| 5.4 Testing of material properties..... | 33 |
| 5.4.1 Corrosion testing..... | 33 |
| 5.4.2. Mechanical testing of coatings | 35 |
| 5.4.3. Interfacial contact resistance..... | 36 |
| Chapter 6. Synthesis of multicomponent coatings..... | 37 |
| 6.1. Controlling the phase formation in sputtered HEAs | 37 |
| 6.1.1 Effect of process conditions..... | 37 |
| 6.1.2. Phase formation mechanisms | 40 |
| 6.1.3. Literature review: Single-phase or multi-phase formation in magnetron sputtered multicomponent alloys..... | 42 |
| 6.1.4. The effect of the substrate on phase formation..... | 44 |
| 6.1.5. Depositing the Cantor alloy on stainless steel – a study of surface energies, growth modes, and stacking faults..... | 47 |
| 6.2. Synthesis of amorphous multicomponent alloys..... | 59 |
| 6. 3. Adding carbon to multicomponent alloys | 61 |
| 6.3.1. Thermodynamic calculations..... | 61 |
| 6.3.2. Amorphization and formation of composite coatings..... | 62 |
| Chapter 7. Tuning the properties of multicomponent materials | 66 |
| 7.1. Designing corrosion resistant alloys..... | 66 |
| 7.1.1. Passivation of metals and alloys | 66 |

| | |
|---|-----|
| 7.1.2. Using a percolation model to design passivating alloys | 67 |
| 7.1.3 Multicomponent alloys with a single passivating element | 71 |
| 7.1.4. Extending the passive region with a second passivating element..... | 72 |
| 7.1.5. Summarizing comments on passivation in MCAs..... | 74 |
| 7.2. The corrosion in bulk samples and coatings..... | 76 |
| 7.3 Corrosion of alloys modified with carbon..... | 77 |
| 7.3.1. The effect of carbon in the amorphous regime | 78 |
| 7.3.2. The effect of carbon in composite coatings | 81 |
| 7.4. Tuning the mechanical properties | 82 |
| 7.4.1. The unusually high hardness of magnetron sputtered coatings . | 82 |
| 7.4.2. The effect of carbon addition on the mechanical properties | 83 |
| 7.4.3. Decreased plasticity in annealed amorphous alloys..... | 86 |
| Conclusions and future work | 91 |
| Populärvetenskaplig sammanfattning | 94 |
| Acknowledgments..... | 97 |
| References..... | 98 |
| Appendix. Literature review | 110 |

Abbreviations

a-C – amorphous carbon
AFM – atomic force microscopy
a.u. – arbitrary unit
bcc – body-centered cubic
CALPHAD – calculation of phase diagrams
ccp – cubic close-packed
EBSD – electron backscatter diffraction
EDS/EDX – energy-dispersive X-ray spectroscopy
EIS – electrochemical impedance spectroscopy
ERDA – elastic recoil detection analysis
fcc – face-centered cubic
GFA – glass forming ability
GI-XRD – grazing-incidence X-ray diffraction
HAADF – high-angle annular dark-field
HEA – high entropy alloy
ICP-MS – inductively coupled plasma-mass spectrometry
ICR – interfacial contact resistance
IPF – inverse pole figure
LSV – linear sweep voltammetry
MCA – multi-component alloy
NN – nearest neighbor
OCP – open circuit potential
PDP – potentiodynamic polarization
RT – room temperature
SAED – selected area electron diffraction
SEM – scanning electron microscopy
SFE – stacking fault energy
STEM – scanning transmission electron microscopy
SZM – structure zone model
TEM – transmission electron microscopy
TKD – transmission Kikuchi diffraction
XPS – X-ray photoelectron spectroscopy
XRD – X-ray diffraction

Chapter 1. Introduction

In fall of 2022, Europe is facing an historic energy crisis. A transition to domestic energy production is necessary, and meanwhile, clean energy goals are endangered. At the same time, France, a global leader in nuclear power, has been forced to shut down 12 of its 54 reactors due to an age-old problem: corrosion. Stainless steel pipes carrying vital cooling water had begun to crack from stress corrosion, threatening the integrity of the core. [1–3]

Corrosion is the degradation of a material through (electro)chemical reactions with its environment. For metallic materials, corrosion is caused by the oxidation of the metal, which is spontaneous (except for gold) in the presence of air or water. The process cannot be stopped, only slowed down. This means that all alloys are affected by corrosion to some extent and corrosion needs to be considered when constructing components or infrastructure, from the selection of materials to the final design.

The impact of corrosion on society comes in many forms. It can, among other things, decrease the life time of components, lead to loss of material, and cause unreliable and delayed production of goods or energy [4]. Corrosion can sometimes result in a slow degradation of the performance of a component. In other cases, the failure is sudden and unexpected, especially when coupled with mechanical failure (there is no shortage of examples of corrosion-related accidents [5]). It is clear that the design of corrosion protection should not come as an afterthought in materials research; it must be studied and optimized in parallel with other desired properties.

Furthermore, materials design for corrosion protection requires knowledge of more than just the electrochemical reactions at the surface. An understanding of the material is necessary, including knowledge of its phase formation, control of microstructure, mechanical properties, and thermal stability. Steels, for example, are some of the most important technical alloys. They are cheap, have high strength, and can easily be processed in large volumes. Stainless steel is alloyed with Cr, which is known to form Cr-rich oxides that cover the surface of the alloy and slow down its dissolution compared to pure iron or carbon steels. But stainless steels are also highly vulnerable to certain environments. The steel used in the nuclear reactors mentioned above failed because of a specific combination of circumstances: heat from welding that caused a change in the microstructure, the mechanical stress on the pipes, and the corrosive aqueous environment [6]. This resulted in the unexpected failure

of a steel that has satisfactory corrosion performance in other environments [3].

The development of corrosion resistant materials must not only improve current technology but also meet new criteria as technology progresses, for example, to reduce the reliance on fossil fuels. The development of hydrogen as an energy source includes improving electrolyzers and fuel cells to not only be effective and safe but also cheap and with a long enough lifetime to compete with the combustion engine alternative. The internal components in fuel cells, which should ideally be metallic to decrease production costs [7], are subjected to highly corrosive environments, for example, a low pH or high potential. Finding materials that suit these applications is a new challenge.

This work is on the materials design of corrosion resistant alloys. The chosen material compositions will be synthesized as coatings with thicknesses in the scale of hundreds of nanometers that can be used on many substrates. The use of coatings over bulk materials has multiple advantages. Since the amount of used materials is smaller, the composition can be chosen more freely, given that economic factors and problems with supply are not as critical. Another benefit is the fact that the properties of the substrate and the coating can be chosen separately, and thus be better optimized for the application. The focus of the work will be on finding the parameters with which the material properties can be tuned in general. However, certain properties will be prioritized for the intended applications, which are electrodes and current collectors in acidic, and/or high-voltage environments. The mechanical properties will be evaluated in parallel with the corrosion resistance. Here, the aim will be to improve the ability of the coatings to be produced on a large scale, for example in roll-to-roll production of coatings on metallic foils. This means that the coatings should be ductile enough to deform without severe failure through cracking and hard enough to resist wear.

The subject of the study will be a new class of materials: high entropy alloys (HEAs), also known as multicomponent alloys (MCAs). These alloys, which are mixtures of many metals at near-equal concentrations, were discovered in 2004 [8,9] and opened up a vast space of unexplored alloy compositions. HEAs offer the prospect of new materials with useful qualities. But because of the range of possible compositions, it is vital to establish principles for choosing the alloying elements and tuning their concentrations to achieve specific desired properties. The chosen synthesis method, which will be in focus throughout the thesis, is magnetron sputter deposition. It is an excellent method for depositing coatings with complex compositions. The next two chapters will provide the necessary background on the synthesis technique and the chosen class of materials.

Chapter 2. Magnetron sputter deposition

Magnetron sputtering is a synthesis method for depositing coatings from the gas phase. The principles of the method are illustrated in Figure 1. Atoms are ejected from a target (source) material by accelerated ions in a magnetron plasma. The target atoms then make their way to the surface of a substrate, where a coating (or film¹) will grow. By using multiple targets of different elements or compounds, almost any material can be synthesized. Furthermore, since the growing material does not need to be heated during the synthesis, even thermally sensitive substrate materials can be coated with this technique. Due to its versatility and relatively low cost, it is widely used in both research and industrial applications.

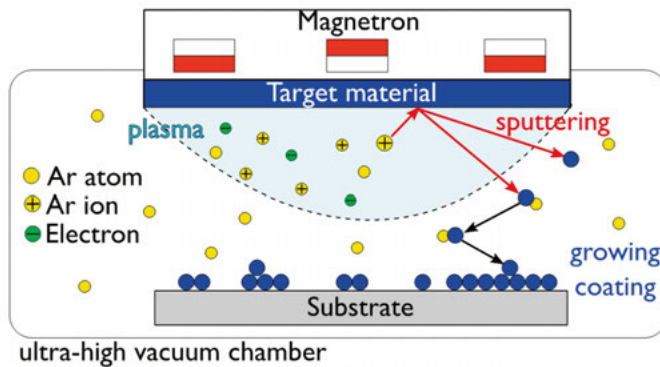


Figure 1. The main processes during magnetron sputtering. Based on an illustration in ref. [10]

Like all synthesis methods, magnetron sputtering produces materials with typical characteristics. One example is a small crystal grain size, often in the nanometer range, which is caused by the simultaneous nucleation at many points on the substrate. Another example is high residual stresses in the deposited material, which affect the mechanical properties.

¹ Note on the terminology: This type of materials can be called either *coatings* or, perhaps more commonly, *thin films* or just *films* [150]. The word *coating* was chosen in this text and will be used exclusively in order to avoid ambiguity between the deposited materials and the much thinner *passive films* formed during oxidation. However, some of the included papers and manuscripts use the word *thin film* to describe the deposited materials.

One feature that will be of particular importance in this work is the control of diffusion during magnetron sputtering. Since the deposition takes place at low temperatures, often close to room temperature, the diffusion of atoms can be limited compared to high-temperature synthesis methods like melting and casting. This makes it possible to synthesize materials under kinetic control, far from thermodynamic equilibrium. When diffusion is limited, simple structures with small unit cells and phases that require no elemental separation are favored, while more complex structures and the formation of multiphase materials can be suppressed. A well-known example is the hard and wear-resistant cubic phase of $\text{Ti}_{1-x}\text{Al}_x\text{N}$, which is commonly used as a coating for cutting tools. The single cubic phase material is metastable. However, through sputter deposition, it is possible to suppress the formation of the thermodynamically favored hexagonal phase that causes a breakdown of the mechanical properties. [11]

On the other hand, diffusion is not always slower than for bulk methods. At low temperatures, the atomic movement in the bulk of a crystal is almost negligible, while surface diffusion is several orders of magnitude faster. During coating growth, each atom spends time on the surface of the growing film, where it can diffuse rapidly. What happens during this short time is crucial to the phase formation and determines the structure and morphology of the coating. There is also a connection between the typically small grain size of the films and the diffusion rates. The energy of the atoms in grain boundaries is higher, since they are less ordered, and this lowers the energy barrier for their movement. A high density of grain boundaries can therefore result in higher diffusion rates. The many grain boundaries can also provide more sites for nucleation. An illustrative example of the effect of enhanced diffusion at low temperatures is the sputter deposition of 316L stainless steel. 316L typically forms a single fcc phase when synthesized from the melt, but during sputter deposition, the low-temperature bcc phase can easily form [12].

The extent of diffusion can be controlled by changing the deposition parameters. For example, by applying a substrate bias voltage, the energy of the atoms at the surface increases, thus promoting diffusion. A higher deposition rate has the opposite effect: the higher flux of incoming atoms results in a shorter time for surface diffusion. Heating the substrate during deposition increases the energy both on the surface and in the bulk of the coating.

In this thesis, multicomponent alloys and carbon-containing materials based on these will be explored using magnetron sputtering. The unique aspects of the synthesis technique are discussed throughout the thesis, but especially in Sections 6.1 and 7.2, and 7.4.1. In Section 6.1, the phase formation of a multicomponent alloy is compared to synthesis through melting and the effects of both the limited diffusion and the enhanced diffusion are exemplified. Sections 7.2. and 7.4.1. concern the properties of the material that are directly linked to the deposition technique.

Chapter 3. Multicomponent materials

3.1 High entropy alloys

High entropy alloys (HEA) are a class of materials first described in 2004 by Cantor et al. [8] and Yeh et al. [9]. In traditional alloy design, an alloy consists of one principal element with smaller amounts of other alloying elements, as shown in Figure 2(a). In a HEA, near-equal amounts of many elements are mixed, as in Figure 2(b). Four or five elements are usually considered the minimum. Based on the principles of traditional metallurgy, alloys with such complex compositions were expected to decompose into a mixture of phases, since the number of potential intermetallic phases is large [13,14]. Instead, HEAs stabilize into a single phase with a solid solution of all elements, crystallized in a simple structure, such as body-centered cubic (bcc) or cubic close-packed structure (ccp) (a.k.a face-centered cubic, fcc)². This was proposed to be due to the high configurational entropy of the solid solution, which is maximized with a large number of elements at an equimolar composition [15]. The new class of materials was, therefore, named high entropy alloys. The HEA concept and design approach quickly became a large research field. Part of the appeal was the large uncharted compositional space, since, at least in theory, the number of possible compositions is much larger than that for traditional alloys. Considering all combinations of five transition metals, there should be hundreds of thousands of new single-phase alloys to explore.

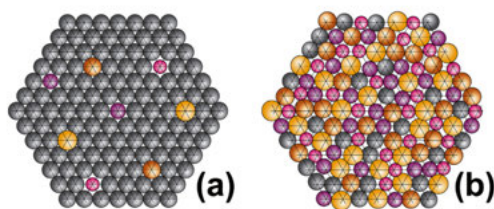


Figure 2. Schematic illustration of a conventional alloy and a single-phase solid solution high entropy alloy. Reprinted from ref [16] under the CC BY NC ND license.

² Note on the terminology. The terms ccp and fcc are often used interchangeably, although the former is a crystal structure and the latter is a crystal lattice. The term fcc is more ambiguous, since it could describe any structure based on the fcc lattice, for example NaCl or the highly complex Cr_{23}C_6 . The term ccp is more precise, but it can be argued that an alloy with elements of different sizes cannot be truly close packed. In this text, the term fcc was chosen simply because it is more commonly used in the HEA field. However, in some of the papers, ccp was used, and the term can therefore be found in some of the figures adapted from these papers.

3.1.1 Criteria for single-phase formation

Already from the first few publications on HEAs, it became clear that not all equimolar alloys of five elements can form an entropy-stabilized single phase [8,9]. Some will, instead, decompose into multiple phases with segregation of the elements. Different semi-empirical criteria for single-phase formation have been proposed, based on parameters such as valence electron concentrations, atomic radii differences, and electronegativities [16]. According to the fundamental principles behind the formation of HEAs, the entropy term of Gibbs free energy

$$\Delta G = \Delta H_{mix} - T \Delta S_{mix} \quad \text{Eq. 1}$$

must be higher than the enthalpy of all possible intermetallic combinations for the single phase to form. With this criterion, the pool of possible single-phase HEAs is lowered from hundreds of thousands to only a few hundred [17].

This simple principle is expanded with the CALPHAD method, in which calculations are used to predict phase compositions through the use of thermodynamic databases for similar systems. The results from these calculations, many of which have been validated through experiments, support the idea that the HEAs are entropy stabilized at higher temperatures where the entropy term is larger [18]. A typical phase fraction diagram of a HEA is seen in Figure 3(a). It shows the thermodynamically stable phases of a single HEA composition as a function of the temperature. Single-phase regions are often seen at high temperatures, while at lower temperatures, multiple phases are stable. In the diagram in Figure 3(a), the σ phase formed at lower temperatures is an intermetallic phase, i.e. an ordered compound of multiple metals.

3.1.2 Multi-phase and amorphous high entropy alloys

So, what happens in HEAs if they do not form a single phase? As expected from the principles shown above, not all equimolar alloy systems with more than five elements display single-phase regions in their calculated phase fractions. In the diagram in Figure 3(b), two solid solutions coexist at high temperatures: fcc and multiple bcc phases with different compositions. The third diagram in Figure 3(c) is an example where an intermetallic phase, C14 Laves, is present at all temperatures. The search for single-phase HEAs is often justified by the fact that intermetallic phases are embrittling, and this is true in many cases [16]. The corrosion protection is also generally better in single-phase materials since the segregation of elements can form regions with lower resistance or galvanic couples between different grains [19]. But this is not always the case, and in recent years, the potential of multi-phase alloys has

been explored, for example by the development of eutectic high entropy alloys [20]. These alloys have compositions chosen to form multiple phases with very fine-grained microstructures. Their toughness can be high even though they contain intermetallics and their properties can be finetuned by changing the size of grains [21]. As for corrosion, it is also possible to design multi-phase alloys where the composition of each phase is tuned to achieve sufficient corrosion resistance [22].

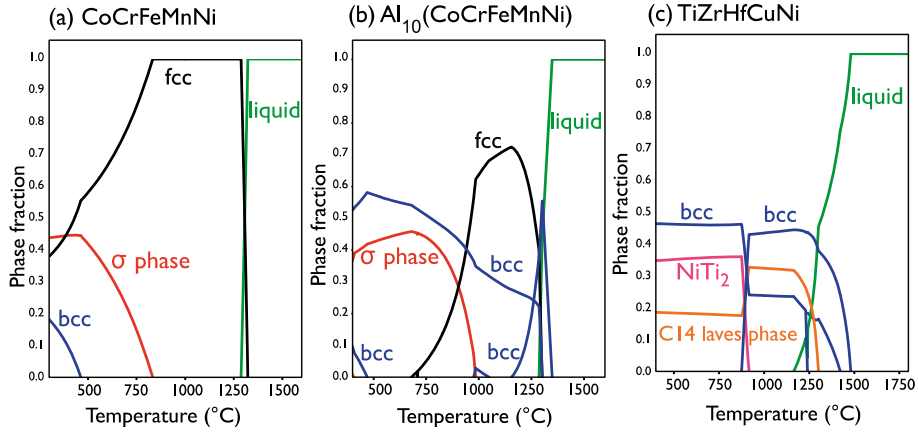


Figure 3. Phase fractions at equilibrium of (a) CoCrFeMnNi (a.k.a. the Cantor alloy) [8], (b) Al₁₀(CoCrFeMnNi)[23], and (c) TiZrHfCuNi[24] from Calphad calculations. The references are examples from the literature of the alloys synthesized as bulk materials. The alloys in (a), (b), and (c) are known to form a single fcc phase, a mixture of fcc and bcc, and metallic glass, respectively.

There is a third possibility for the phase formation in HEA compositions: avoiding crystallization altogether to create amorphous alloys, sometimes called metallic glasses. These alloys are not thermodynamically stable but form through rapid cooling from the melt or gas phase to the solid state. In the 1990s, Akihisa Inoue defined empirical rules for enhancing the ability of alloys to suppress crystallization, a.k.a. the glass-forming ability (GFA) [25]. One of the rules was mixing at least three alloying elements. This means that many HEAs also have high GFAs. An example of this is the alloy in Figure 3 (c). The other two criteria proposed by Inoue were a large difference in atomic radii and a negative enthalpy of mixing [25]. Zhang et al [26] classified HEA using two parameters related to the two latter rules. The atomic size difference was described as

$$\delta = \sqrt{\sum_{i=1}^N c_i (1 - r_i / \bar{r})^2} \quad \text{Eq. 2}$$

where N is the number of components, c is the atomic concentration of the component, r is the radius of component i , and \bar{r} is the weighted average of the atomic radius of all components. The enthalpy of mixing, ΔH_{mix} , of the alloy was calculated through

$$\Delta H_{mix} = \sum_{i=1, i \neq j}^n \Omega_{ij} c_i c_j \quad \text{Eq. 3}$$

where Ω_{ij} is $4 \cdot \Delta H_{mix}$ of the binary combination of elements and c is the atomic concentration of a component.

When Zhang et al. categorized HEAs as a function of these two parameters, they found two-dimensional regions that were dominated by random solid solutions, ordered solid solutions, intermetallic phases, and amorphous alloys, respectively. These are shown in Figure 4. Random solid solutions were more easily formed in alloys with low δ and ΔH_{mix} close to zero. At slightly higher δ and lower ΔH_{mix} , ordered solid solutions were preferred. In the regions with even higher δ and lower ΔH_{mix} , both multiphase and amorphous alloys were formed, with amorphous microstructures dominating the region with the highest δ values.

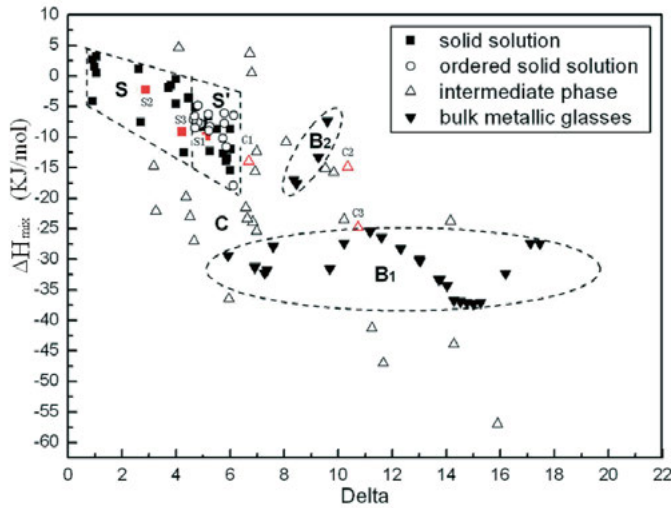


Figure 4. Categorization of some high entropy alloys by mixing enthalpy, ΔH_{mix} , and atomic size differences, δ , calculated using Eq. 2 and Eq. 3, respectively. The different markers represent alloys that form random and solid solutions, intermediate (intermetallic) phases, and amorphous structures. Reprinted from ref [26] with permission from John Wiley and Sons.

3.1.1 Notes on the definition of high entropy alloys

Since the discovery of high entropy alloys, their definition has been under discussion. Yeh et al, who coined the term HEA, defined the alloy class based on composition: at least five elements should be mixed with concentrations between 5 and 35 at% [9]. No criteria were placed relating to the entropy or phase composition. It was only later that definitions were discussed based on the magnitude of the entropy, or others that included only single-phase alloys. The emergence of these definitions was related to the fact that avoiding inter-metallics was considered the main motivation behind HEA research [16]. Since then, the development of equimolar alloys has crossed the boundaries of all the above-mentioned definitions, for example through the exploration of four-element alloys [27] and the increased interest in multi-phase microstructures [20]. Other terms have been proposed that describe the many-element, equimolar composition with fewer restrictions and no association with the single-phase criterion, for example, multicomponent alloys (MCAs), complex concentrated alloys (CCAs), and multi-principal element alloys (MPEAs) [16]. Though there will likely be a continued discussion on the definitions, these alloys are a distinct material class with a common denominator: they exist in the previously uncharted central regions of multi-dimensional compositional space.

In this work, the term multicomponent alloy (MCA) will be used to signify alloys with multiple elements (at least four) at near-equimolar concentrations, whether they can form a single phase or not. In one of the projects, the alloys will be modified with carbon, and when it is no longer justified to refer to them as alloys, they will be called multicomponent materials. The term high entropy alloy (HEA) will be used in certain parts of the thesis, specifically in discussions relating to single-phase formation. It will be used when studying the synthesis conditions needed for single-phase formation in the well-known single-phase HEA CoCrFeMnNi. I would like to stress that this choice is mainly due to the history of the alloy and the motivation behind the work. It is not meant to set this alloy apart from other MCAs.

3.2 The Cantor alloy and 3d transition metal MCAs

The first alloy studied in this thesis, CoCrFeMnNi, was one of the first to be identified as a HEA, and it was named ‘the Cantor alloy’ after Brian Cantor, the main author behind the first paper published on these materials [8]. Today, the Cantor alloy is one of the most well-studied HEAs [28]. As a bulk material, the alloy typically forms a single face centered cubic (fcc) phase. CALPHAD calculations, as illustrated in Figure 3(a), showed that the single phase is only stable above 800 °C [29]. Below this temperature, the alloy should form a phase mixture. However, the low-temperature equilibrium phases were seen

in bulk samples only after very long annealing studies. In one study of arc-melted bulk samples, the equilibrium phases formed after about one year [30]. On the other hand, in nanocrystalline materials [31] (including a study on magnetron sputtered coatings [32]) the decomposition of the single fcc phase was greatly accelerated through grain boundary diffusion and precipitation. The equilibrium phases were seen already after one hour. In as-deposited CoCrFeMnNi synthesized by magnetron sputtering, both single-phase fcc materials [32–35] and other crystal phases [36,37] have been reported. One of the aims of Paper I was to explain the varying results reported in different studies of the same alloy composition.

The Cantor alloy belongs to the family of MCAs known as the 3d transition metal group. These are alloys containing Al, Co, Cr, Cu, Fe, Mn, Ni, Ti, and V as the base elements and are by far the most well-studied type of MCA. Their compositions and material properties are in many ways reminiscent of stainless steels or superalloys. Some of them form single-phase fcc solid solutions, while others form fcc-bcc mixtures or fcc with intermetallic precipitation. Most of them contain Cr [16] and in corrosive environments, they rely on its ability to form a Cr-rich oxide layer that slows down the dissolution of the alloy [38], just like stainless steel [39]. This is the case for the Cantor alloy which was shown to have comparable corrosion resistant to 304 stainless steel in an acidic environment [40].

The Cantor alloy and certain 3d transition metal MCAs also possess interesting mechanical properties. Contrary to most materials, the ductility of the Cantor alloy has been reported to increase with decreasing temperatures between 293 K and 77 K [41]. The plastic deformation of alloys typically happens through the movement of dislocations, which are crystallographic defects. The resistance to deformation can be altered by adding or removing features that hinder the dislocation movement: solute atoms, grain boundaries, and precipitates. While these features increase the hardness, they have the drawback of simultaneously embrittling the material. It is therefore a challenge to optimize a material for both hardness and ductility. Some alloys overcome this trade-off by deforming through a different mechanism. The high plasticity at 77 K was reported to be due to the formation of twins in the crystal structure [41], another type of defect depicted in Figure 5 (c). Twins form when the stacking order of atomic planes is reversed. When many, densely spaced twins form under stress, the alloy can deform plastically. This is called deformation twinning.

The observation of deformation twinning is associated with a low stacking fault energy (SFE). Stacking faults is the more general term for irregularities in the sequence of the atomic planes of the crystal, including twins. The SFE is the excess energy to form an irregularity from perfect stacking (depicted in Figure 5 (b)), and this can be tuned by changing the chemical composition of the alloy [42]. Low SFEs have been found for some cubic materials with an fcc structure such as Cu, Al, and some stainless steels [43]. Several high

entropy alloys are also known to have very low SFE [44]. The Cantor alloy has an SFE of only 21 mJ/m² at room temperature [45], which can be reduced further by an increase in the Mn content [46].

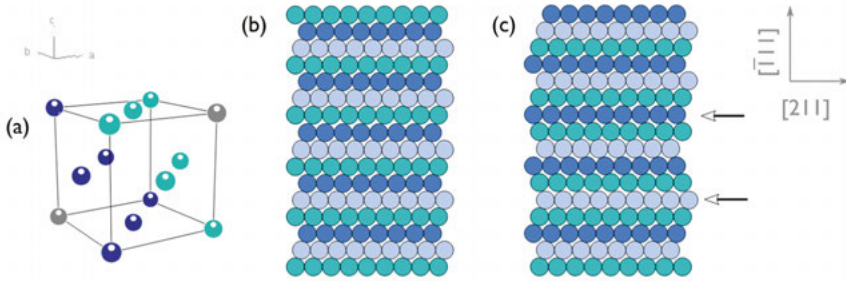


Figure 5. Schematic images of an fcc crystal showing (a) a unit cell where the atoms in each (111) plane have different colors, (b) perfect stacking of (111) planes, and (c) stacking of (111) planes including two twin boundaries marked with arrows.

Nanotwins have also been observed in magnetron sputtered HEA coatings already in the as-deposited state [37,47]. This effect has not been fully explained but could be due to the high intrinsic stress associated with the deposition process. The effect of the already-formed twins on the mechanical properties is not fully understood either, but Wang et al. [47] reported that the hardness was affected by the spacing between the twins, which is in agreement with current knowledge on stacking faults in general [48].

3.3 Adding carbon to MCAs

Alloys can be modified by the addition of small non-metallic elements, such as carbon. Interstitial hardening by carbon addition is a well-known mechanism and carbon can also act as a grain refiner, which also leads to strengthening. The addition of carbon to MCAs is, in principle, analogous. However, since the carbon interacts differently with each component, the complexity increases. For instance, there is a high likelihood that carbon has a higher affinity for certain metals in the alloy. The carbon affinity for the elements will, for example, determine the solubility of carbon in the alloy phase. It will also determine whether a metal carbide can be formed or not.

MCAs in which the components have high carbon affinities can form high entropy carbides, some of which are single-phase materials [49]. Alloys in which none of the components are stable carbide formers decompose and form a composite material with an alloy phase and graphite [50]. The alloys explored in this thesis represent the third case: each of them is a mixture of elements known to form carbides (Cr, Mn, Ta, and W) and elements that have no thermodynamically stable carbides (Fe, Co, and Ni). In bulk materials, this usually results in phase segregation with the formation of carbide precipitates,

and the strong carbide-forming elements are then depleted from the alloy phase [51,52].

Carbon addition to the Cantor alloy CoCrFeMnNi has been explored previously for bulk materials. Up to 1 at% carbon was reported dissolve interstitially while maintaining a single phase and this strengthens the alloy [53] and also increases its resistance to aqueous corrosion [54]. At higher carbon contents, Cr-rich carbides precipitates, which further strengthens the material, but simultaneously embrittles it [55]. The corrosion resistance has also been reported to be negatively affected by the carbide formation which the authors attributed to pitting corrosion close to the precipitates [54]. Considering the material properties desired in this work, it appears that the low solubility of carbon limits the benefits of carbon-addition. However, the addition of carbon through magnetron sputtering gives different results.

As explained in Section 2, magnetron sputtering at low temperatures can result in materials that are far from thermodynamic equilibrium. The limited diffusion favors simple crystal structures while suppressing phase segregation. In previous studies on carbon-containing metal films, the synthesis method has been used to suppress the formation of crystalline carbides in both single-element and HEA coatings [56,57]. In these studies, carbon was added beyond the solubility at equilibrium, creating super-saturated solutions in the bcc matrix. The carbon was reported to decrease the grain size of the materials and make the coatings both harder and more crack resistant. When even more carbon is added, it can begin to precipitate in the grain boundaries, which can result in corrosion resistant materials with good electrical properties [58,59].

The addition of carbon to magnetron sputtered MCA coatings has thus far been limited to alloys containing the early transition metals, which are strong carbide formers [60]. In this work, carbon was added to the alloys CoCrFeMnNi and CrFeNiTa through magnetron sputtering at close to room temperature, to suppress segregation and carbide precipitation. The comparison between the two alloy systems will be used to understand how the concentration of strong carbide formers affects the results.

3.4 Why should we study MCA coatings?

In the early days of MCA research, statements about their promising properties were often over-generalized. For example, the “superior corrosion resistance” of MCAs was treated as a standard feature in paper introductions, where articles on corrosion resistant HEAs were often cited regardless of the similarity to the studied composition (see for example refs [37,61]. However, recent reviews on the corrosion of MCAs make no such claims about MCAs as a group [38,62,63]. A similar development was seen for the concept of sluggish diffusion, which was considered one of the core effects of MCAs but was later shown to be tied to specific compositions [16,64]. There may be

properties that are indeed enhanced specifically due to the equimolar composition (the lattice distortion leading to a higher strength is still under discussion [16]). However, as more different MCAs are explored, it becomes clearer that their properties are as diverse as their compositions. *So why should we study them?*

It was argued by Brian Cantor, one of the inventors of the MCA concept, and by several authors of subsequent reviews [8,16,62], that the main promise of the MCA field lies in the vast number of combinations and variations of elements. The central regions of compositional space have been almost completely unexplored, and the possible range of compositions is greater than for alloys with one or two principal elements. Somewhere in that uncharted space, there may be extraordinary materials. And since their invention, there have indeed been critical discoveries of MCAs that surpassed all conventional alloys in some regard. One example was the Cantor alloy with its high toughness at cryogenic temperatures [41]. The main problem is finding interesting compositions without having to screen the entire compositional space. That is why fundamental studies are needed to find the parameters for how to tune their properties.

Most research on MCAs is performed on bulk samples, but the use of MCA as coatings could be of greater interest in the future. Compared to many traditional technical alloys, the cost of the alloying elements will be greater for MCAs. Stainless steel, for example, is composed of around 70 at% Fe, which is by far the cheapest metallic element. For comparison, the price of raw Co is about 500 times higher. The reliance on a bulk MCA would also mean a greater risk since the supply of metals is always changing [65]. This would be solved by using MCAs as thin (nanometer scale) coatings on more widely available and less costly substrates.

The synthesis of MCAs by magnetron sputtering is also interesting for fundamental reasons. In the section on the thermodynamic basis of HEAs, it was explained that the single phase in HEAs is stabilized at high temperatures. Considering this, the relevance of the high entropy concepts for low-temperature synthesis methods, such as magnetron sputtering, is not obvious. Nevertheless, magnetron sputtering is the most common way of synthesizing HEA coatings [66], and in most of the published articles (see the Appendix) single-phase coatings are reported. The reasons behind this trend will be explored in Section 6.1.

Chapter 4. Aim and scope

The overhead aim of this work was to formulate design principles for new multicomponent materials with high corrosion resistance, hardness, and crack resistance. These are, as explained in the introduction, the requirements for coatings on stainless steel components in fuel cells and electrolyzers. However, this combination of properties could be beneficial for a number of other applications.

CoCrFeMnNi, a.k.a. the Cantor alloy, was chosen as the first model system to understand the phase formation of MCAs during magnetron sputtering. The choice of CoCrFeMnNi was mainly due to the relatively large number of existing studies on the alloy compared to other MCAs, and because many MCAs are based around this composition. This means that there is more prior knowledge about the alloy and that conclusions made on this system can more likely be generalized to other MCA systems.

After studying the model system, new alloys were designed. From the electrochemical tests on CoCrFeMnNi, it was found that Mn and Co were the least beneficial elements for corrosion protection, and they were, therefore, not included in the new alloys. Ta and W were chosen as replacements because of their resistance to corrosion in high-potential environments. They will be used to increase the corrosion resistance of CrFeNi-based MCAs. Furthermore, their different nobilities make it possible to test a fundamental principle concerning the corrosion resistance of alloys. The equimolar CrFeNiTa and CrFeNiW systems have not been studied previously.

Carbon was also added to the alloys, to study if the addition of a p-element can improve both the mechanical properties and the corrosion resistance. The modification with carbon was tested on two different alloy compositions to understand the effect of the base alloy composition on the resulting phases and properties.

All the elements included in the studies are shown in Figure 6.

| | | | | | | | | | | | | | | | | | | |
|---|----|----|----|----|----|----|----|----|----|----|----|----|----|----|----|----|----|----|
| | 1 | | | | | | | | | | | | | | | | | 18 |
| 1 | H | 2 | | | | | | | | | | | 13 | 14 | 15 | 16 | 17 | He |
| 2 | Li | Be | | | | | | | | | | | B | C | N | O | F | Ne |
| 3 | Na | Mg | 3 | 4 | 5 | 6 | 7 | 8 | 9 | 10 | 11 | 12 | Al | Si | P | S | Cl | Ar |
| 4 | K | Ca | Sc | Ti | V | Cr | Mn | Fe | Co | Ni | Cu | Zn | Ga | Ge | As | Se | Br | Kr |
| 5 | Rb | Sr | Y | Zr | Nb | Mo | Tc | Ru | Rh | Pd | Ag | Cd | In | Sn | Sb | Te | I | Xe |
| 6 | Cs | Ba | La | Hf | Ta | W | Re | Os | Ir | Pt | Au | Hg | Tl | Pb | Bi | Po | At | Rn |

Figure 6. Periodic table of elements showing the elements included in the studied materials. The elements in the first model system are marked in blue, the red are the elements added to the novel alloy compositions, and carbon, marked in black, is the modifying p-element.

The main results of the projects are presented in Chapters 6 and 7. Chapter 6 concerns the relationship between the synthesis conditions and the structure of the materials. It is a systematic exploration of how the crystal structure (or lack thereof) and morphology can be controlled during synthesis and subsequent annealing. The studied parameters include the concentration of the metals in the alloy, the carbon content, several sputter process parameters, the choice of substrate material, and the annealing temperature.

Chapter 7 investigates the relationship between material characteristics (structure, microstructure, and morphology) and material properties (mechanical and electrochemical). Through the results of the study, we can better understand how to tune the properties and define strategies for future materials design.

Each of the included papers has a narrower aim and is based on a few delimited scientific questions. The questions are listed below:

- I. What are the fundamental differences in the phase formation through sputtering deposition and bulk synthesis of the CoCrFeMnNi HEA? Why do some studies on magnetron sputtered CoCrFeMnNi report a single phase while others report phase mixtures?
- II. How do a commercial substrate material and its crystal orientation affect the growth of magnetron sputtered CoCrFeMnNi coatings?
- III. What is the lowest concentration of Ta or W, needed to achieve corrosion protection in (CrFeNi) X_x ($X = \text{Ta, W}$) at high potentials? What is the importance of the nobility of the added elements?
- IV. Does carbon addition to magnetron sputtered CoCrFeMnNi coatings result in increased segregation of the metallic elements?
- V. Can the addition of up to 11 at% C to CoCrFeMnNi improve the mechanical properties and corrosion resistance?

- VI. How does the inclusion of carbon affect the corrosion behavior of CoCrFeMnNi in different electrolytes?
- VII. Can the addition of up to 49 at% carbon to MCAs result in a composite material with improved mechanical properties? How does the concentration of strong carbide-forming elements affect their phase formation and properties?

Chapter 5. Methods

5.1 Thermodynamic calculations

The CALPHAD method, which stands for CALculation of PHase Diagrams, was developed in the 1970s [67] and is a way to predict the phase properties of alloys by using thermodynamic databases. Many high entropy alloy systems have been explored based on thermodynamic data from binary and ternary sub-systems [18]. In this work, the CALPHAD method was used to predict the phases of alloys at equilibrium at different compositions and temperatures. The calculations were performed in the Thermo-Calc Software using the TCS High Entropy Alloys Database version 3 (TCHEA3) [68].

5.2 Synthesis

The coatings in the study were synthesized with direct current (dc) magnetron sputtering in an ultra-high vacuum deposition chamber with a base pressure below 10^{-6} Pa. The system has four magnetrons that can fit cylindrical sputter targets of either 51 or 76 mm in diameter. The targets were, in most cases, focused directly on the middle of the sample holder, which is at a distance of 130 mm from the targets. CoCrFeMnNi alloy coatings were deposited with a single, spark-plasma sintered target with equimolar composition. CrFeNiTa and CrFeNiW alloy coatings were synthesized by using a similar sintered CrFeNi target and pure Ta or W targets. The powers of the Ta and W targets were varied to achieve different concentrations of these two metals. Carbon was added to the alloys by co-sputtering with a single graphite target. The process parameters, such as temperature, pressure, target powers, and substrate bias were varied, as was the deposition time.

In most cases, the substrate was rotated to achieve a homogenous composition and thickness on the samples. In one study, however, the rotation was turned off to intentionally form a gradient in the composition over the surface of the sample holder. This made it possible to screen through a range of compositions with a single deposition. This is called a combinatorial approach [69] and is beneficial for studying the compositional space of multicomponent systems [70]. The combinatorial approach was utilized to synthesize samples in the CoCrFeMnNi and CrFeNiTa systems with varying carbon concentrations.

The standard substrate material used for characterization was single-crystalline Si(001) that had been oxidized to form a 1.5 μm thick amorphous oxide on the surface. This substrate has multiple benefits: It simplified diffraction analysis since the single crystal gives only a few reflections. The substrate could easily be cleaved along the (001) crystal plane to produce cross-section samples of the coatings. The amorphous oxide ensures that no lattice matching was possible between the substrate and coating. This is referred to as a “neutral” substrate. Furthermore, the oxide was both thermally stable and resistant to corrosion, allowing the samples to be annealed without reactions at the substrate/coating interphase and ensuring that the substrate contributed with only a low current if it was exposed during electrochemical tests.

The effect of the substrate on the coating structure and morphology was studied by using crystalline materials: Si(001), Al_2O_3 (0001), and finally, polycrystalline 316L stainless steel, which is more relevant for the potential application of these coatings. Lastly, polyimide strips were coated for mechanical tests. These flexible polymer substrates can be used to isolate the behavior of the coatings under tensile stress, a method described in Section 5.4.

5.3 Materials characterization

The following set of techniques was used to characterize the materials in terms of chemical composition, chemical environment, crystal structure, microstructure, and morphology.

Electron microscopy

The morphology of the films, such as grain sizes and shapes, the coating thickness, and other features at this scale were studied with scanning electron microscopy (SEM). SEM is performed in a vacuum chamber, where a focused electron beam is scanned over the sample, and backscattered or secondary electrons are detected to form a micrograph image. Most of the measurements in this work were performed using the in-lens or secondary electron detectors in three different instruments, a Zeiss Merlin, a Zeiss 1550, or a Zeiss 1530 instrument. The acceleration voltage, beam current, and sample tilt were varied for each use.

Transmission electron microscopy (TEM) is a related technique, where electrons are transmitted through thin samples. Electron-transparent cross-section samples were prepared with a focused ion beam. Bright-field and dark-field imaging, as well as scanning TEM (STEM), were used to study the morphology.

Both SEM and TEM can be combined with energy-dispersive X-ray spectroscopy (EDS or EDX). When atoms are excited by electrons, they emit X-rays with an energy that is characteristic of the element. This signal can be used to quantify the atomic composition and create maps of the distribution of

the elements. EDS maps were used in this work to study the elemental segregation in the films. EDS was performed in the Zeiss 1530 or Zeiss 1550 SEM using an 80 mm² silicon drift detector, and in the FEI Titan Themis using the SuperX system.

Profilometry

Profilometry is used to map the topography of a surface. Optical profilometry was used in this work to measure nanometer-scale height differences over the sample surfaces. The measurements were performed on a Wyko NT9100 instrument from Veeco, used in phase shift interferometry mode. This mode utilizes the interference between the light projected onto the sample and onto a reference surface with a known distance from the light source. This can then be reconstructed into a 3D image of the surface.

Profilometry was also used to measure the roughness evolution on the surface during corrosion. Since this roughness can be in the sub-nanometer scale, a higher resolution was required. This was achieved with atomic force microscopy (AFM). The method function by letting a sharp, oscillating tip, placed on a cantilever, interact with the surface of the sample. The electrostatic forces from the surface perturb the movement of the tip, and this signal is used to measure the distance from the surface. The tip is scanned over the surface and a topography image is constructed. Roughness parameters, such as Ra, can then be extracted from the data.

Diffraction

X-ray diffraction (XRD) is a method for studying the structures of materials through the elastic scattering of X-rays by the lattice planes in the crystal. In this work, θ - 2θ measurements were used to probe the crystal planes parallel to the substrate. Grazing-incidence (GI) measurements were performed to isolate the crystal phase compositions of the coatings by minimizing the signal from the substrate.

Diffraction was also performed with electrons in the TEM. Due to the focused electron beam and the simultaneous imaging of the sample, it is possible to study the diffraction of a selected area, like a crystal grain, through selected area electron diffraction (SAED). Smaller grain sizes can be analyzed, which is important when working with nanocrystalline materials that may appear amorphous when analyzed with X-rays. There are multiple techniques that can be used to localize the signal of a certain crystal structure, such as hollow cone dark-field imaging or 4D scanning transmission electron microscopy (4D STEM, formerly known as STEM diffraction imaging). These techniques were used to create maps of the regions with different crystal structures.

Another diffraction-based technique is electron backscatter diffraction (EBSD). The technique works by recording the backscattered electrons emitted in the SEM, a Zeiss Sigma FEG-SEM. The scattering of the electrons as they exit the sample gives rise to so-called Kikuchi patterns. These can be

analyzed to find the orientations of a crystal if the structure is known. Many Kikuchi patterns are recorded as the electron beams sweep over the surface, after which a map can be constructed showing the crystal orientation of each grain. When performed on a lamella instead of a top-view sample, the technique is called transmission Kikuchi diffraction (TKD), and a higher lateral resolution is achieved with this technique. The detected signal can also be compiled to form a microscopy image with strong crystallographic contrast. This is called band contrast imaging.

Electron spectroscopy and synchrotron-based techniques

X-ray photoelectron spectroscopy (XPS) was used to study the chemical environments around different elements in the coatings. The technique is based on the photoelectric effect. Incoming X-rays ionize the atoms in the material which then emit electrons. The kinetic energy of the electrons is related to the binding energy of that electron in the material, which varies with the element and the chemical environment.

The XPS analysis was performed in a PHI Quantera II 2000 scanning XPS microprobe with monochromatic Al K α radiation. When studying the bulk of the films, the oxide layers were removed by sputtering with 200 eV Ar⁺ ions. When performing surface analysis, the angle between the sample surface and the electron energy analyzer was varied to achieve different information depths. XPS was used to find the composition of a material since the relative signal from each element is proportional to its concentration. This was used to quantify oxygen and carbon in most studies since EDX lacks sensitivity for these light elements. Relative sensitivity factors were needed for the quantification, and they were calculated using reference samples measured by elastic recoil detection analysis (ERDA). By combining chemical information with the ability for quantification, the relative signal from each metal in its oxidized state was used to calculate the cation fraction of each element in the surface oxides.

A form of XPS can also be performed at a synchrotron. The photons are then generated by the deceleration of electrons. The photon energies can be much higher than the in-house XPS (this is then called hard XPS, HAXPES) and the energy can be precisely controlled. This makes it possible to vary the information depth and achieve more bulk-sensitive information without the need for sputter etching, which can damage the material. It is also useful for separating XPS peaks from Auger electron signals. At some beamlines, a higher energy resolution can also be achieved [71].

The high and variable photon energy can also be used for X-ray absorption studies. The photon energy is then swept and the absorption of photons at different energies is recorded by measuring either the sample current or the fluorescence. This technique also gives chemical information and can be used as a complement to XPS.

Time-of-flight elastic recoil detection analysis (ToF-ERDA)

ToF ERDA is a technique for quantifying the elements in a material without the use of references. The technique works through the bombardment of heavy ions with a high energy ($36 \text{ MeV } ^{127}\text{I}^{+8}$ or $44 \text{ MeV } ^{127}\text{I}^{+10}$), which causes elastic recoil of the atoms in the material. The measurements in this work were performed at the Tandem laboratory at Uppsala university. The technique is highly sensitive to light species, so the relative concentration of C and O in the films could be found with high accuracy. For some of the sample series, all the samples were quantified with ERDA. For other studies, ERDA was performed on reference samples that were then used to calculate the relative sensitivity factors used for quantification in XPS. However, ERDA cannot separate heavier elements with similar mass, so EDS was always used to quantify the metals.

5.4 Testing of material properties

5.4.1 Corrosion testing

Electrochemical methods with a three-electrode cell

Electrochemistry is the study of chemical reactions that involve an electric current. In an electrochemical cell, reaction rates of redox processes can be measured as currents and the driving forces as electrical potentials. By actively applying currents or potentials, the reactions can also be driven in a certain direction, for example, to accelerate a corrosion process.

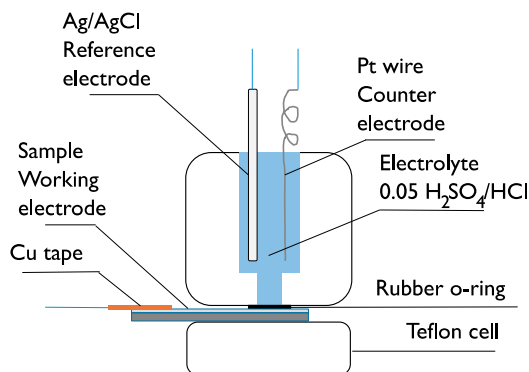


Figure 7. Illustration of the experimental set-up for the electrochemical experiments, depicted in cross-section.

A three-electrode setup was used for the tests. The samples were placed in an in-house made Teflon cell, shown schematically in Figure 7, and used as working electrodes. The samples were at the bottom of a cylindrical reservoir where the electrolyte (0.05 M H₂SO₄ or 0.05 M HCl) was added. An O-ring

with an inner diameter of 5 mm provided a consistent working electrode area. The counter electrode was a Pt wire and the reference was a Ag/AgCl (3 M NaCl) electrode. The electrodes were connected to a potentiostat/galvanostat, an Autolab PGSTAT302N from Metrohm Instruments, or a VersaSTAT 4 from Princeton Applied Research.

All the measurements were performed at room temperature. The following three techniques were used:

Open Circuit Potential (OCP)

The open circuit potential is the potential between the working electrode and the reference when no current is flowing in the cell. In a corrosion test, this entails that the sample is allowed to corrode freely in the electrolyte. The OCP value depends on the rate of the corrosion reactions. The corrosion tests were started by keeping the samples at the OCP for up to 2 hours until the values were nearly stable. This ensured that the reactions were at a steady-state before starting additional measurements.

Electrochemical Impedance Spectroscopy (EIS)

Electrochemical impedance spectroscopy (EIS) can be used to compare the corrosion resistances of materials. An ac voltage with an amplitude of 10 mV was applied on top of the OCP. The ac frequency was then varied from 100 kHz (initial frequency) to 100 mHz (final frequency) and the current response was recorded. The impedance data can be interpreted by fitting it to a model circuit, where the circuit elements represent the characteristics of the corrosion cell. In this way, comparative values can be acquired, such as the charge transfer resistance during the corrosion.

Potentiostatic or potentiodynamic polarization

The samples were polarized by applying a potential between the reference and working electrodes, and the current response in the cell was recorded. A higher potential means that the driving force for corrosion is increased, and the current is a measure of the oxidation rate. In linear sweep voltammetry (LSV), also known as potentiodynamic polarization (PDP), the potential between the sample and the reference electrode is scanned from one potential to another. The starting potential and the scan rate (V/s) were varied to obtain different types of information. The results were plotted as polarization curves. Several parameters can be extracted from such a curve, which describes the corrosion behavior of a material in a specific electrolyte, including the corrosion current density j_{corr} , the corrosion potential E_{corr} , and the passive current density j_{passive} . The samples can also be polarized by applying a static potential to isolate the changes in the current over time.

Inductively coupled plasma-mass spectrometry (ICP-MS)

ICP-MS is a method for measuring the concentration of ions in a solution. In this work, it was used as a complement to the electrochemical tests by measuring the concentrations of dissolved metal ions in the electrolyte after the electrochemical experiments.

5.4.2. Mechanical testing of coatings

The formulated requirements for the coatings in this project, to be durable and deform without cracking, can be condensed to a few mechanical properties that describe the plastic deformation. Durability, the resistance to wear and scratches, is related to the hardness of the coatings. The crack resistance is more complex; for coatings, it depends on the strength and ductility of the coating material, but also the adhesion to the substrate.

Because of this complexity, few lab-scale tests are fully representative of the real-life application. In this work, multiple methods were combined to achieve a deeper understanding of the deformation of the coatings under different types of loading.

Nanoindentation

The most common method for testing the mechanical properties of coatings is nanoindentation [72]. It is performed by pressing a hard tip into the sample and recording the load as a function of the displacement. The behavior of a coating during the indentation depends on the resistance to both elastic and plastic deformation. To isolate the coating behavior from that of the substrate, the depth of the indents cannot exceed 10% of the coating thickness. Indents were made using a CSM instrument, and a Berkovich diamond tip. The hardness and the reduced elastic modulus were calculated using the Oliver and Pharr method [73].

Nanoindentation can also be used to qualitatively study the deformation of coatings, including cracking behavior under stress, by making deeper indents into the material [72]. In this study, indents of more than twice the thickness of the coatings were made using a cube-corner diamond tip, after which the indents were studied with SEM.

However, this technique cannot simulate deformation under tensile strain. Other methods are available, such as tensile tests on free-standing films [74], but they often require extensive sample preparation and are limited to thicker coatings. In this thesis, tensile testing on polymer substrates is used. It is more representative of the application than nanoindentation, while also producing quantitative data.

Fragmentation testing

To study the crack resistance of the coatings under tensile stress, fragmentation tests were carried out. The flexible polymer substrates were stretched in a Deben tensile stage using a displacement rate of 0.1 mm/min, inside a Hitachi SEM at 15 kV acceleration voltage. Three areas on each sample were selected and the number of cracks in that area were recorded at different strains until crack saturation was reached.

The crack density (CD) can be described by the probability of failure according to the Hui model [75]:

$$F_{\infty} = CD(\sigma)/CD_{\infty} \approx 1 - \exp[-(\sigma/\sigma_{\infty})^{\rho}] \quad \text{Eq. 4}$$

where CD_{∞} is the crack density at saturation, σ is the stress on the coating, and ρ and σ_{∞} are the Weibull shape and scale parameters, respectively. The Weibull parameters were fitted to the crack density data, and the values were used to compare the coatings. A higher σ_{∞} means that the coating is stronger, and a higher ρ means that there is a lower scatter in the strength.

When this model is typically used, the coatings are assumed to have only elastic behavior until fracture. This can then be modeled by Hooke's law $\sigma = \bar{E}\varepsilon$, where \bar{E} is the reduced Young's modulus extracted from nanoindentation and ε is the strain. For the softer coatings in this work, however, this model did not fit the data. This was because there was a significant contribution from plastic deformation during the tensile tests. In these cases, a second term was added to account for the plastic deformation after yield stress σ_Y was surpassed. This is described in greater detail in Paper VII.

5.4.3. Interfacial contact resistance

The interfacial contact resistance (ICR) is the resistance between two materials in contact. It is a complex property that depends on the intrinsic electrical resistance of each material but also on its mechanical properties. This is because the contact area (which is very different from the geometric area) between the surfaces changes as the materials deform under compression. In this work, the ICR measurements were performed according to a method developed for bipolar plate materials [76]. The ICR was measured by placing a sheet of Freudenberg 23H carbon paper (a gas diffusion layer material) between two stainless steel plates coated with the material of interest. The resistance was then measured under increasing compressive load. The measurements were performed before and after potentiostatic polarization to study how the formation of a passivating oxide affected the ICR.

Chapter 6. Synthesis of multicomponent coatings

6.1. Controlling the phase formation in sputtered HEAs

CoCrFeMnNi, a.k.a. the Cantor alloy, was used as a model system to understand the principles of phase formation during magnetron sputtering of HEAs. The primary aim of Paper I was to answer the question of whether there is a fundamental difference between magnetron sputtering and melting of HEAs. This question will be answered step by step in the next few sections. The phase formation was first explored through a variation of process parameters during deposition on a single type of substrate: Si with a 1.5 μm thick amorphous oxide grown on top (Section 6.1.1). An amorphous substrate ensured that it could not influence the growth of the coating through lattice matching. The phase formation was then compared to studies on bulk CoCrFeMnNi, and the key differences were described (Section 6.1.2.). A literature review on magnetron sputtered HEAs was also performed to understand if the principles found for the Cantor alloy are valid for HEAs in general (Section 6.1.3.). The final two sections examine the influence of the substrate material on the phase formation of CoCrFeMnNi (Section 6.1.4.), and lastly, the special case of CoCrFeMnNi deposited on polycrystalline stainless steel (Section 6.1.5.).

6.1.1 Effect of process conditions

A series of samples were deposited using a single equimolar composite CoCrFeMnNi target. Three deposition parameters were varied one at a time: the substrate temperature, the target power, and the substrate rf-bias. The temperature had the greatest influence on the material and will be the focus of this section, while the series with different target powers is excluded, as no differences were observed with microscopy or diffraction. All the films in the temperature series were deposited with a floating bias. The lowest temperatures (20-60 $^{\circ}\text{C}$) were achieved without any applied heating, while the rest of the depositions were performed with active heating of up to 600 $^{\circ}\text{C}$. The increase in the substrate temperature had three main effects: a change in the crystal phase composition, grain growth, and increased separation of the elements.

The influence of temperature on the phase composition is depicted in Figure 8. In the samples deposited at 400 $^{\circ}\text{C}$ and above, a phase mixture of fcc

and σ (sigma) phase could be seen. The σ phase peaks decreased in intensity with increasing temperature, pointing to a reduction in the relative amount of this phase. Using electron diffraction in TEM, a small amount of the MnNi-rich phase $L1_0$ was also observed. It appears that the phases formed in this temperature range were the same as those reported after the long-term annealing of the bulk material at 700 °C [30] and the short annealing of the coatings near 300 °C [32]. The results partly agree with the CALPHAD calculation (seen in Figure 3), which correctly predicted a decreasing amount of σ phase at higher temperatures. At 300 °C, no σ phase was present, and the coatings consisted of a mixture of fcc and bcc phases. A preference for bcc over σ phase after long-term annealing of bulk samples at 500°C has been reported in the literature [30,31].

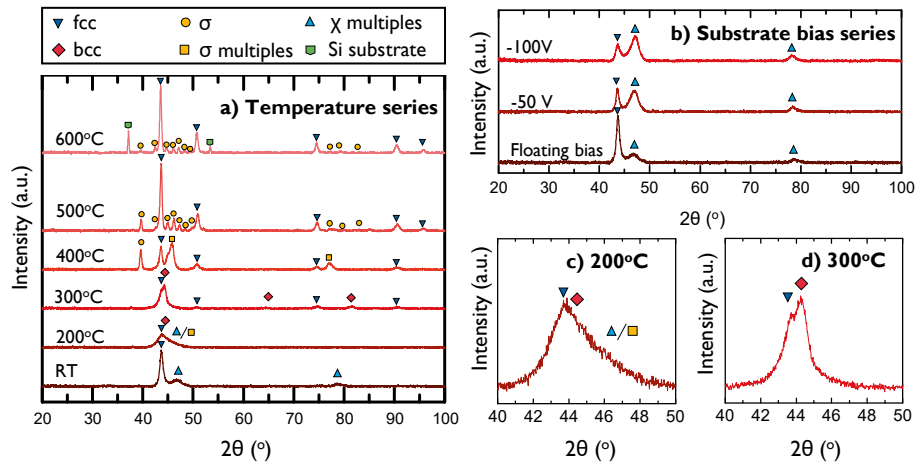


Figure 8. The phase compositions of the CoCrFeMnNi films deposited at varying substrate temperatures (a) and bias voltage (b), as measured by GI-XRD. A narrower 2θ range for samples 200 °C and 300 °C is shown in c) and d). The figure is adapted from Paper I.

In the samples deposited without heating (marked RT), an fcc and the intermetallic χ (chi) phase were present, the latter as multiple overlapping peaks. The χ phase has a complex cubic structure (I-43m) with a unit cell of 58 atoms. Like the σ phase, it can display a range of compositions by substitution with similar transition metals [77,78]. The χ phase has been reported in a HEA coating similar to CoCrFeMnNi [79], but it is most well-known as one of the intermetallic phases causing embrittlement in ferritic, austenitic, and duplex stainless steels [80–82]. In steels, it is almost exclusively observed together with the σ phase. It often precipitates at lower temperatures than the σ phase and is consumed by the σ phase as the latter one forms. It is, therefore, suggested to be a meta-stable phase in many steels, and can be regarded as a precursor to the σ phase [81]. The development of these phases can be seen in the

bias series (Figure 8 (b)), which was deposited without heating. The intensities of the χ phase peaks increased with the increasing bias voltage.

A second effect of the increasing substrate temperature was the formation of larger grains, shown in Figure 9. This is typically seen in sputtered films at higher temperatures and can be explained by an increased diffusion rate of atoms at higher temperatures.

The third effect was an increase in the segregation of elements. TEM-EDX maps of two selected samples are shown in Figure 10. The segregation was prominent in the sample deposited at 500°C. The composition of each of the grains is displayed in Figure 10 (c) and shows that the separation of the elements was slightly less evolved than in the annealing studies, where the σ phase obtained at both 350 °C and 700 °C consisted of around 50 at.% Cr. [30,32]. This indicates that the equilibrium compositions had not yet been reached. The TEM-EDX maps of a sample deposited without heating but with -100V substrate bias are presented in Figure 10 (e). In the maps, there is no evidence of elemental segregation, even in the regions where clear diffraction contrast is seen in STEM. It seems that, although multiple phases were present, they had the same composition. This points to a highly limited diffusion during deposition at lower temperatures. The two phases were most likely a product of simultaneous nucleation and kinetically controlled growth. The relative increase in the χ phase with increasing bias is evidence of this; the fcc phase, with its simple structure and a small unit cell, needs less atomic movement to form than the large and complex χ phase. The fcc phase is, therefore, favored by reduced atom mobility.

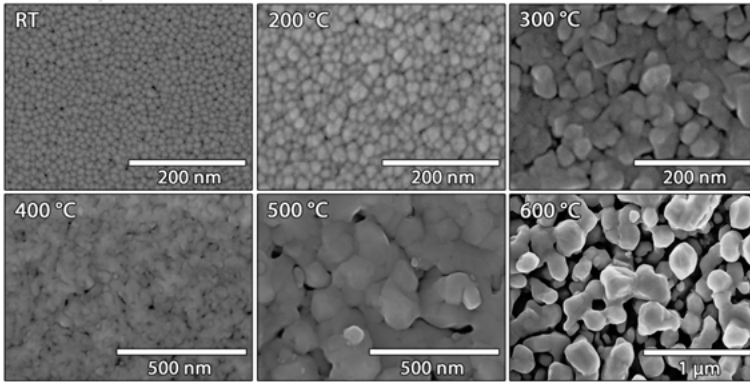


Figure 9. Morphology of the films deposited at various substrate temperatures, from room-temperature (RT) to 600 °C, as seen by top-view SEM using an in-lens detector at 8 kV acceleration voltage. Note that the scales vary in the different images. The figure is adapted from Paper I.

To summarize this section, none of the films in this study formed the single fcc phase that is expected for HEA. At high temperatures, the materials appeared to be close to equilibrium and formed the multiple phases that are seen

in annealing studies [30,32]. At low temperatures, the atomic diffusion was very limited, and the phase selection was, therefore, kinetically controlled.

These results illustrate the two simultaneous effects that an increase in energy input has on the phase selection: a change in the thermodynamic equilibrium state, and an enhanced ability to diffuse toward the equilibrium state. This was exemplified by the change in the relative amount of the fcc phase in the films. At the lowest energy (the RT sample deposited with floating bias), the fcc phase is favored by kinetics. When applying a bias voltage, the relative amount of fcc decreased, as the ability to form the more complex χ phase was improved. However, at even higher energy input, in the films deposited with substrate heating, the fcc phase was favored again. This time it was due to thermodynamics, as it was stabilized by the high entropy, and the high atom mobility allowed the material to rapidly approach equilibrium. If both these effects were to be further enhanced, we should see a single-phase material when sputtering above 800 °C, according to the CALPHAD calculations in Figure 3. This is, however, outside the limits of our deposition system.

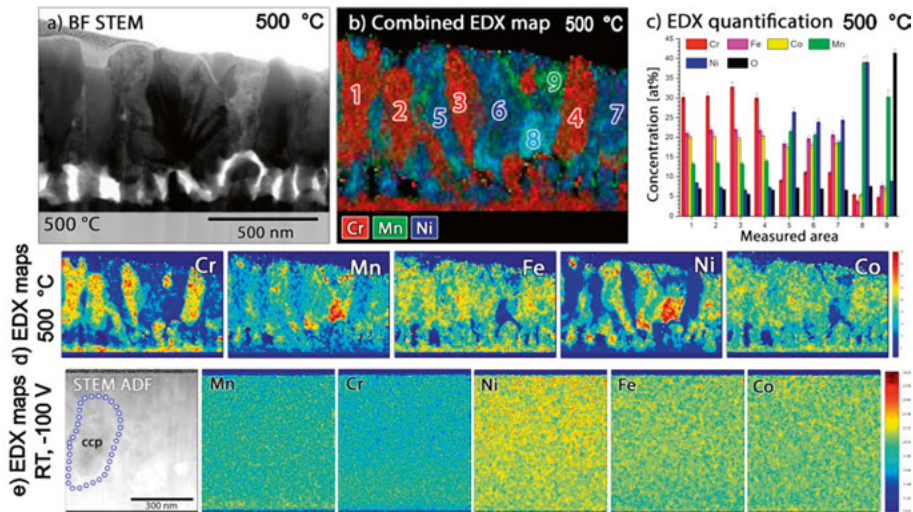


Figure 10. Maps of elemental distribution, measured by EDX in TEM on cross-section samples prepared with a FIB. a) – d) depict the analysis of the sample deposited at 500 °C, while e) depicts the -100 V sample, deposited without heating. The figure is adapted from Paper I.

6.1.2. Phase formation mechanisms

The secondary aim of Paper I was to understand why a single fcc phase was reported in certain studies of sputtered coatings while others obtained multi-phase materials [32–37]. In this section, the phase formation mechanisms are described, the fundamental differences between the two synthesis methods are

defined, and the conditions needed to achieve a single fcc phase in the coating are discussed. The different synthesis routes are visualized in Figure 11.

The left path in Figure 11 depicts the solidification of the bulk alloy from the melt and the subsequent annealing. At temperatures above 800 °C, a single fcc phase is thermodynamically stable, and therefore, this phase is first nucleated from the melt. As the sample is cooled, the other phases become favorable but to precipitate them solid-state diffusion and nucleation are required. The diffusion is slow in a typical bulk alloy with grains in the μm -mm range. Laplanche et al. [83] studied the kinetics of the phase decomposition in CoCrFeMnNi and found that to form σ precipitates, the cooling rate needs to be lower than 0.02 K/s. In the methods used to synthesize bulk HEAs, such as arc-melting, the cooling rates are much higher, and thus the initially formed fcc phase remains. The multiple equilibrium phases can form during prolonged annealing [30], a process that can be accelerated by smaller grain sizes [31,84].

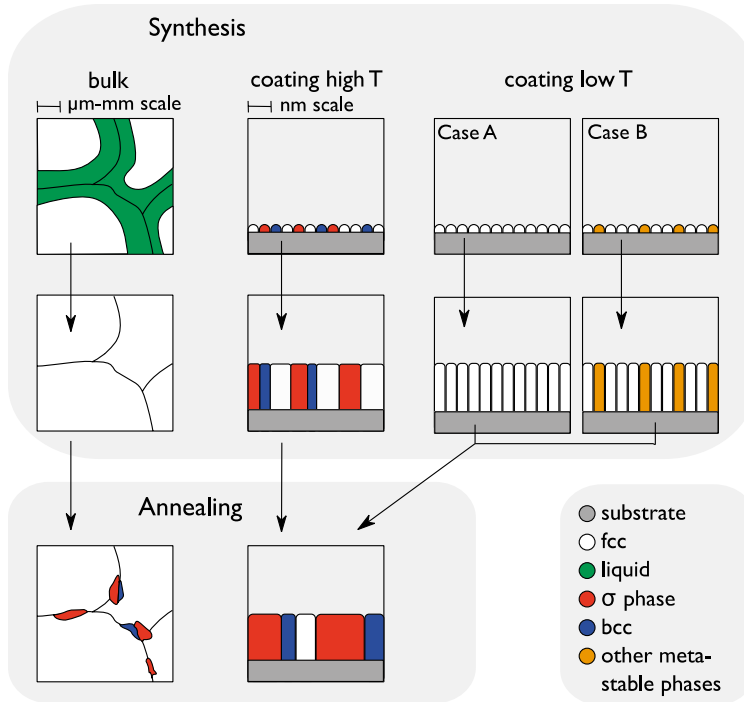


Figure 11. Phase formation mechanisms for CoCrFeMnNi during bulk synthesis from the melt, coating deposition at low and high substrate temperatures, and subsequent annealing. The figure is adapted from Paper I.

During magnetron sputtering, on the other hand, the atoms are quenched from the gas directly to the temperature at the surface of the growing film. In a typical deposition, this is below 800 °C, meaning that the synthesis occurs in

the multi-phase region (see Figure 3). This is the first fundamental difference between the methods and the reason why a single-phase material should not necessarily be expected. The phase formation follows different paths depending on the substrate temperature. When the temperature is high (middle route in Figure 11), the multiple equilibrium phases can form through rapid diffusion at the surface and in the grain boundaries. This diffusion is enhanced by the fact that the grains in magnetron sputtered coatings typically are nanocrystalline, which can be compared to the micro-millimeter-sized grains of bulk materials. When the substrate temperature is low (right route in Figure 11), the phase formation is kinetically controlled, and either a single fcc phase (Case A) or other meta-stable phases and phase mixtures (Case B) are formed. In all the literature studies, the deposition was performed without heating, and the phase selection is, therefore, best described as Case A vs Case B. No obvious difference regarding the remaining deposition parameters (such as the bias voltage, target-substrate distance, target powers, etc.) could be found between the studies. It appears that the selection of phases is sensitive to small changes in the deposition conditions, including differences in the specific plasma conditions of the chambers which cannot be identified through the deposition parameters but could be better understood through plasma diagnostics. As will be shown in Section 6.1.4., the selected substrate has a great influence on the phase formation of the coatings in the kinetic regime.

6.1.3. Literature review: Single-phase or multi-phase formation in magnetron sputtered multicomponent alloys

The literature on magnetron sputtered multicomponent alloy (MCAs) films was reviewed to investigate whether the principles found for CoCrFeMnNi can be applied to HEAs in general. The scope of the review is presented below, followed by a summary of the results, an analysis based on the mechanisms proposed in the previous section, and lastly, some notable examples of alloys.

The review was a summary of studies available in March 2021 and included coatings of the two most well-studied groups of MCAs [16]. The first is the 3d transition metal group (marked in orange in Figure 12). These alloys, which include the Cantor alloy, usually form an fcc phase. The second group (marked in blue) is the refractory metal group. These alloys crystallize with a bcc structure and consist of metals known for their high hardness and heat resistance. Alloys were included in the review if they were described as MCAs or HEAs and had four or more elements, so long as most of those elements belonged to the defined groups. A record was kept of the atomic compositions, the reported phases, any substrate heating, and post-deposition annealing. The full list of studies and data is found as an appendix to this thesis. The general trends are visualized in Figure 13.

Fewer studies on refractory metal MCAs were found; only 17 examples. In this group, more than half of the cases used substrate heating. Ten studies reported a single bcc phase, which was achieved both without heating and with heating of up to 350 °C. Three cases of multiple phases were found, achieved by using substrate heating of 450 °C and above. Three studies obtained amorphous or X-ray amorphous films without heating. Finally, six of the studies annealed the bcc films and found that the single phase was retained at temperatures above 700 °C. The longest annealing was performed at 1100 °C for 3 days.

These results indicate that the proposed mechanisms in Figure 11 are valid for many, perhaps most, of the alloys in these groups. In the 3d transition metal group, almost every single-phase material was obtained through synthesis close to room temperature. It is, therefore, apparent that the stabilization of a single phase is highly dependent on kinetics (as in Figure 11, Case A). The number of reported multiphase materials is relatively low, which could be evidence of kinetic stabilization of the simple crystal structure above more complex intermetallics, but it could also partly be due to the under-reporting of multi-phase films. The decomposition of the fcc phase with any type of heating (following Figure 11, high T or annealing) demonstrates the generally low thermal stability of the coatings in this group. The refractory metals form more thermally stable MCAs with a bcc structure, which is expected. However, while the higher bond strengths of these metals shift all the diffusion processes to higher temperatures, there is no evidence that the core principles differ.

In the introduction, it was discussed how few equimolar alloys may possess a thermodynamically stable single-phase region. The importance of this observation for sputter deposition can now be evaluated. Several alloys from the literature review were selected and their equilibrium phases were calculated using the CALPHAD method. It was found that some alloys that formed a single fcc phase in the films, did not exhibit any temperature region where the single phase was stable. A notable example was in the FeCoNiNb system, where the fcc phase was predicted to be mixed with intermetallic phases at all temperatures. In the coatings, a single fcc phase could be achieved at certain process conditions and favored by, for example, increasing the target power [85]. The same principles seem to apply to CoCrFeMnNiV [34], CoCrCuFeNbNi [86], and CrNbTaTiW [57], once more emphasizing the importance of kinetics in determining the phase composition.

6.1.4. The effect of the substrate on phase formation

In Paper I, all the CoCrFeMnNi coatings were deposited on amorphous Si oxide substrates, and a single fcc phase was never observed within the explored parameter space. It was only when the alloy was deposited on other types of substrates that a single phase was achieved. This is another kind of kinetic stabilization. Figure 14 displays diffractograms of the Cantor alloy

deposited on four different substrate materials. They were all deposited without substrate heating and with a high substrate bias, meaning that the synthesis was under kinetic control (Case A or Case B in Figure 11) but with enhanced adatom mobility. The target power and working pressure were similar for all the depositions, between 0.4-0.7 Pa and between 150 and 180 W.

The coatings deposited on SiO₂ and polyimide formed the same phases seen in Section 6.1.1: a mixture of fcc and χ phase. The coatings on polycrystalline 316L stainless steel and 0001-oriented Al₂O₃, on the other hand, formed a single fcc phase. This can be explained by epitaxial stabilization, which means that the energy of nucleation of certain phases is lowered if there is a crystallographic relationship to the underlying matrix.

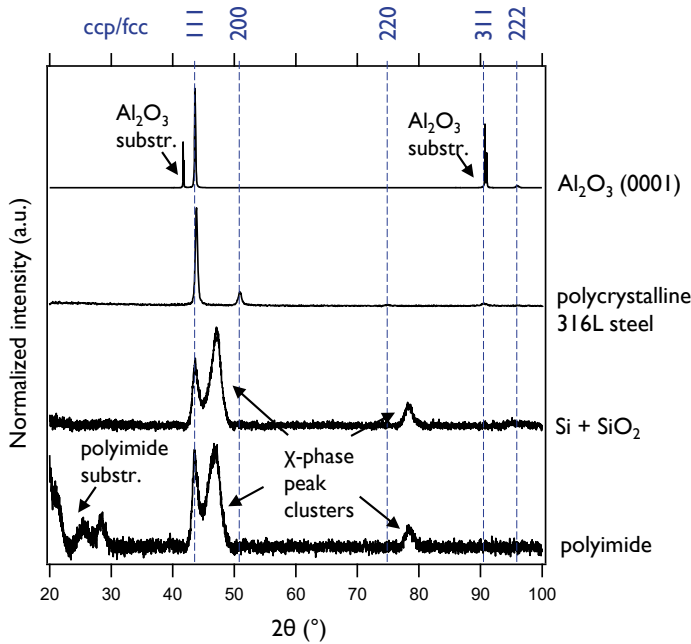


Figure 14. Diffractograms of CoCrFeMnNi coatings deposited under similar deposition conditions on different substrates. The data is from Paper I, Paper II, and Paper V and unpublished material.

When growing on amorphous substrates, like SiO₂ or polyimide, no matching is possible. They are neutral substrates. For 316L SS substrates, the crystal structure of the coating and the substrate are the same. The coating can, therefore, grow by a simple cube-on-cube relationship. The lattice mismatch (in %) is defined by

$$\frac{a_{\text{coating}} - a_{\text{substrate}}}{a_{\text{substrate}}} \times 100 \quad \text{Eq. 5}$$

where a_{coating} and $a_{\text{substrate}}$ are the relevant lattice parameters. It is almost 0% for the Cantor alloy on 316L (the reported bulk cell parameters of the two materials overlap). It is commonly accepted that coatings with a mismatch smaller than 10 % can grow epitaxially [87]. The proposed relationship between the (0001)-oriented Al_2O_3 and the Cantor alloy is described in refs [88,89]. The lattice mismatch is higher in this case, 7.6 %, which should make epitaxial growth less favorable since the coatings would be more strained. It was indeed found that the formation of a single phase was more sensitive to changes in the deposition conditions than when growing the coatings on 316L SS. For example, a small change in the target-substrate distance or the angle between the magnetrons was enough to cause a shift to multi-phase formation.

6.1.5. Depositing the Cantor alloy on stainless steel – a study of surface energies, growth modes, and stacking faults

In this section, the growth of CoCrFeMnNi on polycrystalline stainless-steel substrates was explored in greater detail. There were multiple motivations for this study, the first being that steel is the substrate material for several of the potential applications of these coatings, such as the bipolar plates in fuel cells or electrolyzers. In lab-scale research, single crystalline substrates are most often used since they are standardized and simplify the analysis. However, considering how strongly the substrate affects the growth of the coatings, it is important to use substrates more similar to the intended application already in the early stages of materials design.

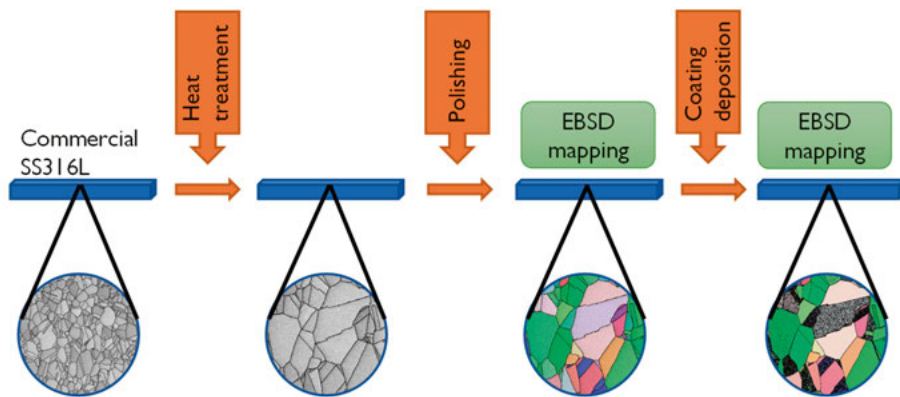


Figure 15. Methodology for studying the growth of coatings on polycrystalline stainless steel substrates. Adapted from Paper II.

The second motivation is understanding the effects of substrate orientation on the coatings. Single crystalline substrates are usually available in a few different crystal orientations (such as 100, 110, and 111), and the choice of orientation can strongly affect the growth behavior of the coatings [90,91]. By using a polycrystalline substrate with a near-random orientation of grains, the trends relating to substrate orientation can be viewed more clearly and with better statistics.

The methodology of the study is schematically shown in Figure 15. Polycrystalline steel substrates were first annealed to enlarge the grains to simplify the analysis. They were then polished to achieve a smooth surface suitable for EBSD analysis. The substrates were then analyzed with EBSD. After the coating experiments, the same area was analyzed with EBSD, making it possible to compare the orientation of the coating relative to the individual substrate grains. Multiple methods were then used to characterize the coating on differently oriented grains.

Influence of substrate orientation on morphology and growth rate

The following section explores the effect of the orientation on the texture, morphology, and growth rate. These results are from Paper II, although some additional unpublished results are also included. Figure 16 shows a top-view SEM micrograph of a 500 nm thick Cantor alloy coating at a grain junction of a polycrystalline 316L stainless steel. The substrate grain boundary is marked with a dashed line, but it is clearly visible due to the distinct coating morphology on the different grains, which varies from nanometer-scale rounded grains to completely smooth.

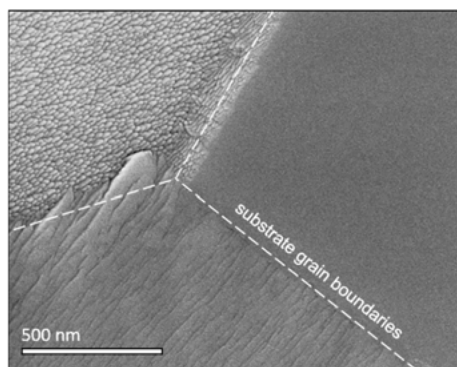


Figure 16. Topview SEM micrograph of a coating of CoCrFeMnNi deposited on 316L stainless steel, showing a grain junction between three different substrate grains. The coating was deposited using a substrate bias of -100 V. Unpublished data.

These differences were studied systematically following the method shown in Figure 15. In a preliminary study, the deposition temperature, working pressure, target power, and substrate bias were varied. It was found that the substrate bias had the greatest effect on the morphology. At a floating potential (no bias), the coating grew with a columnar microstructure and the morphology had no strong substrate dependence. With an increase in bias, the substrate dependence was enhanced. The focus in this section will, therefore, be on the coatings deposited with the highest applied bias: -100V.

Figure 17 (a) and (b) show EBSD maps of an area of the sample before and after depositing a 500 nm thick CoCrFeMnNi coating. On most grains, the detected orientation of the coating was the same as that of the underlying substrate. This confirms that the coating grew with a strong epitaxial relationship to the substrate. On certain grains, the orientation of the coating could not be assigned, which then appears as a black pixel on the map. The thicker the coating grew, the more areas with unassigned pixels were found. Furthermore, they were found preferentially on blue, cyan, purple, and pink grains, meaning that they had orientations close to [111]. The distribution of orientations can be visualized using inverse pole figure (IPF) scatter plots. Figure 17 (c) displays the orientations of the substrate and while Figure 17 (d) and (e) show

the distribution of orientations in coatings deposited under the same conditions but to different thicknesses: 100 nm and 500 nm, respectively. The substrate and the thinner coating displayed a near-random distribution of orientations. However, at a thickness of 500 nm, orientations close to $[111]$ and $[001]$ were missing from the scatter plot, confirming the observation that more unassigned areas were found. The reason for this was later revealed to be the formation of stacking fault structures, which is shown in the TEM studies in the next section.

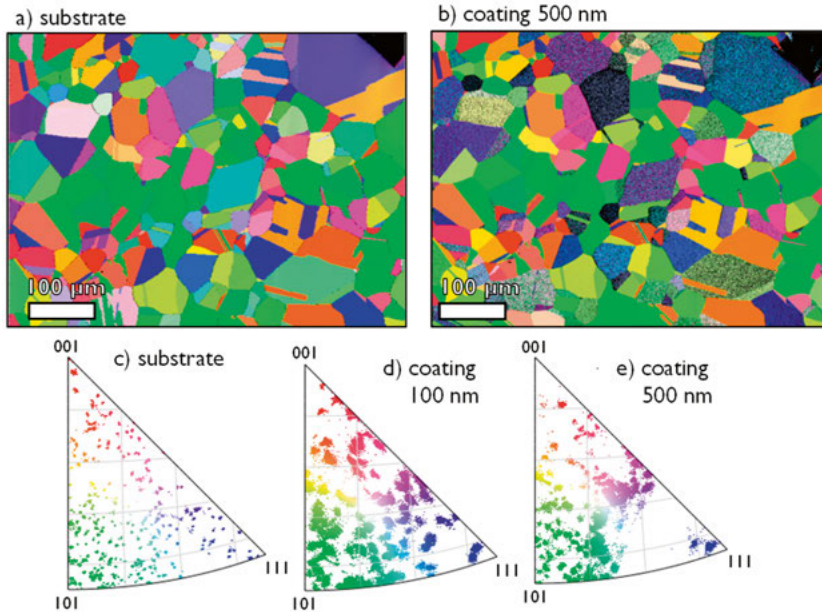


Figure 17. a) EBSD of a 316L substrate prior to deposition, b) EBSD of the 500 nm thick Cantor alloy coating deposited with -100 V substrate bias c) IPF scatter plot of the substrate grain orientations, d) IPF scatter plot of a 100 nm thick and e) a 500 nm thick Cantor alloy coating. Adapted from Paper II.

Figure 18 displays top-view and cross-section band contrast images of the CoCrFeMnNi coating deposited on $[102]$ -adjacent and $[111]$ -adjacent substrate grains. On the $[102]$ -adjacent grains, the coating was completely smooth and appeared to be free of grain boundaries. The TKD image in Figure 18 (e) shows that the orientation of the coating was exactly the same as the substrate. This means that, on the $[102]$ -adjacent grains, the coating grew as perfectly epitaxial single crystals. The single-crystalline sections of the coatings appear to be as large as the substrate grains, which can be up to 100 μm in diameter.

On the $[111]$ -adjacent substrate grains, the coatings had a completely different morphology. The grains appeared rounded in the top-view and were found, with cross-section studied, to be columnar. TKD of the cross-section sample showed that the substrate was $[343]$ -orientated (i.e. $[111]$ -adjacent).

The coating had two distinct crystal orientations, intermixed in the whole coating [343] and [232]. Most of the coating could not be indexed with TKD.

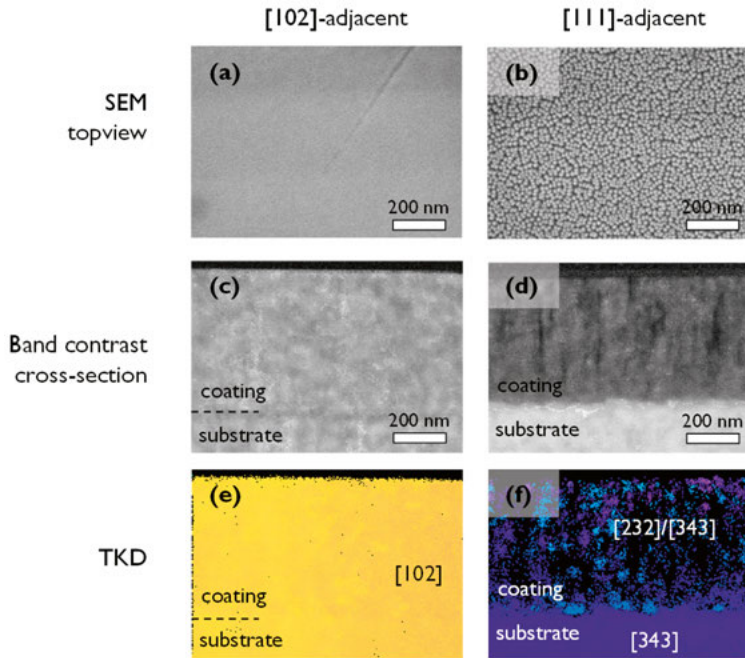


Figure 18. A CoCrFeMnNi coating on stainless steel deposited using -100 V on [102] and [111]-adjacent substrate grains, depicted using a-b) top-view SEM c-d) cross-section band contrast imaging (e-f) TKD. Adapted from Paper II.

The samples were also mapped using profilometry, which revealed that the thickness of the coatings varied by about 10% over the surface. To examine if the effect was related to the substrate orientation, the heights on different grains were displayed in an inverse pole figure scatter plot, shown in Figure 19(a). A clear trend could then be seen. The thinnest and thickest part of the coatings were found on the [111] and [102]-adjacent grains, respectively.

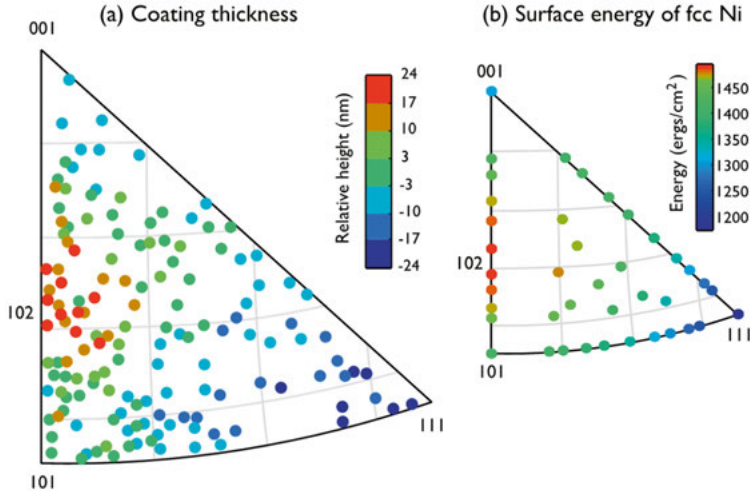


Figure 19. Inverse pole figure scatter plots showing (a) the relative thickness of the coating on different orientations and (b) the surface energy of Ni (data from ref [92]) The figure is adapted from Paper II.

In the literature, the morphology of magnetron sputtered coatings is usually described based on structure zone models, SZMs (see e.g. ref. [93]), where the microstructure is assumed to be dependent on the deposition temperature, pressure, and/or ion bombardment. These parameters influence the surface diffusion rate of adsorbed atoms, and therefore, the final microstructure. The results in Paper II, however, show that completely different microstructures can be obtained from the same deposition on different grains. This means that the typical SZM cannot be applied to explain the growth behavior on some substrates.

The texture development during magnetron sputtering is often described as a competition between atomic planes with different surface energies (see e.g. ref [94]). These models, however, can only be applied to neutral substrates, i.e. substrates not influencing the growth. Furthermore, to apply this model, the regions with competing orientations have to be small (nanometer-scale [95]), allowing diffusion of atoms between them. This is obviously not the case in the present study, where the regions with different orientations are in the order of 10-100 μm .

The reason behind the large differences in morphology and growth rate observed in Paper II has not yet been fully identified. It would require fundamental knowledge of the surface reactions on each of the crystal orientations and, to our knowledge, this has not been well-studied for the growth of either pure fcc metals or fcc alloys. However, a possible mechanism was proposed. The most interesting clue is displayed in Figure 19(b). Here, the surface energies of an fcc metal (Ni) were visualized in an IPF scatter plot. There appears to be a connection between the surface energies and the trends in morphology

and growth rate. Firstly, the large, epitaxial grains in Figure 18 were formed on the grains with the highest surface energy, while the columnar growth of more randomly oriented crystallites was observed on grains with the lowest surface energy. Secondly, there was a remarkably similar trend between the coating thickness and the surface energy (Compare Figure 19(a) and (b)). It appears that the coating thickness and the surface energy increased in the same order, from [111] to [102]. The dependence was not linear, as can be seen from the color scale bars.

Several explanations were considered relating the surface energies to, for example, the sticking coefficient [96,97] or the re-sputtering rate [98]. However, in each case, no evidence could be found that this effect was dominating or that it should result in the trends shown above. It was also considered that the rougher surface could increase the re-sputtering on [111]-adjacent grains, leading to a thinning of the coating on these grains [99]. This does, however, not explain why the morphologies differed in the first place.

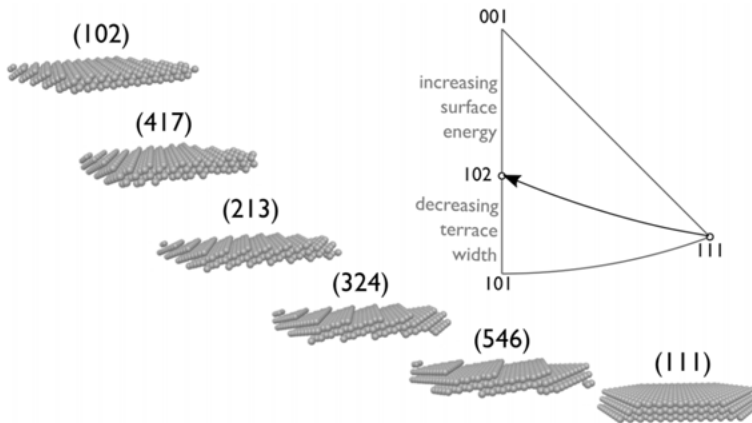


Figure 20. Schematic image of ideal surfaces of the fcc phase in different orientations. The surfaces from 111 to 102 have increasing surface energies and decreasing widths of the 111-like terraces.

The most plausible hypothesis for the difference in morphology is related to the surface structures on different crystal orientations. It has been predicted through theoretical methods that the adatom diffusion should be most rapid on the low energy (111)-surface, and slower on the higher energy surfaces [100,101]. This is related to the density of step edges. In Figure 20, ideal models of the surfaces of the different orientations are displayed. The (111)-surface is perfectly smooth, as it consists of a close-packed plane. Surfaces close to (111) can be seen as tilted (111)-terraces separated by surface steps. These are known as vicinal (111) surfaces. When moving from (111) to (102), the terrace width decreases, meaning that the density of steps increases. This change is important because it has been shown that the presence of step edges is crucial in the nucleation and growth process. Atoms can more easily stick

to an edge position. On surfaces with many steps, the atoms will therefore stay closer to where they land. This means that the coating can more easily grow layer-by-layer, also known as 2D growth. It has been shown experimentally that surfaces with steps more easily lead to the growth of large, epitaxial single crystals [102]. The atoms arriving at the (111) surface, on the other hand, can diffuse over longer distances. This allows for clustering and changes the growth mode to a 3D or island growth.

Influence of substrate orientation on stacking fault structures

As discussed in the introduction, one of the interesting features of the Cantor alloy is that it has a relatively low stacking fault energy. This means that it can easily form twin boundaries. Twinning has been reported in the literature to be the primary deformation mode at low temperatures, making the Cantor alloy one of the toughest alloys at cryogenic temperatures [41]. In bulk CoCrFeMnNi, twins form under stress when the alloy is deformed. In magnetron sputtered coatings, however, twins can be present already in the as-deposited coatings. In this section, the influence of the substrate on the formation of stacking faults will be explored. The results in this section are unpublished and will be complemented with further TEM investigation and theoretical work in a future paper.

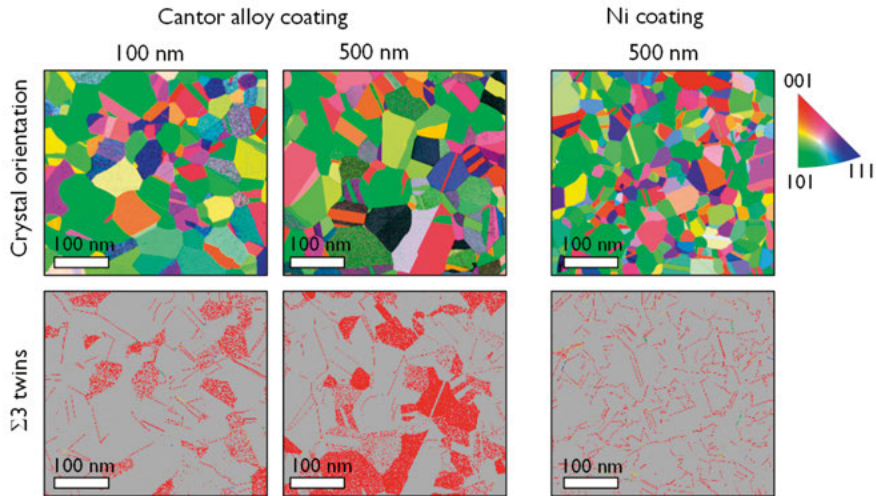


Figure 21. Maps showing the orientation of the fcc crystal grains and $\Sigma 3$ twins in CoCrFeMnNi coatings deposited to a thickness of 100 nm and 500 nm, respectively, as well as a coating of pure Ni deposited to a thickness of 500 nm under the same conditions. Unpublished data.

The previous study of the EBSD maps (in Figure 17) showed that there were areas where the coating could not be fully indexed. Using the same data, maps were generated highlighting the interphases between grains that had a 60° rotation in the 111 planes. This rotation means that the two adjacent

crystals are crystallographic twins, specifically $\Sigma 3$ twins. Figure 21 displays such maps for Cantor alloy coatings deposited to two different thicknesses: 100 and 500 nm and a pure Ni coating deposited to a thickness of 500 nm under the same deposition conditions. Some of the grain boundaries of the substrate in all three samples were found to have this twinning relationship. In the Cantor alloy coatings, twins were also found in the coating. The areas of the coatings that had poor indexing in EBSD (low hit rate) also had a high density of $\Sigma 3$ twins. As shown in Figure 17, there was a larger number of areas with a low hit rate in the thicker coating. This was reflected in an increased number of twins. In the pure Ni sample, there were almost no regions with low hit rate, and accordingly, no $\Sigma 3$ twins were seen except for in between the substrate grains. The higher density of $\Sigma 3 \{111\}$ twins in the Cantor alloys compared to Ni can be explained by the lower stacking fault energy of the alloy. The energies are 125 J/m^2 for Ni [43] and 21 mJ/m^2 for the Cantor alloy [45].

The coatings were then studied using 4D-STEM. Figure 22(b) shows the diffraction patterns found in the substrate and the coating on a single $[111]$ -adjacent substrate grain. The substrate was easily identified as pure fcc, while in the coating, different patterns were found at different distances from the substrate. The thickness dependence will be discussed later. For now, it can be concluded that the patterns can be identified as fcc with different stacking fault structures. The different stackings are depicted in Figure 22 (a).

Part of the coating was “perfect” fcc meaning that it did not have a high density of stacking faults. A streaking (blurring in one direction) of the diffraction pattern was found in part of the coating. This is evidence of a high density of intrinsic stacking faults (e.g. ABCABABCABC). The disordered stacking fault could be observed with high-resolution TEM (see Figure 22 (d)).

There were also two different ordered stacking fault structures, which gave rise to additional spots rather than streaking. The two structures could be separated since the additional spots had different intensities, as can be seen in the integrated patterns in Figure 22(b). Part of the coating was dominated by twinning, which is when the order in stacking is reversed (e.g. ABCABCBACBA). Another part of the coating was identified as a mixture of fcc and the more complex 9R structure. 9R can be described as a stacking fault in every third plane (ABCABCBACABCABC).

The 9R structure has been observed previously in magnetron sputtered fcc metals and alloys [103], including a high entropy alloy [104]. Their formation can be explained by the presence of the $\Sigma 3 \{111\}$ twin boundaries which are truncated by short $\Sigma 3 \{112\}$ incoherent twin boundaries (ITBs) [105]. The $\Sigma 3 \{112\}$ ITBs can be described as partial Shockley dislocations giving rise to an ordered stacking sequence of 9R. The formation of such 9R stacking sequences is facilitated by stress [105].

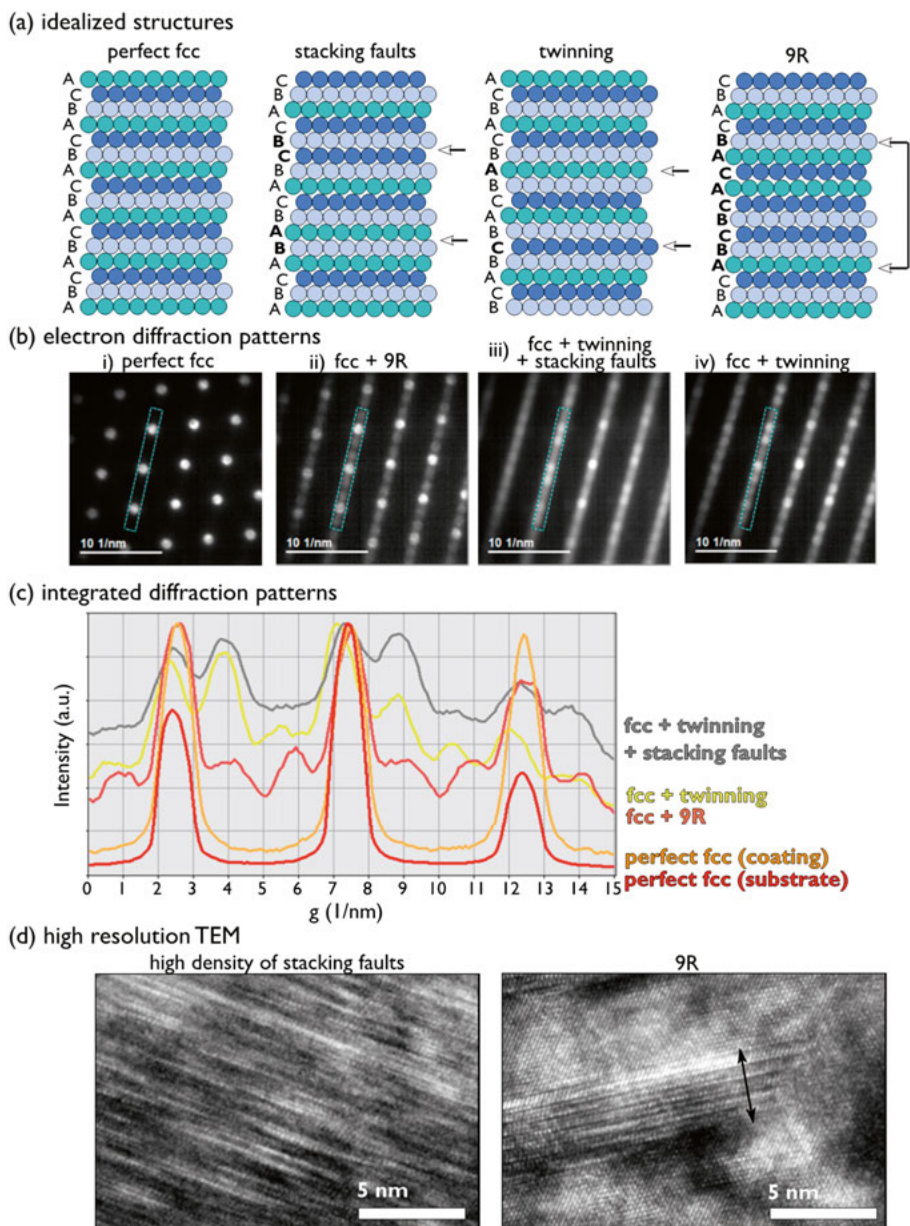


Figure 22. (a) Schematic images of different stacking structures (layers A, B, and C are the closed-packed 111-planes), (b) electron diffraction patterns acquired with 4D STEM from different regions of a Cantor alloy coating on a single [111]-adjacent substrate grain, (c) integrated intensities from the blue areas of the diffraction patterns in (b), and (d) high-resolution TEM images of two areas dominated by disordered stacking faults and fcc with 9R regions, respectively. The thickness marked with a black arrow consists of two repeated 9R sequences and stretches between two column boundaries in the coating. Unpublished data.

The width of the 9R region has been estimated for other metals. In Ag, for example, it was found to be only about 1 nm [105]. Our results, however, showed that the 9R regions were considerably broader in the coatings. This can be seen in Figure 22 (d), where the 9R region was more than 10 nm in width. The 9R regions often extended over an entire column (10-20 nm). The reason for such an extensive formation of ordered stacking fault structures is unclear, but calculations with density functional theory (DFT) are on-going to determine the stability of a 9R structure compared to fcc.

The maps in Figure 21 showed that the prevalence of nanotwins was higher on the [111]-adjacent grains. It also showed that the number of orientations with twins increased as the coating grew. Figure 23 clarifies the orientation dependence. TEM images recorded with a high-angle annular dark field (HAADF) detector and the integrated diffraction patterns from different layers of the coatings are displayed for three orientations: [102], [314], and [223] (a [111]-adjacent orientation).

The [102]-oriented grain had no features that could be seen in the micrograph, such as grains or columns, and the patterns of the grain and the coating were almost perfectly overlapping. This means that the entire coating consisted of fcc with no stacking faults. On the [314]-oriented grain, the first 70 nm of the coating were “perfect” fcc. The next layer was also around 70 nm and consisted of fcc mixed with the 9R structure. The rest of the layer was dominated by twinning. On the [223]-oriented grain, there was no “perfect” fcc layer. The coating closest to the substrate consisted of fcc and 9R, followed by two layers dominated by twinning and stacking faults, respectively.

This type of study was performed in TEM for many grains with different orientations. It was found that the layers with different stacking fault structures were found in the same order from the substrate to the surface: the pure fcc layer, when present, was always found closest to the substrate, followed by layers dominated by 9R, twinning, and finally stacking faults. Not all layers were found on all grains, and the different structures were often intermixed.

To clarify the orientation dependence with better statistics, the thickness of the first coating layer (fcc) is presented in a pole figure scatter plot in Figure 23(c). On the orientations close to [102] and [101], the fcc layer was around 500 nm, meaning that the whole coating was fcc. When moving toward [111] in the IPF, the stacking fault structures initiated closer to the substrate. On certain [111]-adjacent orientations, such as the [223]-oriented grain depicted in Figure 23, no fcc layer was present.

The reason behind this trend has not yet been established. A possible explanation is that the nanocrystalline, columnar morphology of the [111]-adjacent coatings promotes the initiation of stacking faults and, consequently, 9R stacking. Another reason could be that there was an increasing strain with the coating thickness and that the strain evolution is different depending on the crystal orientation. This will be further explored in the ongoing study.

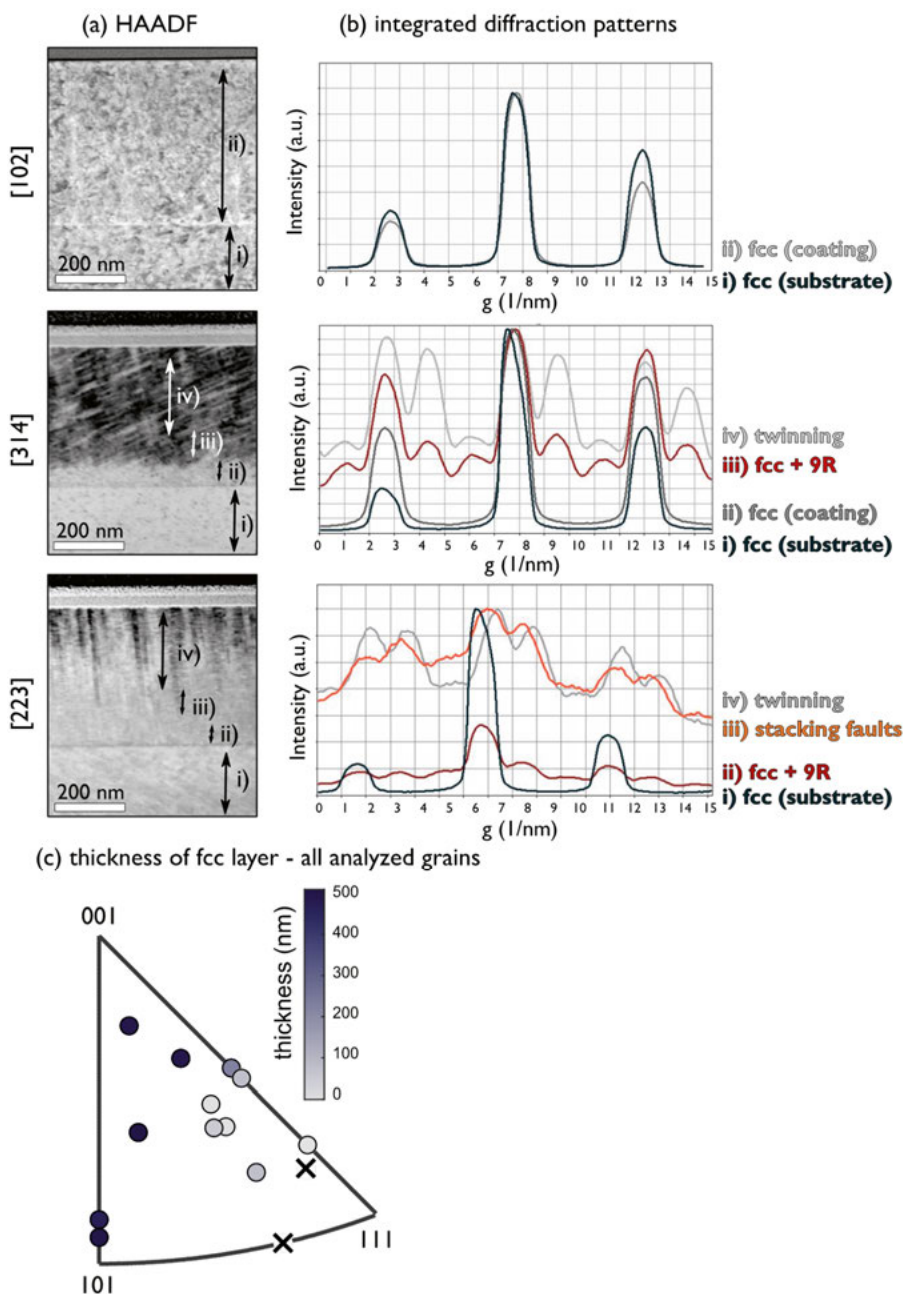


Figure 23. (a) HAADF images and (b) integrated diffraction patterns of the Cantor alloy coating on three substrate grains. (c) inverse pole figure scatter plot displaying the thickness of the fcc layer in the coating on a number of substrate grains with different orientations. The crosses represent orientations where the stacking fault structures reached the substrate so the fcc layer thickness was zero. Unpublished data.

Implications of the substrate dependence on coating properties

To conclude, the study of the Cantor alloy showed that the orientation of the substrate strongly affects the growth mode, the morphology, the deposition rate, and the density and type of stacking faults in the coatings. In planned future studies, the effects of these features on the coating properties will be explored. Tensile tests will be used to study the ductility of the coatings, mapping with nanoindentation to investigate the hardness, and electrochemical studies to explore the corrosion mechanisms and quantify the corrosion rates. This could have important implications for the applications of HEAs and other fcc alloys deposited on stainless steel. The orientation distribution of a steel component can, to some extent, be tuned by parameters during forming and post-annealing. If the substrate-coating interactions are considered, the substrate texture could be used to, for example, lower the overall corrosion rates or increase the crack resistance of a component.

A preliminary corrosion study was performed on the samples deposited with -100 V bias on 316L. The samples were corroded rapidly by applying a potential of 1 V vs Ag/AgCl in a 0.5 M H_2SO_4 solution. This is in the trans-passive region, where Cr, which usually protects the alloy by forming a passivation oxide layer, forms soluble species. It was observed that the coating dissolved more rapidly on some of the grains, which was attributed to the rough morphology. It would be interesting to study these materials with localized electrochemical techniques to measure the electrochemical response of the coating on each grain.

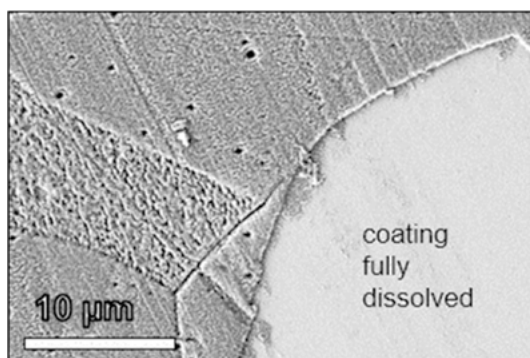


Figure 24. SEM micrograph of a CoCrFeMnNi coating on a 316L substrate after polarization to 1 V for 3 hours in 0.5 M H_2SO_4 . The coating was fully dissolved only on some of the substrate grains. Unpublished data.

6.2. Synthesis of amorphous multicomponent alloys

In Paper III, two four-component systems, CrFeNiTa and CrFeNiW were investigated. The calculated phase fractions of four selected alloy compositions are presented in Figure 25. They are the alloys with the lowest and highest concentrations of Ta and W, respectively, included in the study. Contrary to the calculations on the Cantor alloy (shown in Figure 3 (a)), no single-phase region was predicted for these alloy systems. Instead, the alloys were predicted to form phase mixtures with both solid solutions and intermetallic phases, with severe segregation of the elements. Additional calculations showed that the fcc phase can dissolve at most around 6 at% Ta or W. The bcc phase can dissolve 4 at% Ta and 10 at% W. The synthesis of these alloys at high temperatures, such as traditional melting and casting, would, therefore, lead to phase separation.

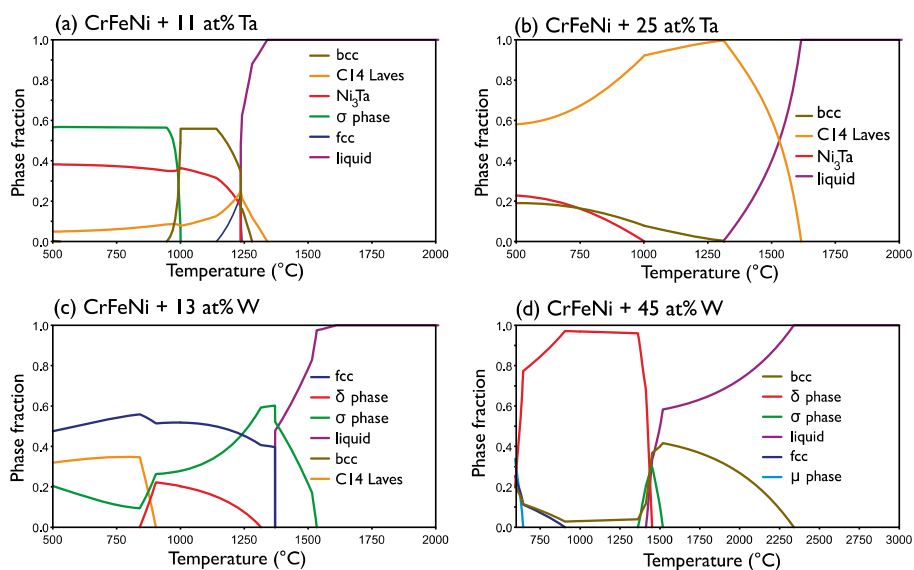


Figure 25. Calculated phase fraction diagrams of alloys in the CrFeNiTa and CrFeNiW systems, with Ta and W concentrations reflecting the highest and lowest concentrations found in the samples. Adapted from Paper III.

When depositing coatings in these materials systems, all the alloys in the composition range suppressed the formation of multiple phases. The diffraction study of the coatings is found in Paper III. Only one alloy formed a crystalline material. It was the alloy with 13 at% W, which was identified as a single fcc phase. All the remaining alloys formed, instead, a single amorphous phase. Electron diffraction in the TEM was performed on two selected samples (with 25 % Ta and 25% W) to rule out the presence of small crystallites. The morphology of the coatings was completely smooth and featureless, with no columns or grain boundaries found in SEM and STEM. Elemental maps

measured by EDS in TEM showed that the amorphous phase was also completely homogenous down to the nanometer scale.

There is only one report in the literature of X-ray amorphous CoCrFeMnNi, which was, furthermore, revealed with TEM to be partially nanocrystalline [106]. The reason why CrFeNiTa and CrFeNiW can form amorphous coatings more easily can be explained by several factors that favor the glass formation ability (GFA). A higher atomic size mismatch, δ , and a smaller enthalpy of mixing, ΔH_{mix} , promotes a higher GFA, as explained in Section 3.1.2. For equimolar CoCrFeMnNi, $\delta=0.92$ and $\Delta H_{\text{mix}} = -4.1$ kJ/mol which, according to Zhang et al. [26], is within the ranges for single-phase crystalline alloys. The values for the CrFeNiTa and CrFeNiW systems vary with the composition as illustrated in Figure 26. δ increased with the addition of both W and T, while ΔH_{mix} increased with added W and decreased with added Ta. The Ta concentrations of the alloys in this study were between 11 and 25 at%, meaning that the δ value of the Ta series varied between 5.0 and 6.7 while ΔH_{mix} was between -10 and -15 kJ/mol. The alloys in the CrFeNiW system had W concentrations between 13 and 45 at%, so δ was between 3.9 and 5.4, while ΔH_{mix} was between -3.7 and -2.0 kJ/mol.

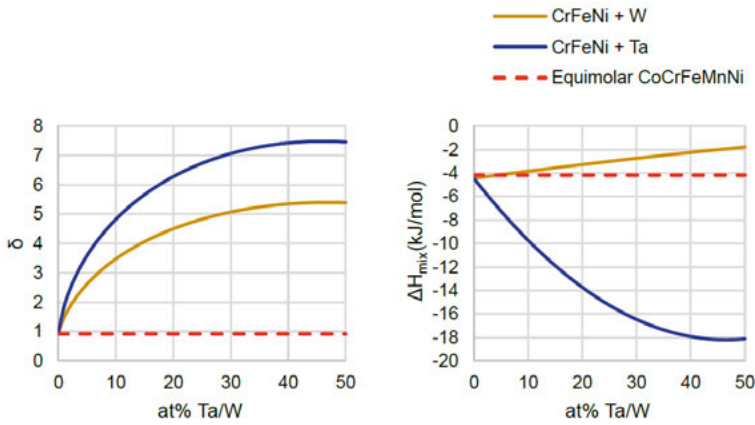


Figure 26. Parameters δ and ΔH_{mix} for the alloy CrFeNi with the addition of either Ta or W. The red dashed line is the value for equimolar CoCrFeMnNi. δ and ΔH_{mix} were calculated using equations 2 and 3, respectively, and values from ref [107] and ref [108], respectively. Adapted from Paper III.

Based on the classification by Zhang et al [26], the alloys in the CrFeNiTa system would be amorphous, while the CrFeNiW alloys fall in the regime of single-phase or ordered solid solutions. This explains why it was easier to form a crystalline alloy for the lowest W content. The formation of amorphous CrFeNiW at higher W concentrations is not unexpected. The cooling can be more rapid during magnetron sputtering at room temperature than for the methods used to produce bulk metallic glasses. Since the cooling rate is a limiting factor for glass formation, this would lead to a shift of the boundaries to

include lower d values and higher ΔH values. There are also other factors that favor amorphization that are not necessarily captured by the criteria by Zhang et al. The use of ΔH_{mix} as a predictor for glass formation is justified by the fact that it captures the range where the metals interact strongly enough to mix easily but not so strongly that they form stable intermetallics [26]. However, while the ΔH_{mix} of the binaries Cr-W, Fe-W, and Ni-W are all close to zero and similar to the binaries of the Cantor alloy, the enthalpies of formation, ΔH_f , of the binary compounds are considerably more negative [17]. This is reflected in the calculated phase fraction diagrams shown in Figure 25; the alloys have multiple stable intermetallic phases. This is further confirmed by studying the binary and ternary subsystems of CrFeNiW. At least two intermetallic phases with W exist in each of the Fe-W, Ni-W, Cr-Fe-W, and Fe-Ni-W subsystems. The existence of multiple intermetallics has been discussed as another predictor for glass formation. The glass-forming compositions of alloys are often found in the space between two intermetallics, where diffusion of elements into different domains is necessary for crystallization [109,110]. This is, for example, true for the glass forming alloy presented in Figure 3(c). This principle, combined with a low solubility of W in the solid solution phases of the CrFeNi alloy, means that crystallization should be relatively easy to suppress.

6. 3. Adding carbon to multicomponent alloys

Carbon was added to modify the equimolar alloy CoCrFeMnNi and the near-equimolar alloy $\text{Cr}_{27}\text{Fe}_{27}\text{Ni}_{26}\text{Ta}_{20}$ (henceforth referred to as CrFeNiTa for simplicity) to improve their mechanical properties and corrosion resistance. In the following sections, the synthesis of the modified materials will be explored. First, thermodynamic calculation will be used to predict the equilibrium phases of the alloys at different carbon concentrations. The results from the kinetically controlled synthesis will then be presented. The results are mainly from Paper VII, although some conclusions from Papers IV and V are included as well.

6.3.1. Thermodynamic calculations

Figure 27 shows the stable phases found at 500 °C at equilibrium for the two alloy systems, as a function of the carbon content. Due to the large number of phases, the diagram has been simplified by categorizing them into alloys (solid solutions and intermetallics), Cr-rich carbides, Ta-rich carbides, and graphite.

At higher temperatures, a small amount of carbon (~1 at% at 1200°C) was predicted to dissolve into the single fcc phase CoCrFeMnNi. This has been confirmed experimentally for CoCrFeMnNi [55,111]. At 500 °C, however, no carbon can be dissolved in either of the systems. The carbon should, instead,

form separate metal carbide phases. The mixed Cr-rich carbides $M_{23}C_6$, M_7C_3 , and Cr_2C_3 were found in both systems. TaC was also present in the CrFeNiTa system. At even higher carbon contents, a graphite phase was expected to form. Since the metal carbide phases were enriched in the stronger carbide-forming elements Cr and Ta, the alloy phases were depleted of the two metals. The depletion increased with the carbon concentration.

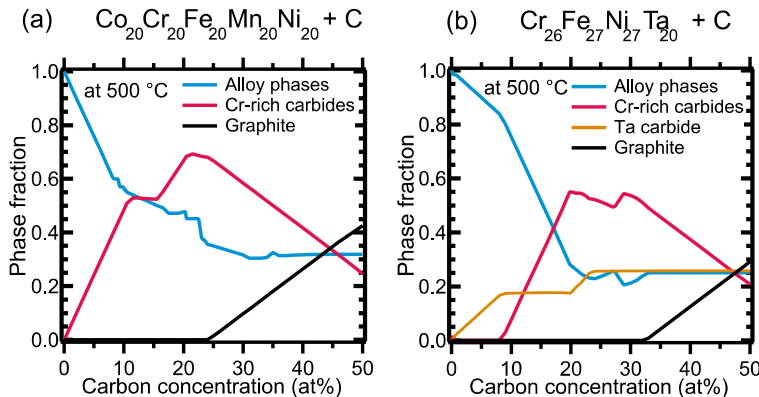


Figure 27. Phase fraction diagrams from CALPHAD thermodynamic calculations at 500°C on (a) the equimolar CoCrFeMnNi system and (b) the near-equi-molar CrFeNiTa system with up to 50 at% carbon. To simplify the diagrams, the alloy phases and the Cr-rich carbides were grouped. The alloy phases include fcc, bcc, σ phase, C14 Laves, and Ni_3Ta . The Cr-rich carbides are $M_{23}C_6$, M_7C_3 , and M_3C_2 . Adapted from Paper VII.

Based on these predictions, the carbon-containing materials would not be expected to possess the desired properties when manufactured via high-temperature syntheses, such as melting and casting. The depletion of Cr and Ta from the alloy phase could lead to areas where a stable passive layer cannot be formed, and the formation of carbide precipitates could make the material harder but would simultaneously lead to embrittlement. Similar results have been reported for the studies of the CoCrFeMnNiC system as a bulk material; the carbon increases the hardness and can also improve the corrosion resistance up to a very limited concentration. Above 1 at.% C the formation of the carbide phase causes both embrittlement and increased pitting corrosion [54,55]. The success of this design approach relies on the ability of sputter deposition to create materials far from thermodynamic equilibrium.

6.3.2. Amorphization and formation of composite coatings

The CoCrFeMnNi alloy was modified with between 6 and 49 at% carbon, while CrFeNiTa alloys were modified with between 22 and 44 at% carbon. All the coatings with added carbon were X-ray amorphous, and the amorphous structure was also confirmed with electron diffraction for CoCrFeMnNi with 11 and 49 at% carbon and CrFeNiTa with 22 and 44 at% carbon, ruling out

the presence of nanocrystallites. The carbon-free CoCrFeMnNi alloy was nanocrystalline and contained both an fcc and a χ phase, as explained in Section 6.1.1., while the CrFeNiTa alloy was amorphous even without carbon addition.

The formation of amorphous materials when adding carbon to sputtered metallic coatings is a well-known phenomenon [59]. To form these materials, crystallization must be avoided by, for example, rapid quenching from the melt or, in this case, through synthesis at low temperatures. With magnetron sputtering, the maximum solubility in alloys can be exceeded as supersaturated solutions of carbon can be formed by kinetic stabilization [56]. Amorphization typically occurs at an even higher carbon concentration, as the energy cost of dissolving more carbon increases, while the low mobility of the atoms suppresses the formation of the more complex crystalline carbides. In alloys, increasing the concentration of weak carbide-formers can progressively shift the amorphization to lower carbon contents [112]. In this case, the stronger carbide formers Cr and Ta were alloyed with very weak carbide formers Fe, Co, and Ni, which should promote the formation of amorphous materials. The chemical environment of the carbon was studied with XPS. It was found that the addition of carbon resulted in two phase-formation regimes.

The single-phase amorphous regime

At lower carbon contents, the carbon was fully incorporated into the amorphous alloy. The materials also appeared completely homogenous. One of the fundamental questions surrounding these materials systems was if the metallic elements would tend to segregate when carbon was added, due to the widely different carbon affinities, or if the carbon would be found bonded only to some of the metals. This was studied in-depth for the CoCrFeMnNi(C) system in Paper IV, using a combination of synchrotron techniques and TEM. It was found that all the metals were affected by the presence of carbon, even Ni and Co, which have very low carbon-affinities. The Ni, for example, displayed a less metallic environment when carbon was present. Furthermore, evidence was found that the segregation of elements did not increase with increasing carbon content.

The mechanical and electrochemical properties of the coatings were studied in depth in Paper V and Paper VI, to test whether the change from crystalline to amorphous, as well as the incorporation of more carbon into the amorphous phase, could improve the corrosion resistance and crack resistance.

The two-phase nanocomposite regime

At higher carbon contents, the carbon was, additionally, found as a segregated carbon-rich phase. This is displayed in Figure 28(a) and (b), where core-level C1s spectra from the two materials systems with around 20 – 50 at% carbon are presented. In all the samples, the lowest contributing peak was found at 282.9 - 283.1 eV, which is a typical binding energy for C-Me in the carbides

of the alloying elements and amorphous metal-carbon materials of similar composition [58,113,114]. At higher carbon contents, several peaks were found that corresponded to sp^2 and sp^3 hybridized C in a C-rich environment [115,116]. The sp^3 contribution was only around 20 % of the C-C signal, which means that the short-range order of the carbon phase was similar to graphite. The XRD analysis, however, showed no indication of a graphite phase and this phase is therefore in the following described as amorphous free carbon (a-C).

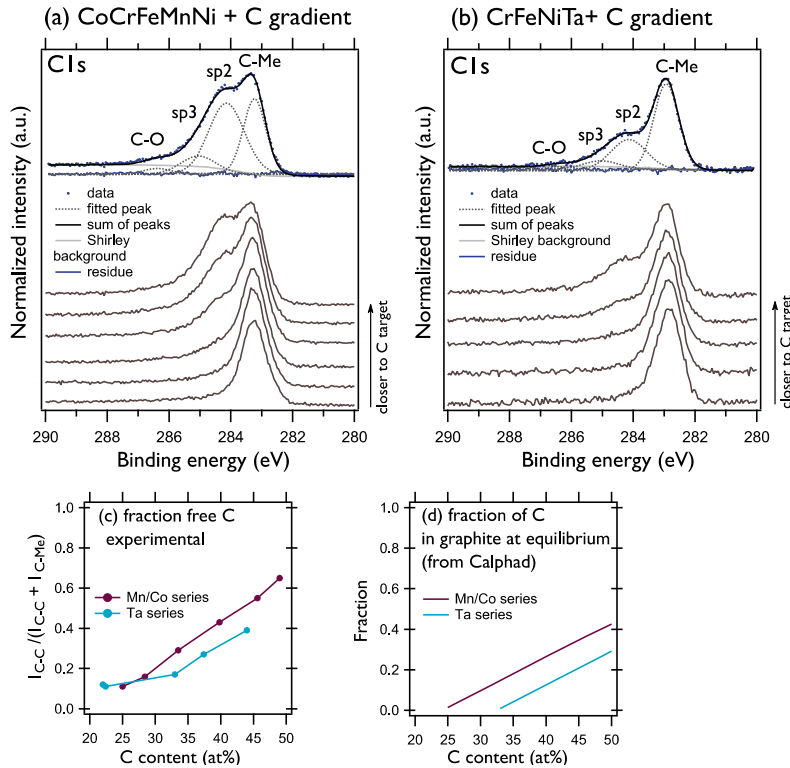


Figure 28. Results from XPS studies showing the C1s spectra of selected samples from (a) the CoCrFeMnNi system and (b) the CrFeNiTa system with added carbon, including an example of the fitted peaks. (c) shows the fraction of C-C carbon for each of the sample series while (d) shows the fraction of carbon found as graphite in the CALPHAD calculations at 500 °C. Adapted from Paper VII.

The existence of a segregated graphite phase above a certain carbon concentration was predicted with CALPHAD. The fraction of carbon found in the graphite phase at equilibrium is presented as a function of the carbon content in Figure 28(d). This can be compared to the experimentally determined fraction of a-C in Figure 28(c). The two graphs show the same trend: a free carbon phase was present from around 25 at% C in the CoCrFeMnNi system and around 30 at% C in the CrFeNiTa. (A baseline fraction of 0.1 was found

experimentally for all samples, regardless of the carbon content, and it was attributed to carbon contamination.) The amount of free carbon then increased linearly with the carbon content. For the same carbon concentration, more free carbon was present in the CoCrFeMnNi system than in CrFeNiTa. In other words, more carbon could be incorporated into the CrFeNiTa metal-rich phase. This should be expected since the average carbon affinity is higher in the CrFeNiTa alloy and the Ta forms more stable carbides than any of the other elements. The good agreement between the calculated and measured carbon phase is an example of how thermodynamic calculations are useful for understanding and predicting the phase formation in amorphous coatings, even though they are non-equilibrium materials.

The distribution of the carbon phase was observed through TEM studies, as shown in Figure 29. The a-C was visible in the TEM images and the EDS maps as a clustering around the grains of the carbon-containing alloy phase. The granular structure was more pronounced for the CoCrFeMnNi system. This microstructure was similar to other amorphous carbon-containing coatings based on transition metals [113,117]. These materials can be described as alloy/a-C composite materials and are expected to possess properties that are dependent on the individual traits of each phase. This was studied in Paper VII.

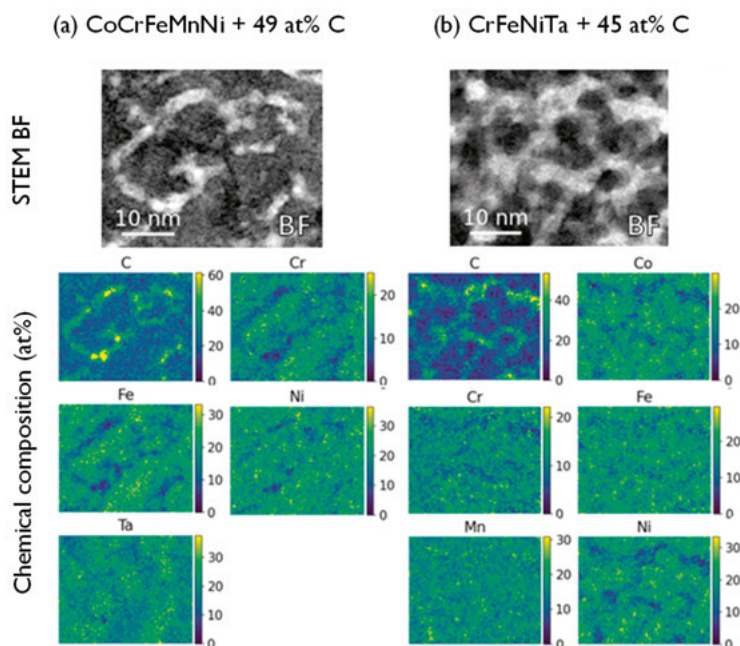


Figure 29. Top-view TEM studies of (a) CoCrFeMnNi with 49 at% C and (b) CrFeNiTa with 45 at% C showing the morphology with high-resolution TEM imaging (overview and a highly magnified image), the amorphous halos in the SAED, and elemental maps recorded with EDS. Adapted from Paper VII.

Chapter 7. Tuning the properties of multicomponent materials

7.1. Designing corrosion resistant alloys

In this section, principles of designing corrosion resistant alloys will be explored theoretically and experimentally. First, the well-studied principles for designing corrosion resistant binary alloys will be reviewed. Then, experiments will be used to study the use and limitations of these principles when applied to multicomponent alloy compositions.

7.1.1. Passivation of metals and alloys

Almost every metal is found in nature in its oxidized form, and so the process of extracting a metal from the ore involves reducing it to its metallic state. Once reduced, the metals react spontaneously with the oxygen in air and water and immediately begin the process of returning to their oxidized states. The reason why metals can be used as engineering materials is that in most cases, this process is extremely slow. This is because of a self-protective mechanism: a type of kinetic control called passivation.

Passivation is when corrosion products are formed on the surface of a metal, usually in the form of metal oxides or hydroxides, and serve as a barrier, lowering the oxidation rate of the metal [118]. The nature of this layer is characteristic of the combination of a metal and an environment, and not all combinations form sufficiently stable passive layers. In alloys, a single element with superior passivating abilities can protect the rest of the material. The most well-known example is stainless steel, where the more soluble iron oxide (rust) fails to protect the steel in many acidic environments. By adding enough Cr (what "enough" means in this context will be explained later) a Cr-rich oxide forms on the entire surface of the material when the Fe oxide is dissolved [39].

Even when the metal is passivated, the oxidation continues, although the rates are typically several orders of magnitude lower than for the unprotected surface. Passivation is a dynamic process that causes the suppression of the redox reaction by the separation of the metal from the electrolyte with a layer of metal oxide. Once passivated, the corrosion reactions reach a steady-state. The rate of corrosion then depends on the balance of reactions seen in Figure 30: the oxidation at the metal/oxide interphase, the dissolution at the

oxide/solution interphase, and the migration of metal and oxygen ions through the oxide layer [118].

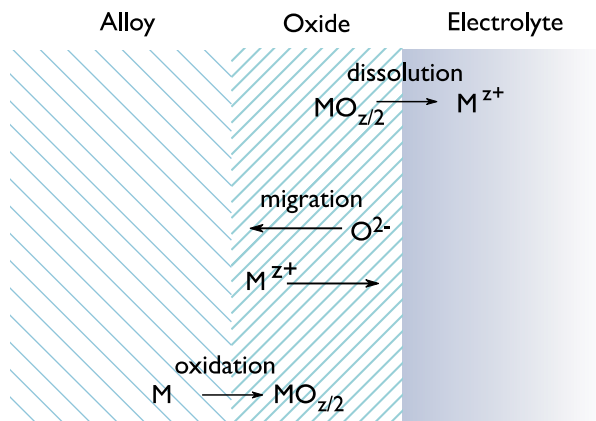


Figure 30. Processes that determine the corrosion rate of a passivated metal: the oxidation of the metal at the metal-oxide interphase, the migration of metal and oxygen ions through the oxide, and the dissolution of the oxide by the electrolyte. Observe that the oxidation and dissolution processes are not displayed as balanced chemical reactions, but only express the change in the predominant chemical species.

This balance of reactions is sensitive to changes in the alloy composition and microstructure, as well as in the environment. There are, therefore, many modifications that can be used to tune the resistance of alloys to specific environments and lower the corrosion rates of already-passive alloys. This type of subtler improvement is the topic of Section 7.3., which describes what happens when carbon was added to the alloys. In Section 7.1., however, the scientific question is more blunt; the only concern is whether the alloys can form a passive layer or not.

7.1.2. Using a percolation model to design passivating alloys

Stainless steels are some of the best-known examples of alloys where one alloying element is responsible for the passivation. In stainless steels, it is the less soluble Cr oxide that remains on the surface when the more soluble Fe oxide is dissolved. Stainless steel was discovered in 1911 when Philip Monnartz found that steels became resistant to acids if they contained at least 12 at% Cr [119]. This was an empirical finding, and it was only later that a theoretical framework was applied to understand the origin of this value.

In 1986, Sieradzki and Newman connected the critical value to the mathematical concept of percolation [120]. Percolation theory (developed by Broadbent and Hammarly in 1957 [121]) describes the connectivity in a lattice where the sites can be either open or closed. An open site can connect to its neighbors, a closed site is isolated from the network. Percolation theory in its

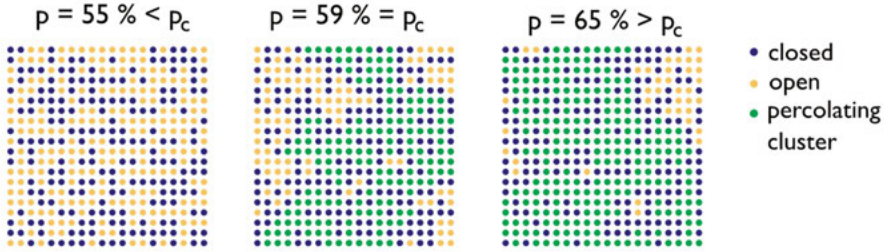
simplest form answers the following question: for a lattice with a random distribution of open and closed sites, what fraction of sites (p) need to be open for there to exist an interconnected network that spans the entire lattice? The answer is in the form of a probability. Below a certain fraction, the probability of finding such a network is zero; only smaller, disconnected clusters can form. Above a certain fraction, the probability is one. Between these extremes, there is a critical fraction or percentage, p_c , called the percolation threshold. p_c depends on the lattice in question. It also depends on whether the open sites can connect only to their nearest neighbors (1st NN) or if the connection extends to the 2nd or 3rd NN, etc [122].

This principle can easily be tested and visualized through a rudimentary Monte Carlo simulation starting in two dimensions. A simple cubic lattice was filled with a random distribution of closed and open sites (they were simply represented by ones or zeros in a 2D matrix). A script was then written in Matlab that searched for percolating clusters, given that each open site was allowed to connect only with its 1st NN. A percolating cluster was defined as a cluster that connected the top and bottom edges of the matrix. Three such experiments are displayed in the first row in Figure 31, showing one experiment below, one above, and one exactly at the percolation threshold p_c [122]. The dots represent the sites, the dark blue dots are closed sites, the yellow dots are open sites, and the green dots are sites belonging to the percolating cluster. At $p = 55\%$, there was nearly zero probability of clustering. At $p = 60\%$, small clusters formed in some of the experiments. At $p = 65\%$, large clusters formed in almost every experiment.

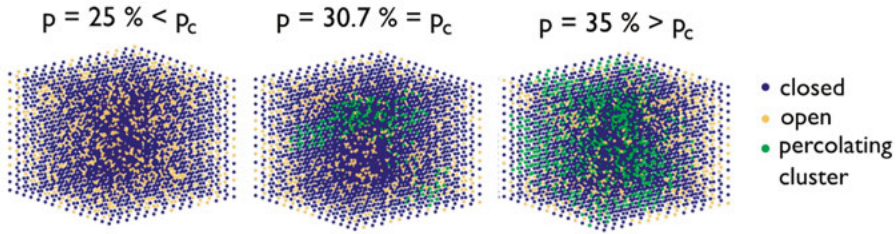
The same type of simulation was performed in three dimensions on a simple cubic lattice considering only 1st NN, and finally, a face-centered cubic (fcc) lattice with connectivity up to 2nd NN (more relevant to the experiments in this work). For the 3D lattices, percolation was defined as the existence of a cluster that reached the top and bottom surfaces of the matrix. The results of some of these experiments are also presented in Figure 31.

Repeated experiments were then performed for the three lattices for $p = 0 - 100\%$, using 0.1% steps and 100 randomly generated lattices for each step. Slightly larger lattices were used to achieve better statistics. Based on these experiments, the probability of finding a percolating cluster is presented as a function of p (Figure 31, bottom right). In this graph, the critical nature of percolation becomes apparent. Below p_c , which is found at the inflection point of each curve, the percolation probability quickly decreases to zero. Above p_c , it rises sharply. In these experiments, p_c was found to be 14, 30, and 60 %, for the fcc, simple cubic, and square lattice, respectively. These were close to the values given in ref [122], which were originally determined with similar Monte Carlo experiments [123].

square lattice - 1st NN connectivity
20 x 20 sites



simple cubic 1st NN connectivity
15 x 15 x 15 sites



face centered cubic
2nd NN connectivity
10 x 10 x 10 unit cells

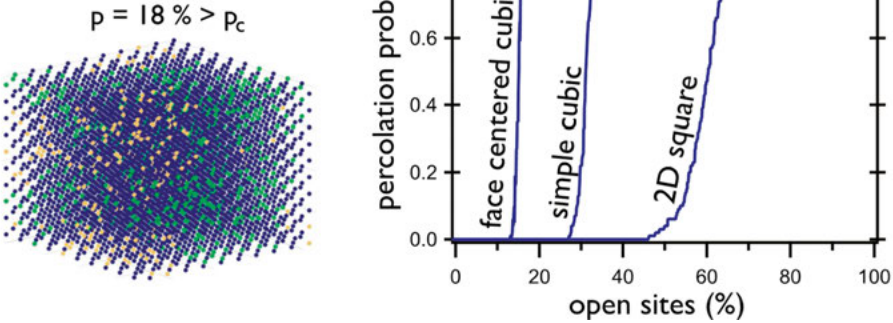


Figure 31. Percolation simulations performed on a square lattice, a simple cubic lattice, and a face centered cubic lattice. The size and connectivity are specified for each lattice. In the lower right corner is a percolation probability diagram which is the results of repeated percolation experiments with p from 0 to 1. Unpublished results.

When simulating the passivation process in an alloy, the lattice represents the crystal lattice, and the sites are the atoms. Open sites are usually defined as the atoms of the passivating element, e.g., Cr in stainless steel. The maximum separation between open sites is based on the simple assumption that two Cr atoms are connected if they are close enough to be bridged with a Cr-

O-Cr bond. This distance can be derived from ionic radii data [124]. For a random distribution of Cr in austenitic stainless steel, this means that Cr can bridge to their 1st and 2nd NN, but not to their 3rd. The passivation of austenitic steel is thus represented by the simulation of the fcc lattice in Figure 31. The calculated p_c of 14 % is an estimate of the minimum concentration of Cr needed to passivate the steel. This is because, above p_c , Cr can form a continuous oxide network that cannot be removed by dissolving the Fe (and Ni) that surrounds it.

Since the percolation model was first proposed, it has been refined to describe the corrosion process more realistically. p_c is only the minimum Cr concentration that is necessary to form a network. But for Cr oxide to cover the surface of an alloy with exactly 14 at% Cr, the non-passivating element (Fe, Ni, etc.) would have to dissolve to a depth of thousands of monolayers. Xie et al. [124] have, therefore, proposed to calculate a new passivation threshold that sets an upper limit for the number of dissolved atomic layers. The passivation threshold is then given by

$$[M]_{passivation} = p_c + (h/c)^{-1.139} \quad \text{Eq. 6}$$

where p_c is the percolation threshold expressed as a fraction, h is the number of layers, and c is a constant of order unity. The derivation of this relationship is described in detail in ref [125].

While the model has been successful in predicting the passivation thresholds of multiple alloys, it is obviously an extremely simplified description of the corrosion process. The diffusion of atoms both inside the alloy and on the surface is assumed to be non-existent, passivation by precipitation of corrosion products is not considered, and it offers no clue as to which elements can be passivating in the first place. Nevertheless, it is a necessary theoretical framework for understanding why the passivation thresholds vary for different alloys. It can also provide a background to why certain material characteristics, like elemental fluctuations or a high surface area, make it more difficult to achieve stable passivation.

The following method is therefore proposed to predict the passivating ability of a new alloy:

1. Use Pourbaix diagrams to find the range of pH and potential where an element exists as solid oxidation products at equilibrium
2. Use studies of the single element in the relevant electrolyte to find if the oxide in question has sufficient stability to be considered passive
3. Calculate the passivation threshold with percolation theory to find the minimum concentration of the passivating element(s) in the new alloy

7.1.3 Multicomponent alloys with a single passivating element

The first alloy studied in this work was the Cantor alloy, CoCrFeMnNi. In acidic environments and at potentials between -0.4 and 0.9 V vs Ag/AgCl, Cr is the only element that is expected to form a passive oxide [126]. Based on the proposed theory above, CoCrFeMnNi with an fcc lattice (ccp structure) should therefore have the same percolation threshold as austenitic stainless steel, around 14 at% Cr. An equimolar composition with 20 at% Cr would (according to Eq. 6) then limit the dissolution of the other metals to around 10 monolayers when the oxide is first formed, or when it repassivates after rupturing.

The corrosion behavior of bulk CoCrFeMnNi has been studied previously, and it is indeed comparable to austenitic stainless steel [40,127]. The same was found to be true for the CoCrFeMnNi coatings in this work. Figure 32 shows polarization curves of a CoCrFeMnNi alloy (deposited with no heating and -100 V bias), compared to a bulk sample of a hyper-duplex stainless steel. Both alloys formed a passive layer shortly after E_{corr} , although CoCrFeMnNi also displayed an active peak, meaning that the passivation process was slower for this sample. Both alloys then remained in a passivated state until reaching 0.9 V vs Ag/AgCl. This is the transpassive potential, where Cr oxidizes and forms soluble Cr(VI) species. This led to the rapid oxidation and dissolution of the previously passivated alloys. At potentials above 1.2 V, close to the end of the polarization curve, a weaker passivation was observed for the CoCrFeMnNi alloy. This was identified to be due to the formation of MnO_2 , which is only thermodynamically stable at these high potentials [126].

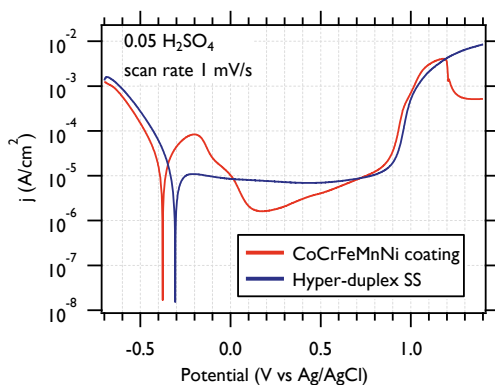


Figure 32. Polarization curve of a CoCrFeMnNi coating and a polished bulk piece of hyper-duplex stainless steel (SAF 3207HD, Sandvik AB). The data is adapted from Paper VI.

The compositions of the oxides on austenitic stainless steel are well-studied [39,128]. Steels are known to form a layered oxide structure based, among other factors, on the oxygen affinity of the alloying elements. The less-noble

Cr and Fe are more easily oxidized, while the nobler Ni is left behind, enriched in the alloy phase under the oxide. This principle has also been reported to apply to CoCrFeMnNi bulk alloy [129] and confirmed for the coatings in this study (in Paper V).

The more detailed aspects of the passivation mechanisms were studied in Paper V and Paper VI. This will be presented in later sections. In this part, the conclusion is simply that the basic principles of passivation for conventional alloys apply to the CoCrFeMnNi HEA.

7.1.4. Extending the passive region with a second passivating element

This section concerns the passivation of the CrFeNiTa and CrFeNiW systems from Paper III. The overhead aim was to find an alloy composition based on a 3d transition metal base alloy, which surpassed the corrosion resistance of stainless steels and the Cantor alloy by remaining passivated at potentials above 1 V vs Ag/AgCl. This was achieved by adding a single element from the refractory metal family to the equimolar CrFeNi alloy. The specific aim of Paper III was to understand if the choice of refractory metal influenced the ability to form a passive layer at high potentials.

The two selected refractory metals were Ta and W. They were first assessed according to the list of criteria defined in Section 7.1.2. To begin with, they both have thermodynamically stable oxides (Ta_2O_5 and WO_3 , respectively) at high potentials [126]. The pure elements are both known to dissolve relatively slowly in H_2SO_4 [130,131] and they are known to form passive layers in binary alloys [132,133]. The passivation thresholds were then estimated using equation 6. Since the alloys were amorphous (see Section 6.2.), a calculation using the real material structure would be complex. The task was simplified by using the fcc phase, based on the assumption that the alloys were nearly close-packed (the soundness of this assumption was assessed in Paper III). The calculations predicted that the passivation threshold should be the same for both alloy systems. The minimum value, given by the percolation threshold for fcc, was around 14 %. With a limitation of 10 dissolved atomic layers, the threshold value, $M_{\text{passivation}}$, increased to around 20 at%. It should be noted that this threshold value is valid when Ta or W is the only stable element. At potentials below 0.9 V, Cr is also passive, and the passivation should in principle be possible if the threshold value is lower than the sum of the concentrations of Cr and Ta or W.

A final factor relating to the chosen metals was considered: their electrochemical nobilities. W is nobler than Fe, Cr, and Ni, while Ta is less noble than all the included metals [134]. This should give rise to a layering of elements at the surface, similar to the effect seen in stainless steel or CoCrFeMnNi, where the more noble element Ni was not present in the oxide

layer to a high extent [39,128]. In the present case, this should mean that, when oxidized freely in the electrolyte or at low potentials, the Ta should be preferentially oxidized but the W should be less oxidized. This would lead to a lower concentration of W in the initially formed oxide. It was hypothesized that the lower W concentration would make it more difficult to suppress the dissolution of Cr above 0.9 V. It was, however, not certain whether this would affect the ability to finally achieve passivation.

Figure 33 (b) and (c) display the main results of this study. The base alloy, which is the red curve in both (a) and (b), exhibited a similar corrosion behavior as that seen for the stainless steel, or the Cantor alloy, in Figure 32. At 1.5 V vs Ag/AgCl, the current decreased. This was not due to repassivation, but a result of the complete dissolution of the coating and exposure of the SiO₂ substrate. Meanwhile, the pure Ta and W coatings (light blue and dark brown, respectively) stayed passivated until the end of the polarization curve experiment.

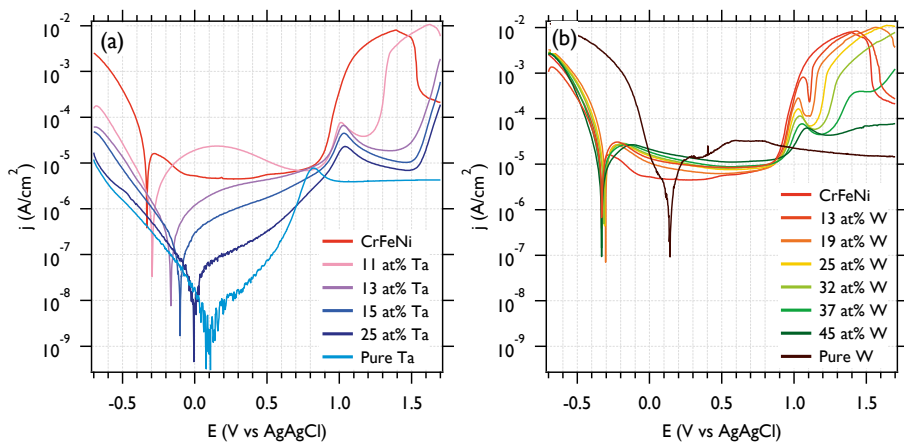


Figure 33. Polarization curves of (a) the equimolar CrFeNi base alloy and for pure W and Ta coatings (b) the alloys in the CrFeNiTa system and (c) the alloys in the CrFeNiW systems, including the CrFeNi base alloy, pure Ta and pure W as references. The figure is adapted from Paper III.

The rest of the curves are measurements on alloys with different concentrations of Ta or W, respectively. Contrary to the prediction, the two alloy systems were not found to passivate at the same refractory metal concentration. The coatings with Ta remained passive at high potentials for concentrations of 15 at% and above. Meanwhile, 45 at% W was required to passivate the CrFeNiW alloys. All the other coatings with concentrations of Ta or W below these experimental threshold values showed signs of failure and dissolved after an extended time at high potentials.

Post-corrosion surface studies with SEM, EDS, XPS, and AFM and mass spectrometry of the electrolyte were used to investigate the mechanisms

behind this large difference. It was found that the coatings that dissolved despite being above the predicted threshold values of W, did not dissolve congruently. Instead of just an exposed substrate at the end of the curve, there was a W-rich oxide on the surface. Cr and Ni were completely dissolved, and the Fe was partly dissolved, leading to the conclusion that the observed oxide was nanoporous. This means that the assumption that the W was above the percolation threshold must have been correct since there was a connectivity of W throughout the alloy that allowed it to form a continuous W-oxide and not be removed when the remaining elements dissolved around it (i.e. undercutting). However, the oxide that formed was not passivating; it was porous and non-protective. Only the sample with 45 at% W in the bulk was able to stabilize the current and avoid dissolution.

The reason why W failed to passivate was further investigated and two factors were found that were likely contributors to this behavior. The first was the lower concentration of W than Ta in the initial oxide, i.e., the oxide that was formed at the beginning of the polarization curve. On the Ta-containing alloys, the Ta was enriched in the oxide, and particularly close to the top surface of the sample. The W in the oxide, on the other hand, was found closer to the bulk of the alloy. This means that, for the same bulk concentration of Ta and W, more of the initially formed oxide had to dissolve on the W-containing samples, which is supported by the height of the peaks at 1 V in the polarization curves. This process increased the roughness and porosity and may have led to irreversible damage that made it more difficult to reach passivation by a new oxide.

The second factor was the pH sensitivity of the W oxides. The development of porosity can lead to the formation of concentration gradients through a build-up of corrosion products in the pores. During the anodic dissolution of metals, this should include a locally decreased pH. The dissolution of WO_3 is sensitive to the local pH and the initial porosity could, therefore, have led to a locally increased dissolution of W. This could prevent it from forming a passivating oxide and thus allow for the continued development of porosity.

In Figure 34, the proposed processes for the CrFeNiW coatings are illustrated. Case A is valid when W is found below its percolation threshold. Case B is valid when the percolation threshold is surpassed, but the W concentration in the oxide is too low to achieve a stable passivation. Case C is when the W can passivate the alloy.

7.1.5. Summarizing comments on passivation in MCAs

In the studies of the passivation of MCAs (Paper III and Paper VI), it was found that multicomponent alloys follow the same basic principles for forming passivating oxides as conventional alloys. For MCAs with only one passivating element, the criteria formulated for binary alloys can easily be applied. However, in MCAs with more than one passivating element, the

complexity of the alloys means that additional factors have to be taken into consideration.

It was found that the percolation theory could be applied successfully to predict the percolation threshold of an element, meaning the concentration where this element forms a continuous network through the alloy. However, the connectivity did not necessarily lead to passivation. This was due to the development of surface roughness and porosity.

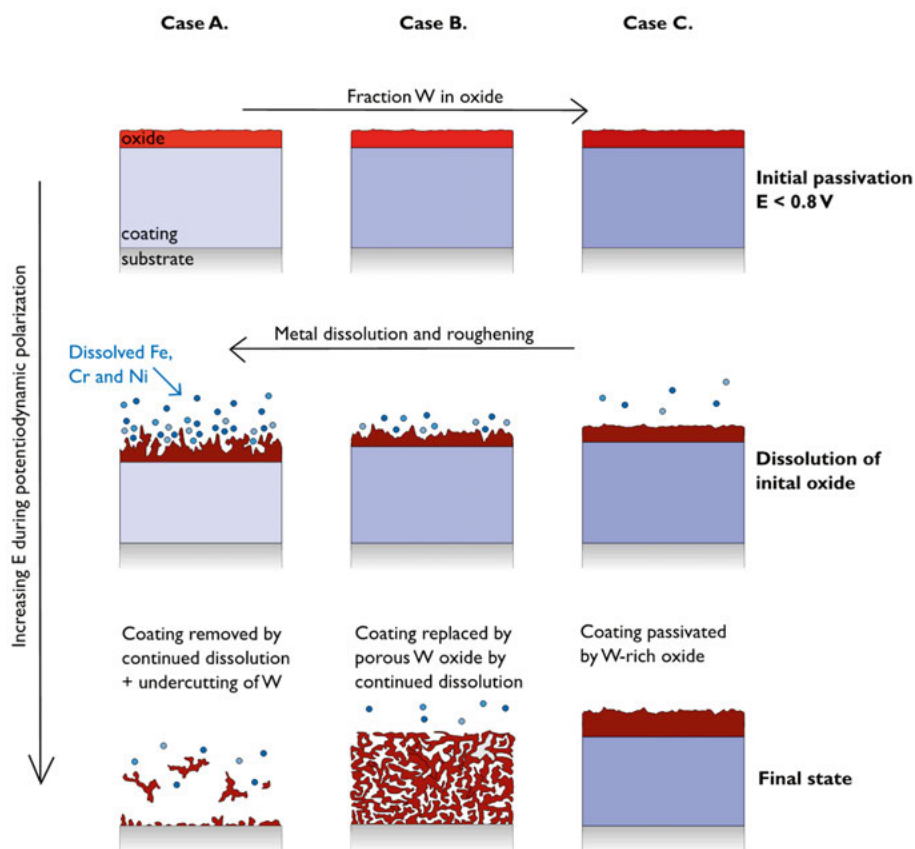


Figure 34. Schematic image of the corrosion process at high potentials for coatings in the CrFeNiW alloy system. Case A is valid below the percolation threshold of W, and Case B and C are valid when W is above the percolation threshold. The figure is from Paper III.

One important conclusion from this observation is that the ability to form a passive layer depends strongly on the damage that has already been caused on the surface prior to the passivation step. In the specific procedure studied in Paper III, the damage could be minimized if the second passivating element (Ta or W) was present in the initially formed oxide to a higher degree. This is more likely if the chosen refractory metal is equally or less noble than Cr. This can be applied as a more general design principle for multicomponent alloys:

the passivating elements should have similar nobility so that they can both incorporate into the initially formed alloy.

A final question is why the use of MCAs with refractory metals would be preferable to the use of pure refractory metal elements. There could be many reasons: the 3d metal alloys are generally cheaper, lighter, more ductile, and more widely available. In Paper III, the contact resistance of the alloys was determined before and after corrosion and it was found that the alloys with low concentrations of Ta had a much lower resistance than pure Ta. This would make them more suitable for use in electrochemical devices where the cell resistance must be minimized.

7.2. The corrosion in bulk samples and coatings

When comparing sputtered materials to similar bulk samples, it is important to consider how the synthesis methods affect the properties. In Figure 35, polarization curves recorded for an equimolar bulk CoCrFeMnNi sample synthesized by arc melting are compared to that for a magnetron sputtered sample deposited without heating with -100 V bias voltage. Two different electrolytes were used: 0.05 M H₂SO₄, which gives rise to more general corrosion, and 0.05 M HCl, which promotes pitting corrosion. The corrosion resistance of the coatings was higher in both electrolytes, as seen by the passive currents. The difference was about one order of magnitude in the H₂SO₄ solution and up to three orders of magnitude in the HCl solution. The corrosion process of the two coatings was very similar in both electrolytes. The coatings thus appear to be much less susceptible to pitting compared to the bulk samples.

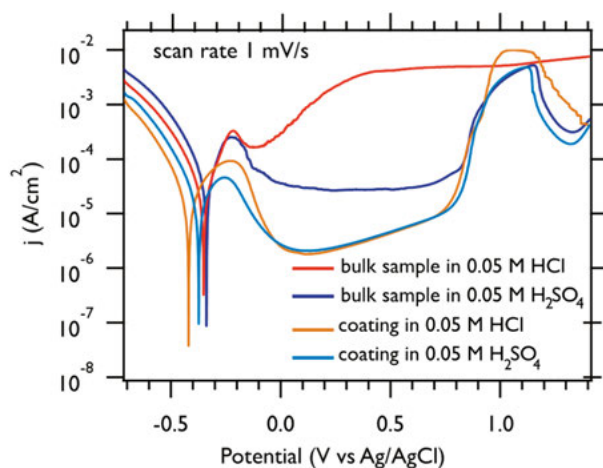


Figure 35. Polarization curves recorded for a magnetron sputtered CoCrFeMnNi coating sample deposited without heating and with -100 V substrate bias and an equimolar CoCrFeMnNi bulk sample synthesized with arc-melting. The coating measurements are from Paper VI, while the bulk measurements are unpublished.

This difference could be attributed to the elemental distributions in the samples. Figure 36 shows EDX maps of the bulk sample performed with top-view SEM. Mn and Ni had segregated to the grain boundaries, resulting in the relative depletion of Cr in these regions, which were in the micrometer scale. Since Cr is the main passivating element, the grain boundaries should be more susceptible to corrosion.

In the coatings, as shown by the TEM-EDX maps in Figure 10, the elements were much more homogeneously distributed, as a consequence of the kinetically controlled growth. While some very slight segregation of Mn to the grain column boundaries could be observed at higher magnifications, it is not certain that segregation at this scale would have any effects on the ability to form a continuous passive layer.

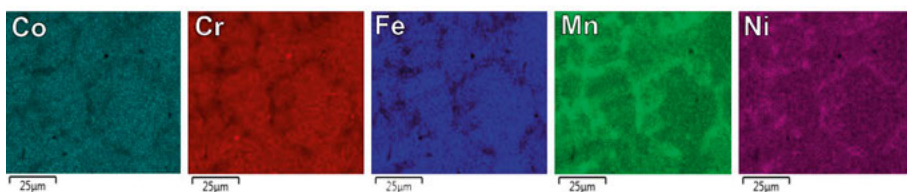


Figure 36. Elemental distribution map for a bulk CoCrFeMnNi sample synthesized with arc melting. The maps were acquired with EDX in SEM. Unpublished data.

Another difference between the two types of samples, which could affect the corrosion resistance, is the smaller grain size in the coating. Just as the density of grain boundaries could affect the diffusion kinetics and nucleation during growth, it could also influence the migration kinetics and oxide nucleation during corrosion. Exactly how the grain boundaries influence the corrosion process, and whether there are general principles that are valid for many materials systems, are questions that are under discussion within the corrosion community [135,136].

7.3 Corrosion of alloys modified with carbon

In Section 6.3.2., the effect of carbon on the phase formation in MCAs was described for two systems: CoCrFeMnNi(C) and CrFeNiTa(C). It was found that the addition of carbon formed materials in two different regimes. At lower concentrations, amorphous single-phase carbon-containing alloys were formed. At higher contents, the carbon partly segregated to a separate phase, creating a nanocomposite MCA/amorphous carbon (a-C) material. In the following sections, the effect of carbon on the corrosion resistance will be explored for the two regimes.

7.3.1. The effect of carbon in the amorphous regime

The most significant results of the corrosion tests are shown in Figure 37 (a) and (b), featuring two representative polarization curves recorded using slightly different measurement parameters. In both cases, the films were first placed in the test cell for 40 minutes at the OCP to corrode freely in the electrolyte. For the polarization curves in (a) the cathodic region was shorter, only from 0.3 V below the OCP, while the curves in (b) started at -0.7 V vs Ag/AgCl. The scan rates were also different: 5 mV/s for the curves in (a) and 1 mV/s for the curves in (b). The main consequence of these differences appears to be that a slower scan and longer cathodic region in the (b) case allowed the oxides to, at least partially, undergo reduction at the beginning of the scan. The subsequent oxidation in (b) therefore involved a re-formation of the passive layer, while curve (a) mainly depicts the performance of the already-formed passive layer.

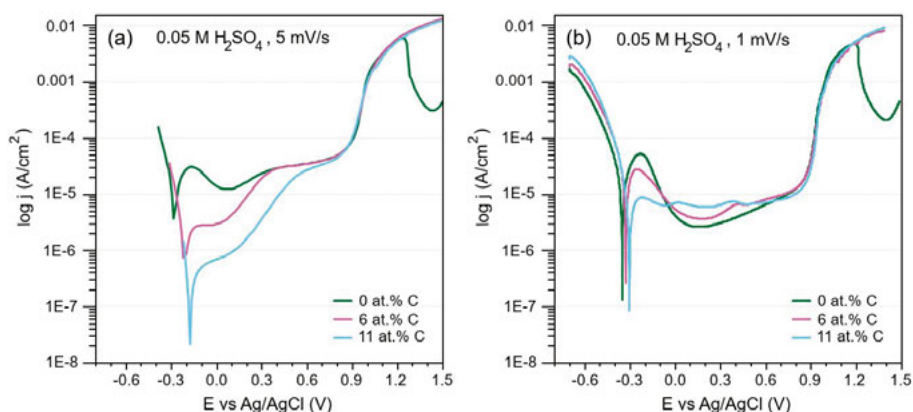


Figure 37. Polarization curves of the films with 0, 6, and 11 at.% C, performed in 0.05 H_2SO_4 after 40 minutes under OCP conditions. The measurements in (a) and (b) were performed using different scan rates and start potentials. Figure (a) is from Paper V and Figure (b) is adapted from Paper VI.

In both experiments, trends that depend on the carbon content could be observed. In curve (a), both the corrosion current, j_{corr} , and the currents in the early part of the passive region were lower for higher carbon contents. This indicates that the passivated samples were more corrosion resistant when carbon was present. The curves in (b) provide complementary information. Since the passive layers were (at least partially) reduced at the beginning of the polarization measurement, the layers must have reformed by an initial rapid oxidation, during which the passivating element was enriched in the oxide while the other elements are dissolved. The current then decreased when a Cr-rich oxide covers the surface. This process is evident in all three samples in Figure 37 (b). The main trend in the measurements concerns the magnitude of the initial current peak; the oxidation process appears to be slower in the carbon-

containing samples. This suppression of the current points to a limitation of the corrosion rate. The same limitation could explain the lower currents in the already-passivated carbon-containing coatings, seen in Figure 37 (a).

At higher potentials, around 1 V vs Ag/AgCl, all three coatings exhibited a transpassive behavior, when the Cr(III) in the passive layer was oxidized to soluble Cr(VI) species, as in stainless steel.

The passive layers formed on the coatings after 40 min at OCP conditions were studied using X-ray photoelectron spectroscopy, to better understand the state of the samples at the beginning of the polarization curve in Figure 37 (a). The samples were exposed to air for a few days after the period at OCP, so some change in the oxide was expected as the oxidation process continued. However, there were clear differences in the thickness and composition of the oxides formed under OCP conditions and those of the samples that had only been exposed to air after the deposition. This suggests that the oxide formed in the electrolyte was relatively stable in air.

3p core-level XPS peaks of the five metals, recorded at the surface and in the bulk of the films after sputter etching, are shown in Figure 38 (a). The peak fitting for two of the measurements is presented in (c) and (d), and a compilation of the relative intensities of the fitted peaks is shown in (b). The results were very similar for the films with 0 and 6 at.% C. After 40 minutes at the OCP, Cr was enriched at the surface in its oxidized form. Mn, Fe and Co were partly oxidized, and Ni was purely metallic, meaning that the signal was coming from the alloy beneath the oxide. The similarity between the samples indicates that the carbon did not dramatically change the oxidation mechanisms of the metals. This supports the results from the polarization curves; the oxidation process was similar, but the rate was suppressed by the added carbon.

The location of the carbon was also explored with XPS. At the surface of the samples after the OCP period, only a thin layer of hydrocarbon contamination was observed. As seen in Figure 39 (a), this contribution to the peak was removed after 1 minute of sputter etching. The carbon in the material appears to be located mainly below the passive layer since the signal increases with increasing sputter time. It was tentatively proposed in Paper V that the carbon was enriched underneath the passive layer and that this carbon-enriched layer would act as a barrier for the diffusion of the metallic elements to the metal-oxide interphase, thus yielding a decreased corrosion rate. However, more recent XPS studies did not reveal any such carbon enrichment. In a sputter depth profile of the passive layer performed with a low analysis angle (Figure 39 (a)) the C-Me peak simply increases until reaching the bulk level, which is achieved after the same sputtering time as seen for the oxygen signal in Figure 39 (b).

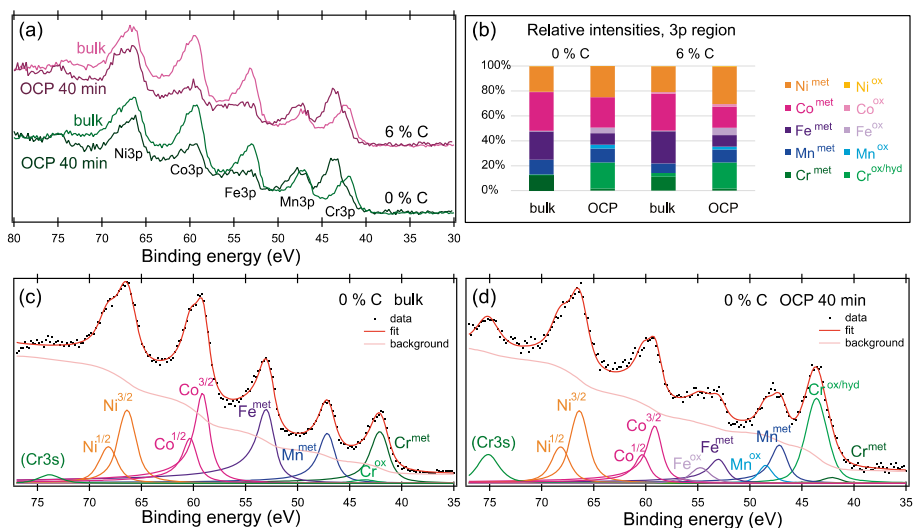


Figure 38. (a) Core level peaks of the metal 3p regions of all the metallic elements in two samples after 40 min at OCP, performed before and after sputter-etching. (b) Relative peak intensities of the metallic elements separated into metallic and oxide contributions. (c)-(d) Fitted peaks for two selected spectra. The measurements were performed with an analysis angle of 45° . The Figure is from Paper V.

The current hypothesis is that the carbon slows down the diffusion of metals below the passive layer, but not necessarily through an enrichment at this depth. One explanation could be that the added carbon atoms increase the energy of diffusion of metallic elements in the amorphous matrix. Another possibility is that there is a small difference in the domain size of the materials, which barely would be detectable using diffraction.

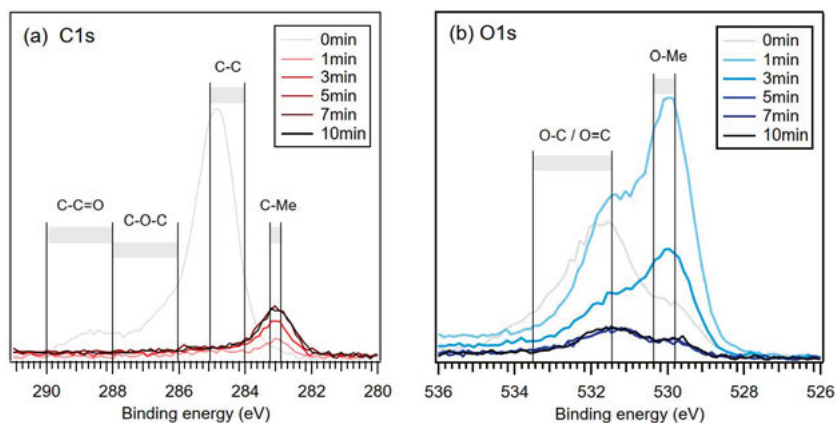


Figure 39. XPS sputter depth profiles on a sample with 6 at.% C after 40 min at the OCP. (a) C1s core level peaks, including the ranges for literature reference values [58,113,116] (b) O1s core level peak, including literature reference values [137,138] The different curves correspond to the sputter times. The measurements were performed with an analysis angle of 10° . The Figure is adapted from Paper VI.

7.3.2. The effect of carbon in composite coatings

The study above showed that, in the low-carbon regime, the carbon was fully incorporated into the alloy. It was found that when a passive layer had formed, the carbon was not in contact with the solution, but was only present in the bulk alloy. When higher concentrations of carbon were added, a separate free carbon phase was formed. This means that, in this regime, carbon must be in direct contact with the solution. The effect of this change was briefly studied for the CoCrFeMnNi/a-C and CrFeNiTa/a-C nanocomposites coatings, to ensure that the free carbon did not degrade the corrosion resistance. It was reported in a study on amorphous magnetron sputtered Cr-C, that the presence of free carbon increased the current during a polarization curve [139]. However, the carbon did not dissolve to form the thermodynamically stable CO_2 . Instead, it formed oxidized surface groups, which can be viewed as a kind of passivation. It was, therefore, suggested that, once the oxidized layer is formed, the carbon would be beneficial to the corrosion resistance [139].

This principle was tested in the present study through the repeated recording of polarization curves for the coatings in the two alloy systems by comparing the performance of the coatings in the amorphous regime to that of coatings with free carbon. The results, which are displayed in Figure 40, showed that, contrary to the results in ref [139], the free carbon did not result in higher currents during the first sweep. The corrosion potential was more positive for the composite coatings while the passive currents were similar for both regimes. When the potential sweep was repeated a second and third time, the differences between the amorphous and composite coatings were even smaller. We can thus conclude that in this electrolyte, the presence of carbon has only a limited effect on the corrosion rate.

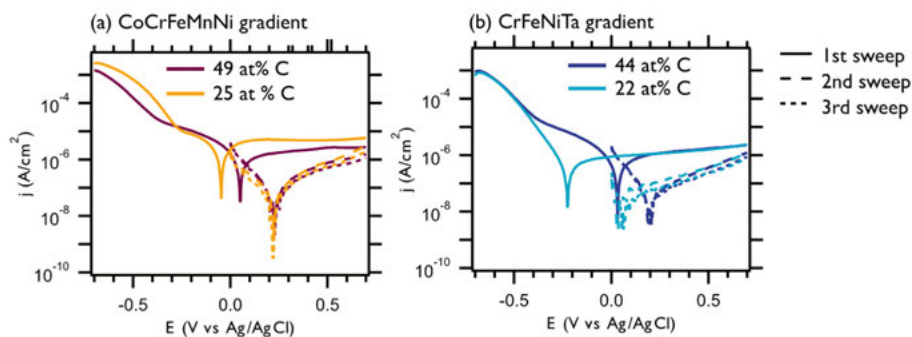


Figure 40. Electrochemical studies on coatings of CoCrFeMnNi and CrFeNiTa with added carbon in the amorphous regime and with the presence of free carbon. The experiments were performed in 0.05 M H_2SO_4 with a sweep rate of 1 mV/s. The figure is from Paper VII.

7.4. Tuning the mechanical properties

The mechanical properties of a material depend on the characteristics of a material at different scales, from the bonds between atoms to the crystal structure, to larger features such as grain size, grain shape, defect concentration, segregation, etc. In this thesis, crystalline alloys, amorphous alloys, and composites are studied, which each have different principles for their mechanical response. For crystalline materials, the mechanisms behind plastic deformation are well-studied and understood, while the equivalent principles in amorphous metals are less well-explored. Crystals deform plastically through the movement of dislocations, which are crystallographic defects. Amorphous materials have no long-range order, and therefore, no dislocations. The deformation is, therefore, often concentrated into bands of atoms, known as shear bands [140]. Amorphous alloys are often harder than crystalline alloys, and typically more brittle, but these properties can vary greatly with the composition and morphology. Since the area of research is relatively new, there is less theory on how to tune the mechanical properties by controlling the formation and movement of shear bands. Composite materials have properties that depend on each phase in the material, but they also depend on the size of the phases and the interface between them [141].

7.4.1. The unusually high hardness of magnetron sputtered coatings

Just as the corrosion resistance, there are mechanical properties that are highly dependent on the synthesis route of a material. It is, for example, well-known that magnetron sputtered coatings can have very different hardness than the corresponding bulk material.

This can be partly explained by the nanocrystallinity of the coating. The hardness values of the Cantor alloy from the literature were compiled by Xiao et al. [106] and plotted against the Hall-Petch equation, which relates the hardness of a material to its average grain size. The figure from ref [106] is included below (Figure 41). It can be seen that typical bulk alloys have reported values of around 3 GPa, while nanocrystalline materials are considerably harder.

In Paper I, hardness measurements were performed by nanoindentation on carbon-free Cantor alloy coatings deposited without heating and with varying substrate bias. The hardest material in the present study had an average column size of 11 nm, meaning that the value of 12.2 GPa in Paper I exceeded the predicted Hall-Petch relationship by about 30%. This means that the high hardness cannot be only due to the smaller grain size. Another contributing factor is the high compressive stress in the coating. This is another feature that is typical of magnetron sputtered materials.

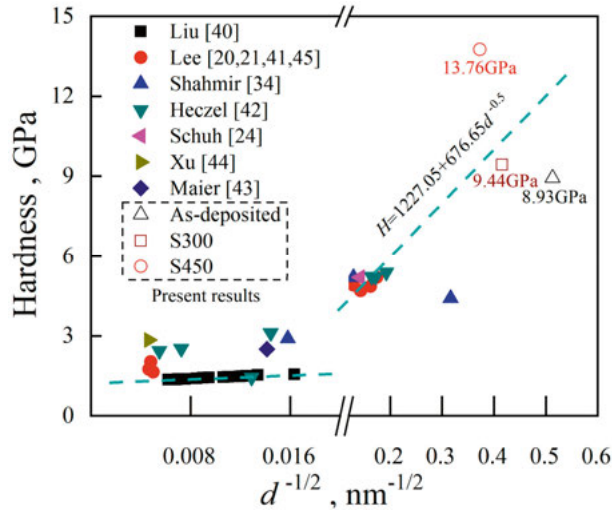


Figure 41. Compilation of hardness values reported for the Cantor alloy as a function of $d^{-1/2}$ where d is the average grain size. The dashed blue line is the Hall-Petch relationship for the Cantor alloy. The figure is from ref [106]. The hollow markers are experimental data from ref [106] while the filled markers are values from other references. Reprinted under the CC BY NC ND license.

7.4.2. The effect of carbon addition on the mechanical properties

Carbon was added to two multicomponent alloys (CoCrFeMnNi and CrFeNiTa) to improve their mechanical properties. This section presents the mechanical tests on alloys with added carbon in the two regimes described in Section 6.3.2: single-phase amorphous and alloy/amorphous carbon (a-C) composites. The purpose was to observe if the coatings with carbon were harder and more crack resistant. This section is separated into two sections, one for the single-phase amorphous and one for the nanocomposite regime, respectively.

The effect of carbon in the single-phase amorphous regime

Coatings in the CoCrFeMnNi(C) system with 0, 6, and 11 at% C were tested with multiple methods. The hardness was determined by nanoindentation to 10% of the film thickness, using a Berkovich diamond tip. The hardness of the coatings was calculated to be 7.9, 14.1, and 15.9 GPa, respectively, for the films with 0, 6, and 11 % carbon. The same instrument was used to perform indentations to a depth of 1250 nm, more than twice the film thickness, using the maximum load of the instrument and a cube-corner diamond tip to achieve a high strain at this load. The indents for the samples with 0 and 6 at.% C is shown in Figure 42 (a) and (b). Both films appeared to be ductile and deform without any cracking, forming pile-ups of material at the edges of the indents. The pileups of the sample with 6 at.% C had a jagged shape. This is typical for indents in amorphous materials, where the plastic deformation occurs as

discrete events with the activation shear bands [140]. While some knowledge was gained on the deformation mechanisms of the two materials, the method was not suitable for comparing the crack resistance of these ductile coatings.

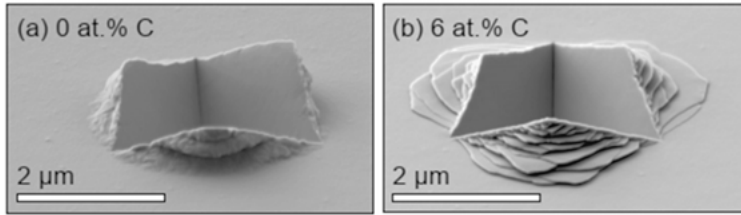


Figure 42. SEM micrographs of indents performed with a cube corner diamond tip, to 1250 nm depth. The images were acquired while tilting the samples relative to the electron beam. The figures are adapted from Paper V.

To better compare the materials, tensile testing was performed. Figure 43 (a) shows representative SEM micrographs acquired in situ during the tensile tests of the coatings on polymer substrates. Cracks formed in the films perpendicular to the direction of the strain. The number of cracks per unit area increased with the strain and was higher for the carbon-free coating. In Figure 43 (b), the crack density is plotted as a function of the tensile strain

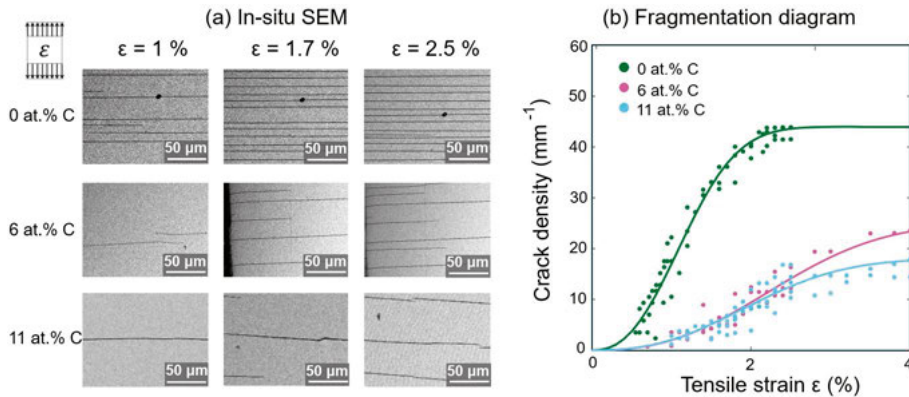


Figure 43. (a) SEM micrographs of CoCrFeMnNi with and without carbon during tensile tests on polyimide substrates and (b) crack density as a function of strain for the three different compositions. The figures are adapted from Paper V.

To quantify the strength of the coatings during cracking, the fragmentation data were fitted to the Weibull distribution function for the probability of failure of the coating, seen in Equation 1. The scale parameter σ_∞ , a measure of the strength of the coating, increased from 2.0 GPa for the sample with no carbon to 3.8 and 3.9 GPa for the samples with 6 and 11 at.% C, respectively. The shape parameter p , which is inversely proportional to the scatter in the coating strength, was lower for the carbon-containing samples, meaning that

these samples cracked in a less homogenous manner. The crack onset strain was also recorded for each experiment, but no significant differences in the values were found. However, the carbon-containing films had a significantly higher variance ($\alpha=0.05$) demonstrating once more the heterogeneous behavior of the amorphous coatings.

The carbon was thus seen to improve both the hardness and the crack resistance of the CoCrFeMnNi coatings. The fact that the largest increase in both hardness and crack resistance was between the carbon-free film and the two carbon-containing films indicates that these values are related to the shift from a crystalline to an amorphous state. The mechanisms for plastic deformation are entirely different in crystalline and amorphous alloys and it is difficult to compare the two materials. More in-depth studies with a larger sample set are needed to explain the relatively high crack resistance of the amorphous films and to investigate whether the addition of carbon favors the already amorphous alloys.

The effect of carbon in the nanocomposite regime

As described in section 6.3.2., a higher content leads to the formation of an amorphous alloy/carbon nanocomposite coating. Figure 44(a) displays the hardness and elastic modulus as a function of the fraction of carbon in the a-C phase, for three samples from each of the two alloy systems CoCrFeMnNi(C) and CrFeNiTa(C). The first point for each series is found at no free carbon, meaning that it is in the amorphous single-phase regime. In this regime, the CrFeNiTa(C) had a hardness of 13 GPa and was harder than the CoCrFeMnNi(C) coating which had a hardness of 11 GPa. With higher a-C contents, both HIT and Er decreased. The coatings with the highest amount of free carbon had similar hardness values in both materials systems: around 9 GPa.

The same instrument was used to perform deeper indentations, to a depth of around 1200 nm, using the maximum load of the instrument. The two single-phase alloys both deformed through shear banding, but the pileups were smaller and smoother in the CrFeNiTa samples. The two composite coatings deformed smoothly with no cracks or pileups and looked almost identical to each other. It appears that the presence of carbon was more important for the deformation mechanism than the composition of the base alloy. A similar trend was observed during tensile tests. The transition from single-phase amorphous to composite material led to an increase in crack density and the strength of the coatings was lower.

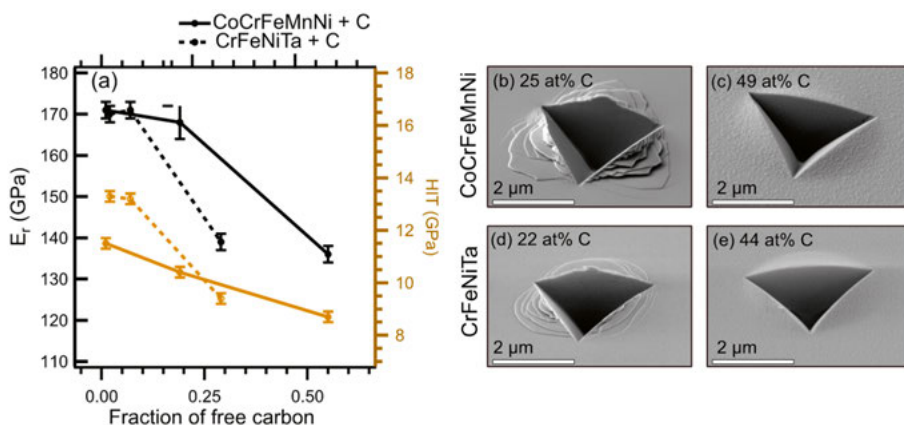


Figure 44. (a) Indentation hardness and elastic modulus as a function of the fraction of free carbon. The markers are the experimental data, the error bars show one standard deviation (from at least 15 indentations) and the lines are guides for the eye. (b)-(e) SEM micrographs of indents performed with a cube corner diamond tip, to approximately 1200 nm depth. The images were acquired while tilting the samples 59° relative to the electron beam. The figures are adapted from Paper VII.

In the literature, there are examples of metal/a-C nanocomposite coatings that are both harder and tougher than the single-phase materials. In the present case, this was not achieved. This could be because the metallic phase was less carbidic and more metallic and, therefore, softer compared to, for example, Ti-C/a-C nanocomposites [142]. Another example from the literature where a-C phase increased the hardness was a nanocomposite based on 316L stainless steel [113]. This material should be less carbidic, as in our case. However, in ref [113], the addition of carbon led to the formation of a uniform nanotubular structure, like nanofibers parallel to the growth direction. This microstructure may be responsible for the high hardness. The present case is more similar to an example of Cr-C/a-C nanocomposite coatings [117], which had a similar particle size and distribution of carbon and also reported a softening associated with the formation of the a-C phase. This shows that the achieved mechanical properties do not only depend on the amount of each phase or the chemical bonds within but also on the size and shape of the two phases. This is in line with current knowledge about nanocomposite materials [141].

7.4.3. Decreased plasticity in annealed amorphous alloys

The mechanisms of deformation in amorphous alloys are still largely unexplored. This is in part because the field is relatively new compared to the study of crystalline alloys. Another reason is that the lack of long-range order in amorphous alloys makes them more challenging to characterize. However, there have been many reported examples of how small structural or elemental

changes in the nanometer scale lead to dramatically improved properties. [140].

To gain more knowledge on the deformation mechanisms of the amorphous alloys in this work, one of the alloys from Paper III was subjected to mechanical tests before and after annealing. It was the equimolar CrFeNiTa. The aim of the study was to understand how the mechanical properties changed after annealing but before crystallization and relate the properties to nanoscale changes. All the results in this section are unpublished.

After preliminary annealing experiments, it was found that CrFeNiTa began forming nanocrystallites at around 650°C (the first phase to form was a C14 Laves phase). The alloy was therefore annealed in steps starting from 300 °C to final temperatures of 450, 550, and 650°C, spending 10 minutes at each temperature.

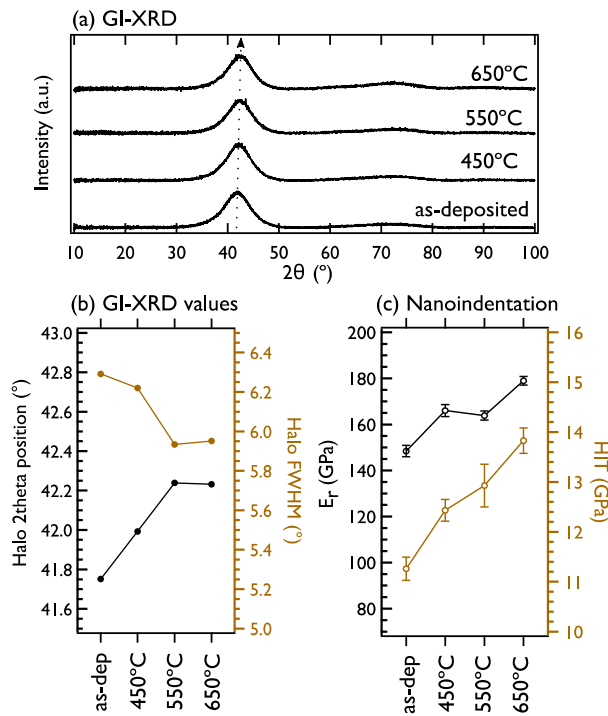


Figure 45. (a) Grazing incidence X-ray diffractograms of the CrFeNiTa coatings before and after annealing to 450, 550, and 650°C, (b) extracted data from the diffractograms, and (c) mechanical properties calculated from nanoindentation. The error bars are 95% confidence intervals. Unpublished data.

The diffractograms from GI-XRD measurements and extracted data from the same are found in Figure 45(a) and (b), respectively. At a first glance, the four samples appeared to exhibit identical amorphous halos. However, the position of the halo shifted to higher 2θ values and the width of the halo decreased during annealing to temperatures of up to 550°C. This means that the

average atomic distances in the amorphous alloys became smaller and more uniform. This is a sign of densification of the alloy, i.e. a decrease in the free volume. The mechanical properties of alloys are related to the free volume. Studies have shown that denser alloys are typically harder but more brittle [143,144].

The mechanical properties were first studied by nanoindentation (using a Berkovich tip and 50 nm deep indents). The hardness of the alloys increased progressively during annealing from 11.3 to 13.8 GPa, as shown in Figure 45(c). The elastic modulus also increased, from 148 to 179 GPa, but the trend was less clear. The changes from the as-deposited state to the sample annealed to 550°C can be attributed to the densification. The increase in hardness from 550 to 650°C cannot be attributed to densification since the average atomic distances were the same. A possible explanation could instead be the formation of nanocrystallites.

The deformation and fracture were then studied qualitatively. The first clear change between the as-deposited and annealed alloys was observed in the fracture surfaces of the coatings. Cross-section samples were prepared by cracking the oxidized Si substrates cleanly along the [001] direction. The SEM cross-section micrographs Figure 46(a) of the fracture in the as-deposited sample looked completely smooth (apart from a small piece of the coating that was chipped off). The annealed samples, however, displayed nanoscale vein patterns. These are often observed in metallic glasses, and the density of veins has been related to the fracture toughness; more closely spaced veins are typically a sign of a more brittle material in both bulk metallic glasses and amorphous coatings [145,146]. The fracture surface of the samples annealed to 650 °C had a more granular appearance which could be a sign of the formation of nanocrystallites.

Deeper indents, to a depth of 1 μm , were then performed with a cube corner tip, to study the deformation in a more controlled manner. The micrographs are shown in Figure 46(b). The sample annealed to 650°C had radial cracks initiating at the corners of the indent. This could be due to the formation of nanocrystallites, although this was not confirmed with TEM. The remaining samples were deformed without visible cracking, but with the formation of pileups around the indents. All the pileups consisted of bands, which is a sign of heterogenous flow through the formation of shear bands [147]. The as-deposited samples appeared to have a smaller number of bands, and they were smoother than in the annealed samples.

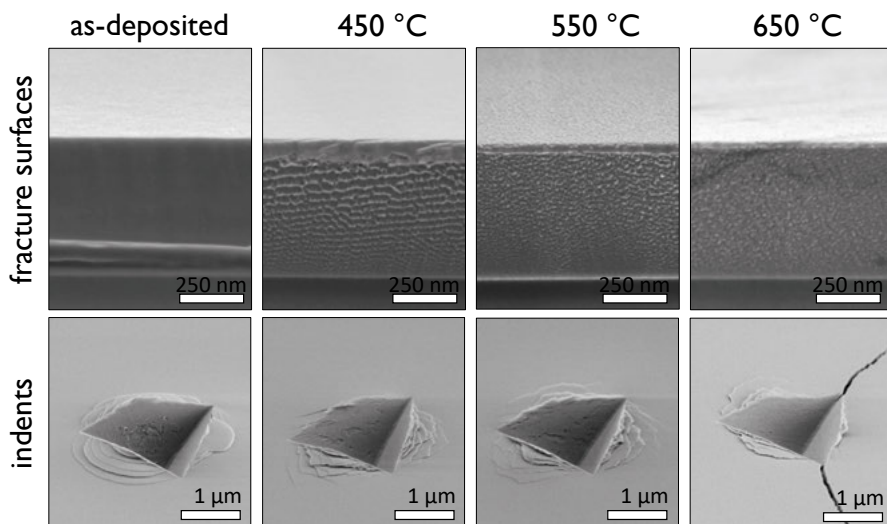


Figure 46. SEM micrographs of the fracture surface and indents performed with a cube corner tip to a depth of 1 μm . The indentation was load controlled and used a loading and unloading rate of 10 mN/min. Unpublished data.

The indents were finally studied in cross-section TEM (except for the sample annealed to 650°C), as shown in Figure 47. The bands that were seen from the top-view are clearly visible in the cross-section. It was confirmed that the morphology of the deformed area was smoother in the as-deposited samples and more jagged in the annealed coatings. Each band in the pileup should correspond to a shear event during indentation. The shear bands in the material were almost imperceptible except when using very high contrasts (they are marked with black arrows). This means that the shear did not result in fracture in most cases. However, in the coating annealed to 550°C, some shear bands penetrated deeper into the material and one of the shear bands had started developing into a crack.

This study concludes that the as-deposited samples appear to have the highest fracture toughness. They deformed smoothly during indentation through the formation of thin shear bands. After annealing, the samples became more and more brittle, which was attributed to densification and possibly also the formation of nanocrystallites. This shows the mechanical properties of these amorphous alloys are thermally sensitive and may degrade even when no signs of crystallization are observed.

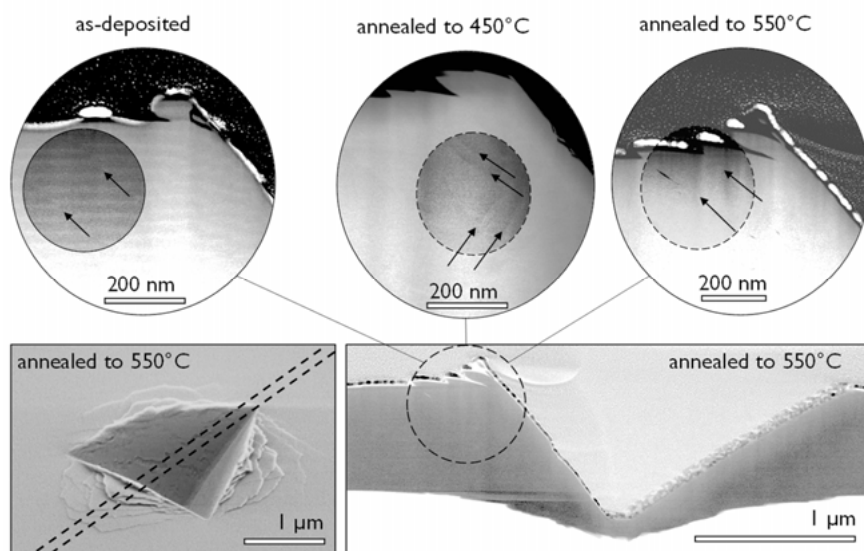


Figure 47. Cross-section study of the indents in the as-deposited CrFeNiTa alloy, as well as annealed to 450 and 550 °C. The SEM in the bottom left corner shows the approximate position of the lamella. The bottom right STEM HAAEDF image is an overview of the indent in the sample annealed to 550 °C and the three upper images are close-ups of the indents in different samples at the approximate position marked by the circle. A small section of each image is presented with a higher contrast to better visualize the shear bands, which are marked out with black arrows. The striped pattern in the as-deposited sample is due to a slight (<1 at%) variation in the Ta content, most likely caused by variations in the working pressure during deposition. Unpublished data.

Conclusions and future work

The aim of this thesis was to explore multicomponent alloys (MCAs) through magnetron sputtering and to find principles for designing new corrosion resistant coatings based on this materials class. The main conclusions are summarized below.

There are fundamental differences between synthesizing the CoCrFeMnNi MCA through magnetron sputtering compared to casting. While a single phase is easily formed from the melt, magnetron sputtering occurs at low temperatures where the single phase is not thermodynamically stable. Combined with the relatively rapid diffusion on the surface of the growing coating and in the closely spaced grain boundaries, this means that the equilibrium phases are more easily formed through magnetron sputtering. This was the main conclusion in Paper I.

The principles found for CoCrFeMnNi could explain trends seen in the literature for phase formation in other MCAs. MCAs that form a single phase through casting were sometimes multi-phase in the magnetron sputtered coatings. On the other hand, alloys that had no thermodynamically stable single-phase region could sometimes form metastable single-phase coatings.

It was also found that the phase formation could be controlled by epitaxial stabilization with crystalline substrates. In Paper II, the deposition of CoCrFeMnNi on polycrystalline stainless steel was studied. The growth mode varied greatly between the differently oriented substrate grains, leading to differences in texture, morphology, and coating thickness. The mechanisms were not fully explained, but they appeared to be related to the surface structures of different crystal grains. The substrate grain orientation also affected the formation of stacking fault structures, which were found in this alloy due to its low stacking fault energy.

The MCAs in Paper III, CrFeNiTa and CrFeNiW, had higher glass-forming abilities than CoCrFeMnNi. Most of them formed amorphous coatings. Ta or W was added to extend the passive region to higher electrochemical potentials, where the Cr-rich oxides are not stable. The ability of Ta or W to passivate the alloys was predicted using percolation theory. The experiments confirmed the prediction for the CrFeNiTa system, but not for the CrFeNiW system. It was found that the incorporation of Ta or W into the initially formed oxide was a key factor for the successful extension of the passive region. Less W than Ta was found in the initial oxide due to the higher nobility of W, which led to irreversible damage of the surface when Cr was dissolved. This was why

percolation theory could not predict the behavior of W. A new criterion for designing corrosion resistant MCAs was proposed: all passivating elements should have similar nobilities.

The addition of carbon to the MCAs in this study was expected to result in decomposition to multiple phases with different compositions. This is because the elements have widely varying carbide forming abilities. However, through magnetron sputtering, carbon could be added without leading to a segregation of the metals. This was discovered in Paper IV.

The properties of the MCAs with carbon were different depending on the carbon concentration, as shown in Papers V, VI, and VII. At lower carbon contents, the alloys formed a single amorphous phase. At higher carbon contents, a separate phase with free carbon was formed. The carbon-containing single-phase materials were more corrosion resistant, harder, and more crack resistant than the pure alloy. When free carbon was formed, the coatings became softer, but the corrosion resistance was not affected.

Here follows a short list of related studies that would be interesting for the future.

- The methodology used in Paper II has great potential for future studies. The effect of crystal orientation on the properties of MCA (or other fcc alloys) coatings on polycrystalline steel substrates is interesting for several potential applications. One way to study this would be to modify the texture of the steel by adapting the synthesis and annealing procedures. The overall corrosion resistance of coatings deposited on different textures could then be measured. Tensile tests could be used to measure the crack densities. This could be used to find substrate-coating combinations with lower overall corrosion rates and less severe cracking.
- There are also more fundamental questions that could be answered using the method from Paper II. For example, the effect of nanocrystallinity on corrosion is not yet understood, as mentioned in Section 7.2. In a recent review, it was stated that it has been difficult to study the effect since the synthesis of samples with different grain sizes requires different synthesis conditions or even different synthesis methods. This means that there are other critical differences between the materials, other than the grain size, that affect their corrosion performance [148]. In Paper II, regions with columnar morphology and single crystals were deposited side by side under the same conditions and with the same composition. These could be used to better isolate the effect of grain boundary density by studying them with localized electrochemical techniques [149].
- The effect of stacking faults on the mechanical properties of coatings has not yet been systematically explored. By mapping the

surfaces of the samples from Paper II, the mechanical response could be correlated to the density and type of stacking faults found on different substrate grains.

- The principles found in Paper III can be used to predict new promising alloy compositions. A second, less, or equally noble passive element is expected to extend the passivity of stainless steel-like MCAs. 3d-metal alloys with added Nb or Ti could therefore yield good results.
- The phase formation of CrFeNi coatings with an added refractory metal could be tuned with the sputter deposition parameters. If the diffusion rate is high enough to prevent amorphization but low enough to avoid forming multiple phases, a meta-stable fcc phase could be achieved. This was already observed for the CrFeNiW coatings with 13 at% W. Alloys with a simple fcc structure are expected to be more ductile than the amorphous alloys presented in this work, and more ductile than bcc alloys in general. This would unlock the full potential of this design approach, by combining the benefits of the 3d-transition metal and refractory metal groups.
- The addition of carbon to MCAs should be further explored. The first step would be to study the deposition parameters. In a study by Suszko et al [113], carbon was added to a sputtered 316L stainless steel coating (similar to the Cantor alloy). The carbon source was ethylene gas instead of graphite and the substrate was heated to 300°C instead of unheated as in this work. The resulting material was an alloy/amorphous carbon nanocomposite with a self-organized nanotubular structure, which possessed a unique combination of hardness and toughness. It would therefore be interesting to attempt to recreate these deposition conditions for the addition of carbon to MCAs.

Populärvetenskaplig sammanfattning

Målet med detta projekt är att utveckla designprinciper för metalliska ytbeläggningar som kan skydda komponenter från korrosion, det vill säga den destruktiva oxidationen av metallen. Fokuset har legat på beläggningar på stålkomponenter i elektrokemiska anordningar där vätgas används för energilagring. Ett exempel är elektrolysörer som används för att tillverka vätgas från vatten genom att tillföra elektrisk energi, eller bränsleceller som bygger på motsatt process: vätgasen och syrgas från luften får bilda vatten igen och elektrisk energi utvinns i processen. I båda fallen utsätts materialen inuti cellerna för en korrosiv miljö och det behövs ytbeläggningar som kan göra cellerna mer hållbara. För att kunna appliceras industriellt behöver beläggningarna, förutom att ha ett högt korrosionsmotstånd, även vara både hårda och formbara för att inte nötas eller spricka under tillverkningsprocessen. De ska även vara billiga och ha god elektrisk ledningsförmåga.

Multikomponentlegeringar (MCA efter multicomponent alloy) eller högentropilegeringar (HEA, efter engelskans high entropy alloy) som de ibland kallas, är en ny typ av material som upptäcktes år 2004. Legeringarna tillverkas genom att blanda lika delar av många (minst fyra) metalliska element. I legeringar med många olika metaller kan det lätt bildas flera faser, det vill säga en uppdelning i områden med olika kristallstrukturer och koncentrationer. Detta sker eftersom vissa av metallerna binder starkare till varandra, så entalpin (den inre energin) hos systemet kan sänkas på detta vis. Den klassiska definitionen av en HEA är ett material som i stället bildar en enda kristallin fas där alla element är blandade, eftersom den ökade entropin (oordningen) i den blandade fasen blir viktigare än entalpin. Eftersom materialklassen är ny och det finns ett nästan obegränsat antal sammansättningar att upptäcka, behövs det göras systematiska studier för att finna principer och tumregler för hur egenskaperna hos dessa material kan ändras och optimeras.

Egenskaperna hos ett material beror dels av koncentrationerna av olika element, men lika mycket av kristallstrukturen, det regelbundna mönster av atomer som sträcker sig genom varje korn, och mikrostrukturen, kristallkornens storlek och form. Andra faktorer på mikrometer- och nanometer-skala kan också vara viktiga. Det kan exempelvis vara om materialet är homogent eller har fluktuationer i den kemiska sammansättningen, och olika typer av defekter. I en MCA finns det stora möjligheter att styra alla dessa faktorer. Det finns exempelvis fördelar med att bilda en kristallin fas i stället för flera. Blandningar av faser kan visserligen göra materialet hårdare, men det bidrar också

till lättare sprickbildning, och kan även leda till att korrosionsmotståndet minskar.

Tre olika legeringar i klassen MCA valdes ut i detta projekt. Beläggningarna tillverkades med magnetronsputtring (även kallad katodförstötning). Joner accelereras framför metallplattor av de önskade elementen, och dessa joner slår då ut atomer från plattan. Atomerna landar sedan på komponenten som ska beläggas och en tunn film, ofta mindre än en mikrometer, byggs upp atom för atom. Med denna metod har man hög kontroll över vissa processer som är svårare att styra med traditionella bulkmetoder, som smältning och gjutning. Bland annat kan atomernas rörlighet (diffusionen) bättre kontrolleras under tillverkningsprocessen. Om diffusionen begränsas tillräckligt kan systemet inte gå mot termodynamisk jämvikt, alltså det tillstånd som minimerar den totala energin. I stället kan det ”stelna” i ett tillstånd som kräver mindre diffusion.

När MCA studerades med magnetronsputtring i detta projekt, visade det sig att termodynamiken är av mindre vikt än när man tillverkar MCA som bulkmaterial. Ökningen av entropin har ingen märkbar effekt när diffusionen är mycket begränsad. Men enfasiga material kunde ändå tillverkas med hjälp av magnetronsputtring. Anledningen var att den begränsade diffusionen även stoppade bildandet av flera faser, eftersom uppdelningen skulle kräva att atomerna diffunderar längre sträckor. Vissa av legeringarna blev amorfa. Det innebär att atomerna inte är ordnade på ett regelbundet vis, det vill säga att de inte har en definierad kristallstruktur. Amorfa material är vanliga i andra materialklasser, bland annat är alla typer av glas amorfa. Det är dock ovanligt för metallegeringar, eftersom de har en hög drivkraft att kristallisera.

Flera sätt att förbättra korrosionsegenskaperna undersöktes. Elementen Cr, Fe och Ni användes som utgångspunkt och tillsatser av Mn, Co, Ta och/eller W användes för att skapa olika MCAs. Eftersom legeringarna innehåller de huvudsakliga elementen i ett rostfritt stål är de intressanta som ytbeläggningar på just stål, eftersom likheterna kan ge en överföring av materialegenskaper som kristallstruktur och kornorientering. Detta undersöktes systematiskt för en av legeringarna. Det visade sig att relationen mellan stålet och beläggningen hade en enorm inverkan på beläggningens egenskaper, vilket förväntas påverka både dess korrosionsresistens och mekaniska egenskaper.

Ett av de mest lovande materialen i detta projekt var en tunnfilm av CrFe-NiTa. I ett vanligt stål är det kromet som skyddar mot korrosion genom att bilda ett svårslösligt skikt av kromrika oxider. Men när stål utsätts för en hög elektrisk potential, förlorar kromet elektroner och kan då bara bilda lättlösliga föreningar. Detta lämnar stålet oskyddat. Så är fallet i till exempel en elektrolysör, där en hög spänningsskillnad behövs för att oxidera vattnet. I CrFeNiTa kan Ta då ”ta över” skyddet genom att bilda en Ta-rik oxid, och materialet kan användas i mycket mer aggressiva miljöer. Detta material var även bättre än rent Ta, eftersom Ta vid höga potentialer bildar en elektriskt isolerande oxid

som ökar kontaktresistensen. CrFeNiTa är alltså som ett ”superstål” som kombinerar de bästa egenskaperna av båda materialen.

En annan metod för att förbättra hårdheten och korrosionsmotståndet, och minska sprickbildningen, var att tillsätta kol till MCA-beläggningarna. I dessa experiment blev diffusionskontrollen återigen viktig för resultatet. När systemet tillåts att gå mot jämvikt, leder kolet till en separation av kristallina faser. Bland annat bildas mycket hårda och spröda metallkarbider. Kromet, som är det element som skyddar materialet mot korrosion, ansamlas till vissa korn, vilket lämnar andra korn helt oskyddade. Genom att begränsa atomernas rörlighet kunde detta undvikas. I stället bildades ett material som var helt homogent och amorft. Amorfa legeringar har egenskaper som skiljer sig starkt från de vanliga kristallina motsvarigheterna, och det finns i allmänhet mindre teoretisk kunskap om dessa. I detta fall blev det amorfa materialet med kol hårdare och mer tåligt mot sprickbildning än det kristallina. Även korrosionsmotståndet förbättrades, en effekt som ökade med mängden kol i beläggningen.

Acknowledgments

First of all, I want to thank Ulf Jansson for being an incredibly dedicated and reliable supervisor. Our meetings were always challenging and never boring. Your most important comment is permanently etched into my brain: *What's your scientific question?* To my second supervisor Leif Nyholm: thank you for teaching me your thorough and systematic approach to science. I will always remember your best advice: *A hypothesis is better than no hypothesis.*

Next, I want to thank my three best mentors: Rebecka Lindblad, Maria Paschalidou, and Erik Lewin, who have shared their awesome knowledge on everything from vacuum pumps to how to survive in academia without going insane. I want to thank Pedro Berastegui and David Rehnlund for my introduction to research. In the lab, I would not have gotten far without Mikael Ottosson, Leif Edlén, Amit Patel, Victoria Sternhagen, and Peter Bergkvist.

For the great collaborations with other groups, I want to thank: Live Mölmen and Peter Leisner at Jönköping university, Greta Lindwall at KTH, Marcus Tavares and Kristofer Gamstedt at Applied Mechanics, Marcos Moro, Petter Ström and Daniel Primetzhofer at the Tandem laboratory, Szilárd Kolozsvári at Plansee, and Lisa Lautrup at Alleima. To Lars Riekehr and Olivier Donzel-Gargand: I cannot thank you enough for your TEM work.

I would like to thank everyone in the FunMat-II center who made this project possible. Particularly Smita, Rui, Clara, and Michael: I think each of you will find some of your suggestions implemented in my papers. I also want to thank Peter Polcik and everyone at Plansee for the sputter targets.

I feel lucky to have worked with so many clever and kind people in the Inorganic and Structural Chemistry groups. I know I'm not the best at joining parties, but I'm glad for the times that I did! I've enjoyed some dancing, some strange competitions, and even some casual pyromania. Thank you, Anna, for being a wonderful collaborator and friend! Babsi: we never seem to end up on the same papers, but you have been a real companion in science and life. This would have been much harder and more boring without you. A special thanks to the people who have helped me out and taught me new things: Aishwarya, Katalin, Kristina, Simon C, Stefan, Johan, Markus, Paulius, Hanna and more.

Finally, to everyone on the outside. Mom and Dad. My partners, Jörn and Justin. Everyone in my friends-family. You are the main reason why my PhD years have been a happy and (relatively) balanced time. An extra special thanks to Justin and Mom for all the free proofreading and style advice over the years, and to Therese for making the cover of this book.

References

- [1] B. Mallet, Repair work on stress corrosion at Civaux 1 reactor completed, Nasdaq. (2022). <https://www.nasdaq.com/articles/repair-work-on-stress-corrosion-at-civaux-1-reactor-completed> (accessed October 27, 2022).
- [2] French regulator gives update on corrosion issue, World Nucl. News. (2022). <https://www.world-nuclear-news.org/Articles/French-regulator-gives-update-on-corrosion-issue> (accessed October 27, 2022).
- [3] Safety-relevant damage in the safety injection systems of French nuclear power plants, Gesellschaft Für Anlagen- Und Reakt. (GRS), GGmbH. (2022). <https://www.grs.de/en/news/safety-relevant-damage-safety-injection-systems-french-nuclear-power-plants> (accessed November 4, 2022).
- [4] G. Koch, Cost of corrosion, Trends Oil Gas Corros. Res. Technol. Prod. Transm. (2017) 3–30. <https://doi.org/10.1016/B978-0-08-101105-8.00001-2>.
- [5] D. Hoepfner, V. Chandrasekaran, A. Taylor, Review of pitting corrosion fatigue models, Comm. Aeronaut. Fatigue. (1999) 1–25.
- [6] Stress Corrosion Cracking in Light Water Reactors: Good Practices and Lessons Learned, Int. At. Energy Agency. (2011). <http://www.iaea.org/Publications/index.html> (accessed November 4, 2022).
- [7] B.D. James, J.M. Huya-Kouadio, C. Houchins, Bipolar Plate Cost and Issues at High Production Rate, 2017. https://www.energy.gov/sites/prod/files/2017/05/f34/fcto_bipolar_plates_wkshp_james.pdf (accessed March 12, 2021).
- [8] B. Cantor, I.T.H. Chang, P. Knight, A.J.B. Vincent, Microstructural development in equiatomic multicomponent alloys, Mater. Sci. Eng. A. 375–377 (2004) 213–218. <https://doi.org/10.1016/j.msea.2003.10.257>.
- [9] J.W. Yeh, S.K. Chen, S.J. Lin, J.Y. Gan, T.S. Chin, T.T. Shun, C.H. Tsau, S.Y. Chang, Nanostructured high-entropy alloys with multiple principal elements: Novel alloy design concepts and outcomes, Adv. Eng. Mater. 6 (2004) 299–303+274. <https://doi.org/10.1002/adem.200300567>.
- [10] K. Nygren, Magnetron Sputtering of Nanocomposite Carbide Coatings for Electrical Contacts, PhD thesis, Acta Universitatis Upsaliensis, Uppsala, 2016.
- [11] A. Höling, L. Hultman, M. Odén, J. Sjölen, L. Karlsson, Mechanical properties and machining performance of Ti1–xAlxN-coated cutting tools, Surf. Coatings Technol. 191 (2005) 384–392. <https://doi.org/10.1016/J.SURFCOAT.2004.04.056>.
- [12] M.J. Godbole, A.J. Pedraza, L.F. Allard, G. Geesey, Characterization of sputter-deposited 316L stainless steel films, J. Mater. Sci. 27 (1992) 5585–5590. <https://doi.org/10.1007/BF00541627>.
- [13] A.L. Greer, Confusion by design, Nat. 1993 3666453. 366 (1993) 303–304.

- <https://doi.org/10.1038/366303a0>.
- [14] J. Yeh, S. Chen, J. Gan, S. Lin, Communications: Formation of Simple Crystal Structures in Cu-Co-Ni-Cr-Al-Fe-Ti-V Alloys with Multiprincipal Metallic Elements, 35 (2004).
 - [15] T.K. Chen, M.S. Wong, T.T. Shun, J.W. Yeh, Nanostructured nitride films of multi-element high-entropy alloys by reactive DC sputtering, *Surf. Coatings Technol.* 200 (2005) 1361–1365. <https://doi.org/10.1016/j.surfcoat.2005.08.081>.
 - [16] D.B. Miracle, O.N. Senkov, A critical review of high entropy alloys and related concepts, *Acta Mater.* 122 (2017) 448–511. <https://doi.org/10.1016/J.ACTAMAT.2016.08.081>.
 - [17] M.C. Tropicovsky, J.R. Morris, P.R.C. Kent, A.R. Lupini, G.M. Stocks, Criteria for predicting the formation of single-phase high-entropy alloys, *Phys. Rev. X* 5 (2015) 1–6. <https://doi.org/10.1103/PhysRevX.5.011041>.
 - [18] C. Zhang, M.C. Gao, CALPHAD modeling of high-entropy alloys, in: *High-Entropy Alloy. Fundam. Appl.*, Springer International Publishing, 2016: pp. 399–444. https://doi.org/10.1007/978-3-319-27013-5_12.
 - [19] Z. Tang, L. Huang, W. He, P.K. Liaw, Alloying and Processing Effects on the Aqueous Corrosion Behavior of High-Entropy Alloys, *Entropy* 2014, Vol. 16, Pages 895–911. 16 (2014) 895–911. <https://doi.org/10.3390/E16020895>.
 - [20] Y. Lu, Y. Dong, S. Guo, L. Jiang, H. Kang, T. Wang, B. Wen, Z. Wang, J. Jie, Z. Cao, H. Ruan, T. Li, A Promising New Class of High-Temperature Alloys: Eutectic High-Entropy Alloys, *Sci. Reports* 2014 41. 4 (2014) 1–5. <https://doi.org/10.1038/srep06200>.
 - [21] Z.Y. Ding, Q.F. He, D. Chung, Y. Yang, Evading brittle fracture in submicron-sized high entropy intermetallics in dual-phase eutectic microstructure, *Scr. Mater.* 187 (2020) 280–284. <https://doi.org/10.1016/J.SCRIPTAMAT.2020.06.032>.
 - [22] S.B. Inman, J. Han, A.Y. Gerard, J. Qi, M.A. Wischhusen, S.R. Agnew, S.J. Poon, K. Ogle, J.R. Scully, Effect of Mn Content on the Passivation and Corrosion of Al_{0.3}Cr_{0.5}Fe₂Mn_xMo_{0.15}Ni_{1.5}Ti_{0.3} Compositionally Complex Face-Centered Cubic Alloys, *Corrosion* 78 (2022) 32–48. <https://doi.org/10.5006/3906>.
 - [23] J.Y. He, W.H. Liu, H. Wang, Y. Wu, X.J. Liu, T.G. Nieh, Z.P. Lu, Effects of Al addition on structural evolution and tensile properties of the FeCoNiCrMn high-entropy alloy system, *Acta Mater.* 62 (2014) 105–113. <https://doi.org/10.1016/j.actamat.2013.09.037>.
 - [24] L. Ma, L. Wang, T. Zhang, A. Inoue, Bulk Glass Formation of Ti-Zr-Hf-Cu-M (M=Fe, Co, Ni) Alloys, *Mater. Trans.* 43 (2002) 277–280. <https://doi.org/10.2320/MATERTRANS.43.277>.
 - [25] A. Inoue, Stabilization of metallic supercooled liquid and bulk amorphous alloys, *Acta Mater.* 48 (2000) 279–306. [https://doi.org/10.1016/S1359-6454\(99\)00300-6](https://doi.org/10.1016/S1359-6454(99)00300-6).
 - [26] Y. Zhang, Y.J. Zhou, J.P. Lin, G.L. Chen, P.K. Liaw, Solid-Solution Phase Formation Rules for Multi-component Alloys, *Adv. Eng. Mater.* 10 (2008) 534–538. <https://doi.org/10.1002/adem.200700240>.

- [27] W. Huo, F. Fang, X. Liu, S. Tan, Z. Xie, J. Jiang, Fatigue resistance of nanotwinned high-entropy alloy films, *Mater. Sci. Eng. A.* 739 (2019) 26–30. <https://doi.org/10.1016/j.msea.2018.09.112>.
- [28] Y.F. Ye, Q. Wang, J. Lu, C.T. Liu, Y. Yang, High-entropy alloy: challenges and prospects, *Mater. Today.* 19 (2016) 349–362. <https://doi.org/10.1016/j.mattod.2015.11.026>.
- [29] J.E. Saal, I.S. Berglund, J.T. Sebastian, P.K. Liaw, G.B. Olson, Equilibrium high entropy alloy phase stability from experiments and thermodynamic modeling, *Scr. Mater.* 146 (2018) 5–8. <https://doi.org/10.1016/j.scriptamat.2017.10.027>.
- [30] F. Otto, A. Dlouhý, K.G. Pradeep, M. Kuběnová, D. Raabe, G. Eggeler, E.P. George, Decomposition of the single-phase high-entropy alloy CrMnFeCoNi after prolonged anneals at intermediate temperatures, *Acta Mater.* 112 (2016) 40–52. <https://doi.org/10.1016/j.actamat.2016.04.005>.
- [31] B. Schuh, F. Mendez-Martin, B. Völker, E.P. George, H. Clemens, R. Pippin, A. Hohenwarter, Mechanical properties, microstructure and thermal stability of a nanocrystalline CoCrFeMnNi high-entropy alloy after severe plastic deformation, *Acta Mater.* 96 (2015) 258–268. <https://doi.org/10.1016/j.actamat.2015.06.025>.
- [32] Y.J. Li, A. Savan, A. Kostka, H.S. Stein, A. Ludwig, Accelerated atomic-scale exploration of phase evolution in compositionally complex materials, *Mater. Horizons.* 5 (2018) 86–92. <https://doi.org/10.1039/c7mh00486a>.
- [33] A. Kauffmann, M. Stüber, H. Leiste, S. Ulrich, S. Schlabach, D.V. Szabó, S. Seils, B. Gorr, H. Chen, H.J. Seifert, M. Heilmaier, Combinatorial exploration of the High Entropy Alloy System Co-Cr-Fe-Mn-Ni, *Surf. Coatings Technol.* 325 (2017) 174–180. <https://doi.org/10.1016/j.surfcoat.2017.06.041>.
- [34] S. Fang, C. Wang, C.L. Li, J.H. Luan, Z.B. Jiao, C.T. Liu, C.H. Hsueh, Microstructures and mechanical properties of CoCrFeMnNiV_x high entropy alloy films, *J. Alloys Compd.* 820 (2020) 153388. <https://doi.org/10.1016/j.jallcom.2019.153388>.
- [35] Y.-C. Hsu, C.-L. Li, C.-H. Hsueh, Effects of Al Addition on Microstructures and Mechanical Properties of CoCrFeMnNiAl_x High Entropy Alloy Films, *Entropy.* 22 (2019) 2. <https://doi.org/10.3390/e22010002>.
- [36] C. Dang, J.U. Surjadi, L. Gao, Y. Lu, Mechanical Properties of Nanostructured CoCrFeNiMn High-Entropy Alloy (HEA) Coating, *Front. Mater.* 5 (2018) 1–6. <https://doi.org/10.3389/fmats.2018.00041>.
- [37] C. Sha, Z. Zhou, Z. Xie, P. Munroe, High entropy alloy FeMnNiCoCr coatings: Enhanced hardness and damage-tolerance through a dual-phase structure and nanotwins, *Surf. Coatings Technol.* 385 (2020) 125435. <https://doi.org/10.1016/j.surfcoat.2020.125435>.
- [38] Y. Qiu, S. Thomas, M.A. Gibson, H.L. Fraser, N. Birbilis, Corrosion of high entropy alloys, *Npj Mater. Degrad.* 1 (2017) 15. <https://doi.org/10.1038/s41529-017-0009-y>.
- [39] C.O.A. Olsson, D. Landolt, Passive films on stainless steels - Chemistry, structure and growth, *Electrochim. Acta.* 48 (2003) 1093–1104. [https://doi.org/10.1016/S0013-4686\(02\)00841-1](https://doi.org/10.1016/S0013-4686(02)00841-1).

- [40] H. Luo, Z. Li, A.M. Mingers, D. Raabe, Corrosion behavior of an equiatomic CoCrFeMnNi high-entropy alloy compared with 304 stainless steel in sulfuric acid solution, *Corros. Sci.* 134 (2018) 131–139. <https://doi.org/10.1016/j.corsci.2018.02.031>.
- [41] B. Gludovatz, A. Hohenwarter, D. Catoor, E.H. Chang, E.P. George, R.O. Ritchie, A fracture-resistant high-entropy alloy for cryogenic applications, *Science* (80-.). 345 (2014) 1153–1158. <https://doi.org/10.1126/science.1254581>.
- [42] Y.H. Zhao, Y.T. Zhu, X.Z. Liao, Z. Horita, T.G. Langdon, Tailoring stacking fault energy for high ductility and high strength in ultrafine grained Cu and its alloy, *Appl. Phys. Lett.* 89 (2006) 121906. <https://doi.org/10.1063/1.2356310>.
- [43] L. Sun, X. He, J. Lu, Nanotwinned and hierarchical nanotwinned metals: a review of experimental, computational and theoretical efforts, *Npj Comput. Mater.* 2018 41. 4 (2018) 1–18. <https://doi.org/10.1038/s41524-018-0062-2>.
- [44] T.Z. Khan, T. Kirk, G. Vazquez, P. Singh, A. V. Smirnov, D.D. Johnson, K. Youssef, R. Arróyave, Towards stacking fault energy engineering in FCC high entropy alloys, *Acta Mater.* 224 (2022) 117472. <https://doi.org/10.1016/J.ACTAMAT.2021.117472>.
- [45] S. Huang, W. Li, S. Lu, F. Tian, J. Shen, E. Holmström, L. Vitos, Temperature dependent stacking fault energy of FeCrCoNiMn high entropy alloy, *Scr. Mater.* 108 (2015) 44–47. <https://doi.org/10.1016/J.SCRIPTAMAT.2015.05.041>.
- [46] S. Huang, H. Huang, W. Li, D. Kim, S. Lu, X. Li, E. Holmström, S.K. Kwon, L. Vitos, Twinning in metastable high-entropy alloys, *Nat. Commun.* 9 (2018) 1–7. <https://doi.org/10.1038/s41467-018-04780-x>.
- [47] Z. Wang, C. Wang, Y.L. Zhao, Y.C. Hsu, C.L. Li, J.J. Kai, C.T. Liu, C.H. Hsueh, High hardness and fatigue resistance of CoCrFeMnNi high entropy alloy films with ultrahigh-density nanotwins, *Int. J. Plast.* 131 (2020) 102726. <https://doi.org/10.1016/J.IJPLAS.2020.102726>.
- [48] X. Zhou, X. Li, C. Chen, Atomistic mechanisms of fatigue in nanotwinned metals, *Acta Mater.* 99 (2015) 77–86. <https://doi.org/10.1016/J.ACTAMAT.2015.07.045>.
- [49] P. Sarker, T. Harrington, C. Toher, C. Oses, M. Samiee, J.P. Maria, D.W. Brenner, K.S. Vecchio, S. Curtarolo, High-entropy high-hardness metal carbides discovered by entropy descriptors, *Nat. Commun.* 9 (2018) 1–10. <https://doi.org/10.1038/s41467-018-07160-7>.
- [50] J.T. Fan, L.J. Zhang, P.F. Yu, M.D. Zhang, D.J. Liu, Z. Zhou, P. Cui, M.Z. Ma, Q. Jing, G. Li, R.P. Liu, Improved the microstructure and mechanical properties of AlFeCoNi high-entropy alloy by carbon addition, *Mater. Sci. Eng. A.* 728 (2018) 30–39. <https://doi.org/10.1016/j.msea.2018.05.013>.
- [51] H. Cheng, W. Chen, X. Liu, Q. Tang, Y. Xie, P. Dai, Effect of Ti and C additions on the microstructure and mechanical properties of the FeCoCrNiMn high-entropy alloy, *Mater. Sci. Eng. A.* 719 (2018) 192–198. <https://doi.org/10.1016/J.MSEA.2018.02.040>.
- [52] M. Beyramali Kivy, C.S. Kriewall, M. Asle Zaeem, Formation of chromium-iron carbide by carbon diffusion in AlXCoCrFeNiCu high-

- entropy alloys, *Mater. Res. Lett.* 6 (2018) 321–326.
<https://doi.org/10.1080/21663831.2018.1449767>.
- [53] I. Baker, Interstitials in f.c.c. high entropy alloys, *Metals* (Basel). 10 (2020) 1–20. <https://doi.org/10.3390/met10050695>.
- [54] H. Luo, S. Zou, Y.H. Chen, Z. Li, C. Du, X. Li, Influence of carbon on the corrosion behaviour of interstitial equiatomic CoCrFeMnNi high-entropy alloys in a chlorinated concrete solution, *Corros. Sci.* 163 (2020) 108287. <https://doi.org/10.1016/j.corsci.2019.108287>.
- [55] J. Chen, Z. Yao, X. Wang, Y. Lu, X. Wang, Y. Liu, X. Fan, Effect of C content on microstructure and tensile properties of as-cast CoCrFeMnNi high entropy alloy, *Mater. Chem. Phys.* 210 (2018) 136–145. <https://doi.org/10.1016/j.matchemphys.2017.08.011>.
- [56] L. Yang, C. Liu, M. Wen, X. Dai, Y. Zhang, X. Chen, K. Zhang, Small atoms as reinforced agent for both hardness and toughness of Group-VIB transition metal films, *J. Alloys Compd.* 735 (2018) 1105–1110. <https://doi.org/10.1016/j.jallcom.2017.11.208>.
- [57] S. Fritze, P. Malinovskis, L. Riekehr, L. von Fieandt, E. Lewin, U. Jansson, Hard and crack resistant carbon supersaturated refractory nanostructured multicomponent coatings, *Sci. Rep.* 8 (2018) 1–8. <https://doi.org/10.1038/s41598-018-32932-y>.
- [58] K. Nygren, M. Andersson, J. Höglström, W. Fredriksson, K. Edström, L. Nyholm, U. Jansson, Influence of deposition temperature and amorphous carbon on microstructure and oxidation resistance of magnetron sputtered nanocomposite CrC films, *Appl. Surf. Sci.* 305 (2014) 143–153. <https://doi.org/10.1016/j.apsusc.2014.03.014>.
- [59] U. Jansson, E. Lewin, Sputter deposition of transition-metal carbide films - A critical review from a chemical perspective, *Thin Solid Films.* 536 (2013) 1–24. <https://doi.org/10.1016/j.tsf.2013.02.019>.
- [60] U. Jansson, E. Lewin, Carbon-containing multi-component thin films, *Thin Solid Films.* 688 (2019) 137411. <https://doi.org/10.1016/j.tsf.2019.137411>.
- [61] W. Sheng, X. Yang, C. Wang, Y. Zhang, Nano-crystallization of high-entropy amorphous NbTiAlSiW_x films prepared by magnetron sputtering, *Entropy.* 18 (2016). <https://doi.org/10.3390/e18060226>.
- [62] J.R. Scully, S.B. Inman, A.Y. Gerard, C.D. Taylor, W. Windl, D.K. Schreiber, P. Lu, J.E. Saal, G.S. Frankel, Controlling the corrosion resistance of multi-principal element alloys, *Scr. Mater.* 188 (2020) 96–101. <https://doi.org/10.1016/j.scriptamat.2020.06.065>.
- [63] N. Birbilis, S. Choudhary, J.R. Scully, M.L. Taheri, A perspective on corrosion of multi-principal element alloys, *Npj Mater. Degrad.* 2021 51. 5 (2021) 1–8. <https://doi.org/10.1038/s41529-021-00163-8>.
- [64] J. Dąbrowa, M. Zajusz, W. Kucza, G. Cieślak, K. Berent, T. Czeppe, T. Kulik, M. Danielewski, Demystifying the sluggish diffusion effect in high entropy alloys, *J. Alloys Compd.* 783 (2019) 193–207. <https://doi.org/10.1016/J.JALLCOM.2018.12.300>.
- [65] Raw Materials Information System, (n.d.). <https://rmis.jrc.ec.europa.eu/> (accessed November 5, 2022).
- [66] W. Li, P. Liu, P.K. Liaw, Microstructures and properties of high-entropy

- alloy films and coatings: A review, *Mater. Res. Lett.* 6 (2018) 199–229.
<https://doi.org/10.1080/21663831.2018.1434248>.
- [67] A.K. Mallik, Computer calculations of phase diagrams, *Bull. Mater. Sci.* 8 (1986) 107–121. <https://doi.org/10.1007/BF02744176>.
- [68] T.-C. Software, TCHEA3: TCS High Entropy Alloy Database, (2018).
https://www.thermocalc.com/media/35873/tchea3_extended_info.pdf
 (accessed December 16, 2019).
- [69] T. Gebhardt, D. Music, T. Takahashi, J.M. Schneider, Combinatorial thin film materials science: From alloy discovery and optimization to alloy design, *Thin Solid Films*. 520 (2012) 5491–5499.
<https://doi.org/10.1016/J.TSF.2012.04.062>.
- [70] A. Marshal, K.G. Pradeep, D. Music, S. Zaefferer, P.S. De, J.M. Schneider, Combinatorial synthesis of high entropy alloys: Introduction of a novel, single phase, body-centered-cubic FeMnCoCrAl solid solution, *J. Alloys Compd.* 691 (2017) 683–689. <https://doi.org/10.1016/j.jallcom.2016.08.326>.
- [71] C. Kalha, N.K. Fernando, P. Bhatt, F.O.L. Johansson, A. Lindblad, H. Rensmo, L.Z. Medina, R. Lindblad, S. Siol, L.P.H. Jeurgens, C. Cancellieri, K. Rossnagel, K. Medjanik, G. Schönhense, M. Simon, A.X. Gray, S. Nemšák, P. Lömker, C. Schlueter, A. Regoutz, Hard x-ray photoelectron spectroscopy: a snapshot of the state-of-the-art in 2020, *J. Phys. Condens. Matter*. 33 (2021) 233001. <https://doi.org/10.1088/1361-648X/ABEACD>.
- [72] K. Fu, Y. Yin, L. Chang, D. Shou, B. Zheng, L. Ye, Analysis on multiple ring-like cracks in thin amorphous carbon film on soft substrate under nanoindentation, *J. Phys. D. Appl. Phys.* 46 (2013).
<https://doi.org/10.1088/0022-3727/46/50/505314>.
- [73] W.C. Oliver, G.M. Pharr, Measurement of hardness and elastic modulus by instrumented indentation: Advances in understanding and refinements to methodology, *J. Mater. Res.* 19 (2004) 3–20.
<https://doi.org/10.1557/jmr.2004.19.1.3>.
- [74] J. Ast, M. Ghidelli, K. Durst, M. Göken, M. Sebastiani, A.M. Korsunsky, A review of experimental approaches to fracture toughness evaluation at the micro-scale, *Mater. Des.* 173 (2019) 107762.
<https://doi.org/10.1016/j.matdes.2019.107762>.
- [75] M.V. Tavares da Costa, J. Bolinsson, R.C. Neagu, P. Fayet, E.K. Gamstedt, Experimental assessment of micromechanical models for fragmentation analysis of thin metal oxide coatings on polymer films under uniaxial tensile deformation, *Surf. Coatings Technol.* 370 (2019) 374–383.
<https://doi.org/10.1016/j.surfcoat.2019.03.035>.
- [76] L. Mølmen, L. Fast, A. Lundblad, P. Eriksson, P. Leisner, Contact resistance measurement methods for PEM fuel cell bipolar plates and power terminals, *J. Power Sources*. 555 (2023) 232341.
<https://doi.org/10.1016/J.JPOWSOUR.2022.232341>.
- [77] A. Hellawell, W. Hume-Rothery, The constitution of alloys of iron and manganese with transition elements of the first long period, *Philos. Trans. R. Soc. London. Ser. A, Math. Phys. Sci.* 249 (1957) 417–459.
<https://doi.org/10.1098/rsta.1957.0004>.
- [78] J.. McMullin, S.F. Reiter, D.G. Ebeling, Equilibrium structures in Fe-Cr-

- Mo alloys, *Trans. Am. Soc. Met.* 46 (1954) 799.
- [79] C. Sha, Z. Zhou, Z. Xie, P. Munroe, Extremely hard, α -Mn type high entropy alloy coatings, *Scr. Mater.* 178 (2020) 477–482. <https://doi.org/10.1016/j.scriptamat.2019.12.029>.
- [80] A. Redjaïmia, A. Proult, P. Donnadieu, J.P. Morniroli, Morphology, crystallography and defects of the intermetallic χ -phase precipitated in a duplex ($\delta + \gamma$) stainless steel, *J. Mater. Sci.* 39 (2004) 2371–2386. <https://doi.org/10.1023/B:JMSC.0000019999.27065.13>.
- [81] D.M. Escriba, E. Materna-Morris, R.L. Plaut, A.F. Padilha, Chi-phase precipitation in a duplex stainless steel, *Mater. Charact.* 60 (2009) 1214–1219. <https://doi.org/10.1016/j.matchar.2009.04.013>.
- [82] A.F. Padilha, P.R. Rios, Decomposition of austenite in austenitic stainless steels, *ISIJ Int.* 42 (2002) 325–337. <https://doi.org/10.2355/isijinternational.42.325>.
- [83] G. Laplanche, S. Berglund, C. Reinhart, A. Kostka, F. Fox, E.P. George, Phase stability and kinetics of σ -phase precipitation in CrMnFeCoNi high-entropy alloys, *Acta Mater.* 161 (2018) 338–351. <https://doi.org/10.1016/j.actamat.2018.09.040>.
- [84] H. Shahmir, J. He, Z. Lu, M. Kawasaki, T.G. Langdon, Effect of annealing on mechanical properties of a nanocrystalline CoCrFeNiMn high-entropy alloy processed by high-pressure torsion, *Mater. Sci. Eng. A.* 676 (2016) 294–303. <https://doi.org/10.1016/j.msea.2016.08.118>.
- [85] J.Y. Zhang, Z.Y. Ding, F.C. Li, Y. Yang, Controlled synthesis of nanostructured glassy and crystalline high entropy alloy films, *Nanotechnology.* 31 (2020) 045601. <https://doi.org/10.1088/1361-6528/AB4A41>.
- [86] B.R. Braeckman, D. Depla, Structure formation and properties of sputter deposited Nb_x-CoCrCuFeNi high entropy alloy thin films, *J. Alloys Compd.* 646 (2015) 810–815. <https://doi.org/10.1016/j.jallcom.2015.06.097>.
- [87] M.X. Zhang, P.M. Kelly, Edge-to-edge matching and its applications: Part I. Application to the simple HCP/BCC system, *Acta Mater.* 53 (2005) 1073–1084. <https://doi.org/10.1016/J.ACTAMAT.2004.11.007>.
- [88] H. Bialas, K. Heneka, Epitaxy of fcc metals on dielectric substrates, *Vacuum.* 45 (1994) 79–87. [https://doi.org/10.1016/0042-207X\(94\)90346-8](https://doi.org/10.1016/0042-207X(94)90346-8).
- [89] D.L. Miller, M.W. Keller, J.M. Shaw, A.N. Chiaramonti, R.R. Keller, Epitaxial (111) films of Cu, Ni, and Cu_xNi_y on α -Al₂O₃ (0001) for graphene growth by chemical vapor deposition, *J. Appl. Phys.* 112 (2012) 064317. <https://doi.org/10.1063/1.4754013>.
- [90] A. Pandey, J. Kaushik, S. Dutta, A.K. Kapoor, D. Kaur, Electrical and structural characteristics of sputtered c-oriented AlN thin films on Si (100) and Si (110) substrates, *Thin Solid Films.* 666 (2018) 143–149. <https://doi.org/10.1016/j.tsf.2018.09.016>.
- [91] C.J. Sun, P. Kung, A. Saxler, H. Ohsato, E. Bigan, M. Razeghi, D.K. Gaskill, Thermal stability of GaN thin films grown on (0001) Al₂O₃, (0112) Al₂O₃ and (0001)Si 6H-SiC substrates, *J. Appl. Phys.* 76 (1994) 236–241. <https://doi.org/10.1063/1.357133>.
- [92] Y.N. Wen, J.M. Zhang, Surface energy calculation of the fcc metals by

- using the MAEAM, *Solid State Commun.* 144 (2007) 163–167.
<https://doi.org/10.1016/J.SSC.2007.07.012>.
- [93] A. Anders, A structure zone diagram including plasma-based deposition and ion etching, *Thin Solid Films*. 518 (2010) 4087–4090.
<https://doi.org/10.1016/j.tsf.2009.10.145>.
- [94] I. Petrov, P.B. Barna, L. Hultman, J.E. Greene, Microstructural evolution during film growth, *J. Vac. Sci. Technol. A Vacuum, Surfaces, Film.* 21 (2003) S117–S128. <https://doi.org/10.1116/1.1601610>.
- [95] G.H. Gilmer, H. Huang, T.D. De La Rubia, J.D. Torre, F. Baumann, Lattice Monte Carlo models of thin film deposition, *Thin Solid Films*. 365 (2000) 189–200. [https://doi.org/10.1016/S0040-6090\(99\)01057-3](https://doi.org/10.1016/S0040-6090(99)01057-3).
- [96] B. Emmoth, H. Bergsaker, Sticking of sputtered particles to different surfaces, *Nucl. Instruments Methods Phys. Res. Sect. B Beam Interact. with Mater. Atoms*. 33 (1988) 435–437. [https://doi.org/10.1016/0168-583X\(88\)90601-5](https://doi.org/10.1016/0168-583X(88)90601-5).
- [97] J.T. Stuckless, C.E. Wartnaby, N. Al-Sarraf, S.J.B. Dixon-Warren, M. Kovar, D.A. King, Oxygen chemisorption and oxide film growth on Ni{100}, {110}, and {111}: Sticking probabilities and microcalorimetric adsorption heats, *J. Chem. Phys.* 106 (1998) 2012.
<https://doi.org/10.1063/1.473308>.
- [98] H.E. Roosendaal, Sputtering yields of single crystalline targets, (1981) 219–256. https://doi.org/10.1007/3540105212_10.
- [99] J.L. Whitton, W.O. Hofer, U. Littmark, M. Braun, B. Emmoth, Influence of surface morphology on the angular distribution and total yield of copper sputtered by energetic argon ions, *Appl. Phys. Lett.* 36 (2008) 531.
<https://doi.org/10.1063/1.91568>.
- [100] R.T. Tung, W.R. Graham, Single atom self-diffusion on nickel surfaces, *Surf. Sci.* 97 (1980) 73–87. [https://doi.org/10.1016/0039-6028\(80\)90104-1](https://doi.org/10.1016/0039-6028(80)90104-1).
- [101] C.L. Liu, J.M. Cohen, J.B. Adams, A.F. Voter, EAM study of surface self-diffusion of single adatoms of fcc metals Ni, Cu, Al, Ag, Au, Pd, and Pt, *Surf. Sci.* 253 (1991) 334–344. [https://doi.org/10.1016/0039-6028\(91\)90604-Q](https://doi.org/10.1016/0039-6028(91)90604-Q).
- [102] P. Yang, S. Zhang, S. Pan, B. Tang, Y. Liang, X. Zhao, Z. Zhang, J. Shi, Y. Huan, Y. Shi, S.J. Pennycook, Z. Ren, G. Zhang, Q. Chen, X. Zou, Z. Liu, Y. Zhang, Epitaxial Growth of Centimeter-Scale Single-Crystal MoS₂ Monolayer on Au(111), *ACS Nano*. 14 (2020) 5036–5045.
<https://doi.org/10.1021/acsnano.0c01478>.
- [103] Q. Li, S. Xue, J. Wang, S. Shao, A.H. Kwong, A. Giwa, Z. Fan, Y. Liu, Z. Qi, J. Ding, H. Wang, J.R. Greer, H. Wang, X. Zhang, Q. Li, S. Xue, Z. Qi, J. Ding, H. Wang, X. Zhang, J. Wang, S. Shao, A.H. Kwong, A. Giwa, J.R. Greer, Z. Fan, Y. Liu, High-Strength Nanotwinned Al Alloys with 9R Phase, *Adv. Mater.* 30 (2018) 1704629. <https://doi.org/10.1002/ADMA.201704629>.
- [104] W. Lu, C.H. Liebscher, F. Yan, X. Fang, L. Li, J. Li, W. Guo, G. Dehm, D. Raabe, Z. Li, Interfacial nanophases stabilize nanotwins in high-entropy alloys, *Acta Mater.* 185 (2020) 218–232.
<https://doi.org/10.1016/J.ACTAMAT.2019.12.010>.
- [105] J. Wang, A. Misra, J.P. Hirth, Shear response of $\Sigma 3\{112\}$ twin boundaries in

- face-centered-cubic metals, *Phys. Rev. B - Condens. Matter Mater. Phys.* 83 (2011) 1–8. <https://doi.org/10.1103/PhysRevB.83.064106>.
- [106] L.L. Xiao, Z.Q. Zheng, S.W. Guo, P. Huang, F. Wang, Ultra-strong nanostructured CrMnFeCoNi high entropy alloys, *Mater. Des.* 194 (2020) 108895. <https://doi.org/10.1016/j.matdes.2020.108895>.
- [107] C. Kittel, *Introduction to Solid State Physics*, 8th ed., John Wiley & Sons, Inc, 2005.
- [108] A. Takeuchi, A. Inoue, Classification of bulk metallic glasses by atomic size difference, heat of mixing and period of constituent elements and its application to characterization of the main alloying element, *Mater. Trans.* 46 (2005) 2817–2829. <https://doi.org/10.2320/MATERTRANS.46.2817>.
- [109] M. Kaplan, G.K. Pálsson, D.M. Holzapfel, J.M. Schneider, B. Hjörvarsson, Phase formation and thermal stability of amorphous ZrNbCrMo thin films, *J. Non-Crystalline Solids X*. 9–10 (2021). <https://doi.org/10.1016/j.nocx.2021.100061>.
- [110] M. Kaplan, *Designing metallic glasses*, PhD thesis, Acta Universitatis Upsaliensis, Uppsala, 2022.
- [111] Z. Li, Interstitial equiatomic CoCrFeMnNi high-entropy alloys: carbon content, microstructure, and compositional homogeneity effects on deformation behavior, *Acta Mater.* 164 (2019) 400–412. <https://doi.org/10.1016/j.actamat.2018.10.050>.
- [112] B. Trindade, M.T. Vieira, Modification of the structural order of transition metal-carbon systems by the addition of a Group VIII element, *Mater. Sci. Eng. A*. 352 (2003) 195–201. [https://doi.org/10.1016/S0921-5093\(02\)00865-1](https://doi.org/10.1016/S0921-5093(02)00865-1).
- [113] T. Suszko, W. Gulbiński, J. Morgiel, G. Greczynski, E. Dobruchowska, P. Dłużewski, J. Lu, L. Hultman, Amorphous FeCrNi/a-C:H coatings with self-organized nanotubular structure, *Scr. Mater.* 136 (2017) 24–28. <https://doi.org/10.1016/j.scriptamat.2017.03.040>.
- [114] G. Greczynski, D. Primetzhofner, L. Hultman, Reference binding energies of transition metal carbides by core-level x-ray photoelectron spectroscopy free from Ar⁺ etching artefacts, *Appl. Surf. Sci.* 436 (2018) 102–110. <https://doi.org/10.1016/J.APSUSC.2017.11.264>.
- [115] J.C. Lascovich, R. Giorgi, S. Scaglione, Evaluation of the sp²/sp³ ratio in amorphous carbon structure by XPS and XAES, *Appl. Surf. Sci.* 47 (1991) 17–21. [https://doi.org/10.1016/0169-4332\(91\)90098-5](https://doi.org/10.1016/0169-4332(91)90098-5).
- [116] J.F. Moulder, W.F. Stickle, P.E. Sobol, K.D. Bomben, *Handbook of X-ray photoelectron spectroscopy*, Physical Electronics, Inc., Eden Prairie, Minnesota, 1995. <https://doi.org/10.1002/sia.740030412>.
- [117] M. Andersson, J. Höglström, S. Urbonaitė, A. Furlan, L. Nyholm, U. Jansson, Deposition and characterization of magnetron sputtered amorphous Cr-C films, *Vacuum*. 86 (2012) 1408–1416. <https://doi.org/10.1016/j.vacuum.2012.01.021>.
- [118] D.D. Macdonald, Passivity - The key to our metals-based civilization, *Pure Appl. Chem.* 71 (1999) 951–978. <https://doi.org/10.1351/pac199971060951>.
- [119] C.R. Simcoe, Stainless steel: the steel that does not rust — part 1, *Adv. Mater. Process.* (2015) 38–39.

- [120] K. Sieradzki, R.C. Newman, A Percolation Model for Passivation in Stainless Steels, *J. Electrochem. Soc.* 133 (1986) 1979.
<https://doi.org/10.1149/1.2109065>.
- [121] G. Grimmett, *Percolation*, Springer New York, New York, NY, 1989.
<https://doi.org/10.1007/978-1-4757-4208-4>.
- [122] V.K.S. Shante, S. Kirkpatrick, *Advances in Physics An introduction to percolation theory*, *Adv. Phys.* 20 (1971) 325–357.
<https://doi.org/http://dx.doi.org/10.1080/00018737100101261>.
- [123] V.A. Vyssotsky, E. Sonnenblick, H.L. Frisch, J.M. Hammersley, Critical percolation probabilities (site problem), *Phys. Rev.* 124 (1961) 1021–1022.
<https://doi.org/10.1103/PhysRev.123.1566>.
- [124] Y. Xie, D.M. Artymowicz, P.P. Lopes, A. Aiello, D. Wang, J.L. Hart, E. Anber, M.L. Taheri, H. Zhuang, R.C. Newman, K. Sieradzki, A percolation theory for designing corrosion-resistant alloys, *Nat. Mater.* 20 (2021) 789–793. <https://doi.org/10.1038/s41563-021-00920-9>.
- [125] P. Sotta, D. Long, The crossover from 2D to 3D percolation: Theory and numerical simulations, *Eur. Phys. J. E.* 11 (2003) 375–388.
<https://doi.org/10.1140/epje/i2002-10161-6>.
- [126] M. Pourbaix, *Atlas of Electrochemical equilibria in aqueous solutions*, NACE International Cebelcor, 1974.
- [127] S. Pathak, N. Kumar, R.S. Mishra, P.S. De, Aqueous Corrosion Behavior of Cast CoCrFeMnNi Alloy, *J. Mater. Eng. Perform.* 28 (2019) 5970–5977.
<https://doi.org/10.1007/s11665-019-04329-z>.
- [128] Z. Wang, E.-M. Paschalidou, A. Seyeux, S. Zanna, V. Maurice, P. Marcus, Mechanisms of Cr and Mo Enrichments in the Passive Oxide Film on 316L Austenitic Stainless Steel, *Front. Mater.* 6 (2019) 232.
<https://doi.org/10.3389/fmats.2019.00232>.
- [129] L. Wang, D. Mercier, S. Zanna, A. Seyeux, M. Laurent-Brocq, L. Perrière, I. Guillot, P. Marcus, L. Perriere, I. Guillot, P. Marcus, Study of the surface oxides and corrosion behaviour of an equiatomic CoCrFeMnNi high entropy alloy by XPS and ToF-SIMS, *Corros. Sci.* 167 (2020) 108507.
<https://doi.org/10.1016/j.corsci.2020.108507>.
- [130] J.P. Kollender, A.I. Mardare, A.W. Hassel, In-Situ Monitoring of Metal Dissolution during Anodization of Tantalum, *J. Electrochem. Soc.* 164 (2017) C598–C601. <https://doi.org/10.1149/2.1471709jes>.
- [131] M.S. El-Basiouny, S.A. Hassan, M.M. Hefny, On the electrochemical behaviour of tungsten: the formation and dissolution of tungsten oxide in sulphuric acid solutions, *Corros. Sci.* 20 (1980) 909–917.
[https://doi.org/10.1016/0010-938X\(80\)90123-7](https://doi.org/10.1016/0010-938X(80)90123-7).
- [132] V. Kublanovsky, A.I. Dikumar, H. Cesiulis, I. Prosycevas, Electrodeposition and corrosion properties of nanocrystalline Fe-W alloys, *Physicochem. Mech. Mater.* 7 (2008) 308–314.
<https://www.researchgate.net/publication/291982831> (accessed September 25, 2022).
- [133] K. Hashimoto, P.Y. Park, J.H. Kim, H. Yoshioka, H. Mitsui, E. Akiyama, H. Habazaki, A. Kawashima, K. Asami, Z. Grzesik, S. Mrowec, Recent progress in corrosion-resistant metastable alloys, *Mater. Sci. Eng. A.* 198

- (1995) 1–10. [https://doi.org/10.1016/0921-5093\(95\)80052-V](https://doi.org/10.1016/0921-5093(95)80052-V).
- [134] G. Aylward, T. Findlay, *Si Chemical Data*, 6th ed., John Wiley and Sons Ltd, 2008.
- [135] K.D. Ralston, N. Birbilis, C.H.J. Davies, Revealing the relationship between grain size and corrosion rate of metals, *Scr. Mater.* 63 (2010) 1201–1204. <https://doi.org/10.1016/j.scriptamat.2010.08.035>.
- [136] L. Ying, L. Li, Understanding the corrosion resistance of nanocrystalline materials: electrochemical influences, in: *Corros. Prot. Control Using Nanomater.*, Elsevier, 2012: pp. 59–85. <https://doi.org/10.1533/9780857095800.1.59>.
- [137] M.C. Biesinger, B.P. Payne, A.P. Grosvenor, L.W.M. Lau, A.R. Gerson, R.S.C. Smart, Resolving surface chemical states in XPS analysis of first row transition metals, oxides and hydroxides: Cr, Mn, Fe, Co and Ni, *Appl. Surf. Sci.* 257 (2011) 2717–2730. <https://doi.org/10.1016/j.apsusc.2010.10.051>.
- [138] G. Beamson, D. Briggs, *High Resolution XPS of Organic Polymers: The Scienta ESCA300 Database*, 1992.
- [139] J. Höglström, M. Andersson, U. Jansson, F. Björefors, L. Nyholm, On the evaluation of corrosion resistances of amorphous chromium-carbon thin-films, *Electrochim. Acta.* 122 (2014) 224–233. <https://doi.org/10.1016/j.electacta.2013.11.130>.
- [140] A.L. Greer, Y.Q. Cheng, E. Ma, Shear bands in metallic glasses, *Mater. Sci. Eng. R Reports.* 74 (2013) 71–132. <https://doi.org/10.1016/j.mser.2013.04.001>.
- [141] M.J. Buehler, A. Misra, Mechanical behavior of nanocomposites, *MRS Bull.* 44 (2019) 19–24. <https://doi.org/10.1557/MRS.2018.323/FIGURES/3>.
- [142] A.A. Voevodin, J.S. Zabinski, Load-adaptive crystalline-amorphous nanocomposites, *J. MATERIALS Sci.* 33 (1998) 319–327.
- [143] G.P. Zhang, Y. Liu, B. Zhang, Effect of annealing close to T_g on notch fracture toughness of Pd-based thin-film metallic glass for MEMS applications, *Scr. Mater.* 54 (2006) 897–901. <https://doi.org/10.1016/J.SCRIPTAMAT.2005.10.072>.
- [144] N. Li, L. Liu, Q. Chen, J. Pan, K.C. Chan, The effect of free volume on the deformation behaviour of a Zr-based metallic glass under nanoindentation, *J. Phys. D. Appl. Phys.* 40 (2007) 6055. <https://doi.org/10.1088/0022-3727/40/19/043>.
- [145] X.K. Xi, D.Q. Zhao, M.X. Pan, W.H. Wang, Y. Wu, J.J. Lewandowski, Fracture of Brittle Metallic Glasses: Brittleness or Plasticity, (n.d.). <https://doi.org/10.1103/PhysRevLett.94.125510>.
- [146] M. Ghidelli, S. Gravier, J.J. Blandin, J.P. Raskin, F. Lani, T. Pardoen, Size-dependent failure mechanisms in ZrNi thin metallic glass films, *Scr. Mater.* 89 (2014) 9–12. <https://doi.org/10.1016/J.SCRIPTAMAT.2014.06.011>.
- [147] T. Burgess, M. Ferry, Nanoindentation of metallic glasses, *Mater. Today.* 12 (2009) 24–32. [https://doi.org/10.1016/S1369-7021\(09\)70039-2](https://doi.org/10.1016/S1369-7021(09)70039-2).
- [148] R.K. Gupta, N. Birbilis, The influence of nanocrystalline structure and processing route on corrosion of stainless steel: A review, *Corros. Sci.* 92 (2015) 1–15. <https://doi.org/10.1016/J.CORSCI.2014.11.041>.

- [149] N. Jadhav, V.J. Gelling, Review—The Use of Localized Electrochemical Techniques for Corrosion Studies, *J. Electrochem. Soc.* 166 (2019) C3461–C3476. <https://doi.org/10.1149/2.0541911jes>.
- [150] J.E. Greene, Review Article: Tracing the recorded history of thin-film sputter deposition: From the 1800s to 2017, *J. Vac. Sci. Technol. A Vacuum, Surfaces, Film.* 35 (2017) 05C204. <https://doi.org/10.1116/1.4998940>.

Appendix. Literature review

This is a list of the studies included in the literature review summarized in Section 6.1.3. of the thesis. The review aimed to compile all available studies on magnetron sputtered coating in the two largest families of multicomponent alloys (MCAs): the refractory metal MCAs and the 3d transition metal MCAs. It was last updated in March 2021.

The tables display different alloy compositions, any heating during deposition, the as-deposited phases, and any annealing and its resulting phases. Some studies included multiple compositions, which are then recorded as different alloys in the tables. When a combinatorial approach was used, there was no clear separation between different compositions. In these studies, the compositions that yielded different phase compositions were registered as separate cases. For instance, in ref [3], the compositional gradient yielded fcc, bcc, or fcc+bcc depending on the Al-content. This study thus counts as three cases. When several substrate temperatures were evaluated, these are separated by commas in the ‘Substrate heating’ column, and the resulting phases are separated in the same way under ‘As-deposited phases’. A limitation of the review is that very few studies reported the resulting temperature of the substrate when no heating was applied. In ref [7] there was no active heating, but the temperature was 170-280 °C. This is higher than in some of the cases with active heating.

Appendix Table 1. Compilation of magnetron sputtered multicomponent alloys of the 3d transition metal group.

| Materials system | Substrate heating | As-deposited phases | Annealing | Ref |
|------------------|-------------------|---------------------|-----------|-----|
| AlCoCrCuFe | No heating | fcc | | [1] |
| AlCoCrCuFeMn | No heating | fcc | | [2] |
| AlCoCrCuFeNi | -100 °C - RT | fcc | | [3] |
| AlCoCrCuFeNi | -100 °C - RT | fcc + bcc | | [3] |
| AlCoCrCuFeNi | -100 °C - RT | bcc | | [3] |
| AlCoCrCuFeNi | No heating | fcc | | [4] |

Appendix Table 1. Continued.

| Materials system | Substrate heating | As-deposited phases | Annealing | Ref |
|-------------------------|------------------------------------|-------------------------------|--|------------|
| AlCoCrCuFeNi | No heating | fcc+bcc | 100-800 °C, time not specified. Decomposition to AlCr-rich inter-metallics | [5] |
| AlCoCrCuFeNi | No heating | fcc | 100-800 °C, time not specified. Decomposition from 700 °C + reaction with substrate | [5] |
| AlCoCrCuFeNi | 250 °C | fcc + bcc | | [6] |
| AlCoCrCuFeNiV | No heating (170 °C – 280 °C) | fcc + bcc | | [7] |
| AlCoCrCuNi | No heating | fcc | | [1] |
| AlCoCrFeNi | No heating | fcc | | [8] |
| AlCoCrFeNi | No heating | fcc + B2 | | [9,10] |
| AlCoCuFeNi | No heating | bcc | | [1] |
| AlCoFeNiTiZr | No heating | fcc | | [11] |
| AlCrFeNiTi | No heating, 175 °C, 240 °C, 500 °C | amorphous, bcc, bcc, bcc + B2 | Amorphous films annealed 500-1000 °C, 15 °C /min Decomposition to bcc, B2, L2 ₁ | [12] |
| CoCrCuFeGeNi | No heating | amorphous | | [13] |
| CoCrCuFeInNi | No heating | amorphous | | [13] |
| CoCrCuFeMn | No heating | bcc | | [1] |
| CoCrCuFeNbNi | No heating | fcc | | [14,15] |
| CoCrCuFeNi | No heating | fcc | | [16] |
| CoCrCuFeNi | No heating | fcc | | [14,17] |
| CoCrCuFeNi | No heating | fcc | 800 °C for 1 h Decomposition to fcc + bcc | [18] |
| CoCrCuMnNi | No heating | fcc | | [1] |
| CoCrFeMnNi | No heating | fcc | | [19] |
| CoCrFeMnNi | No heating | fcc + hcp | | [20] |
| CoCrFeMnNi | No heating | fcc | 350 °C for 1 h Decomposition to fcc + bcc + L10 + σ phase | [21] |

Appendix Table 1. Continued.

| Materials system | Substrate heating | As-deposited phases | Annealing | Ref |
|-------------------------|--------------------------|--|--|------------|
| CoCrFeMnNi | No heating | fcc | | [22] |
| CoCrFeMnNi | No heating | fcc + bcc | | [23] |
| CoCrFeMnNi | No heating | fcc | | [24] |
| CoCrFeMnNi | No heating | amorphous | 300 °C and 450 °C for 1 h Formation of fcc grains | [25] |
| CoCrFeNi | No heating | fcc | | [26,27] |
| CoCuFeMnNi | No heating | 2 fcc phases + unidentified phase(s) | | [28] |
| CoFeNbNi | No heating | fcc + C15 Laves | | [29] |
| CrCuFeMoNi | No heating | fcc | | [30] |

Appendix Table 2. Compilation of magnetron sputtered multicomponent alloys of the refractory metal group.

| Materials system | Substrate heating | As-deposited phases | Annealing | Ref |
|------------------|------------------------------|---|---|------|
| AlCrMoTiV | No heating, 250 °C, 350 °C | bcc, bcc, bcc | | [31] |
| CrHfNbTaTiZr | No heating (170 °C – 280 °C) | bcc + C14 Laves | 1000-1000 °C for 2 h No phase change | [7] |
| CrNbTaTiW | 300 °C | bcc | | [32] |
| CrTaVW | No heating | bcc | 900 °C in situ TEM, time not specified No phase change | [33] |
| HfNbTaTiZr | No heating | amorphous | | [34] |
| HfNbTiVZr | No heating, 275 °C, 450 °C | amorphous, bcc, bcc+C14/C15 Laves | | [35] |
| HfNbTaZr | 25 °C, 500 °C, 700 °C | amorphous, amorphous, bcc + β phase | | [36] |
| MoNbTaW | No heating | bcc | 800 °C for 2 h No phase change | [37] |
| MoNbTaW | No heating | bcc | 1000 °C for 3 days No phase change | [38] |
| MoNbTaVW | 100 °C | bcc | Annealing in air bcc remains to 500 °C Thereafter oxidation | [39] |
| MoNbTaVW | 100 °C | bcc | Annealing in air bcc remains to 400 °C Thereafter oxidation | [40] |
| NbTaTiW | 20 °C | bcc | 700 °C for 90 min No phase change | [41] |
| NbTaTiVZr | No heating (170 °C – 280 °C) | bcc | | [7] |

Included studies

- [1] S.A. Kube, S. Sohn, D. Uhl, A. Datye, A. Mehta, J. Schroers, Phase selection motifs in High Entropy Alloys revealed through combinatorial methods: Large atomic size difference favors bcc over fcc, *Acta Mater.* 166 (2019) 677–686. <https://doi.org/10.1016/j.actamat.2019.01.023>.
- [2] X. Li, Z. Zheng, D. Dou, J. Li, Microstructure and properties of coating of FeAlCuCrCoMn high entropy alloy deposited by direct current magnetron sputtering, *Mater. Res.* 19 (2016) 802–806. <https://doi.org/10.1590/1980-5373-MR-2015-0536>.
- [3] B.R. Braeckman, F. Boydens, H. Hidalgo, P. Dutheil, M. Jullien, A.L. Thomann, D. Depla, High entropy alloy thin films deposited by magnetron sputtering of powder targets, *Thin Solid Films.* 580 (2015) 71–76. <https://doi.org/10.1016/j.tsf.2015.02.070>.
- [4] T.K. Chen, M.S. Wong, T.T. Shun, J.W. Yeh, Nanostructured nitride films of multi-element high-entropy alloys by reactive DC sputtering, *Surf. Coatings Technol.* 200 (2005) 1361–1365. <https://doi.org/10.1016/j.surfcoat.2005.08.081>.
- [5] V. Dolique, A.L. Thomann, P. Brault, Y. Tessier, P. Gillon, Thermal stability of AlCoCrCuFeNi high entropy alloy thin films studied by in-situ XRD analysis, *Surf. Coatings Technol.* 204 (2010) 1989–1992. <https://doi.org/10.1016/j.surfcoat.2009.12.006>.
- [6] N.A. Khan, B. Akhavan, H. Zhou, L. Chang, Y. Wang, L. Sun, M.M. Bilek, Z. Liu, High entropy alloy thin films of AlCoCrCu_{0.5}FeNi with controlled microstructure, *Appl. Surf. Sci.* 495 (2019). <https://doi.org/10.1016/j.apsusc.2019.143560>.
- [7] V.F. Gorban', R.A. Shaginyan, N.A. Krapivka, S.A. Firstov, N.I. Danilenko, I. V. Serdyuk, Superhard Vacuum Coatings Based on High-Entropy Alloys, *Powder Metall. Met. Ceram.* 54 (2016) 725–730. <https://doi.org/10.1007/s11106-016-9767-2>.
- [8] L. Gao, W. Liao, H. Zhang, J.U. Surjadi, D. Sun, Y. Lu, Microstructure, mechanical and corrosion behaviors of CoCrFeNiAl 0.3 High Entropy Alloy (HEA) films, *Coatings.* 7 (2017). <https://doi.org/10.3390/coatings7100156>.
- [9] W.B. Liao, H. Zhang, Z.Y. Liu, P.F. Li, J.J. Huang, C.Y. Yu, Y. Lu, High strength and deformation mechanisms of Al_{0.3}CoCrFeNi high-entropy alloy thin films fabricated by magnetron sputtering, *Entropy.* 21 (2019). <https://doi.org/10.3390/e21020146>.
- [10] W. Liao, S. Lan, L. Gao, H. Zhang, S. Xu, J. Song, X. Wang, Y. Lu, Nanocrystalline high-entropy alloy (CoCrFeNiAl_{0.3}) thin-film coating by magnetron sputtering, *Thin Solid Films.* 638 (2017) 383–388. <https://doi.org/10.1016/j.tsf.2017.08.006>.

- [11] J. na Liu, Z. guo Xing, H. dou Wang, X. fang Cui, G. Jin, B. shi Xu, Microstructure and fatigue damage mechanism of Fe–Co–Ni–Al–Ti–Zr high-entropy alloy film by nanoscale dynamic mechanical analysis, *Vacuum*. 159 (2019) 516–523. <https://doi.org/10.1016/j.vacuum.2018.10.061>.
- [12] A. Marshal, P. Singh, D. Music, S. Wolff-Goodrich, S. Evertz, A. Schökel, D.D. Johnson, G. Dehm, C.H. Liebscher, J.M. Schneider, Effect of synthesis temperature on the phase formation of NiTiAlFeCr compositionally complex alloy thin films, *J. Alloys Compd.* 854 (2021) 155178. <https://doi.org/10.1016/j.jallcom.2020.155178>.
- [13] B.R. Braeckman, F. Misják, G. Radnóczy, D. Depla, The influence of Ge and In addition on the phase formation of CoCrCuFeNi high-entropy alloy thin films, *Thin Solid Films*. 616 (2016) 703–710. <https://doi.org/10.1016/j.tsf.2016.09.021>.
- [14] B.R. Braeckman, D. Depla, Structure formation and properties of sputter deposited Nb_x-CoCrCuFeNi high entropy alloy thin films, *J. Alloys Compd.* 646 (2015) 810–815. <https://doi.org/10.1016/j.jallcom.2015.06.097>.
- [15] B.R. Braeckman, F. Misják, G. Radnóczy, M. Caplovicová, P. Djemia, F. Tétard, L. Belliard, D. Depla, The nanostructure and mechanical properties of nanocomposite Nb_x-CoCrCuFeNi thin films, *Scr. Mater.* 139 (2017) 155–158. <https://doi.org/10.1016/j.scriptamat.2017.06.046>.
- [16] Z. An, H. Jia, Y. Wu, P.D. Rack, A.D. Patchen, Y. Liu, Y. Ren, N. Li, P.K. Liaw, Solid-solution CrCoCuFeNi high-entropy alloy thin films synthesized by sputter deposition, *Mater. Res. Lett.* 3 (2015) 203–209. <https://doi.org/10.1080/21663831.2015.1048904>.
- [17] B.R. Braeckman, P. Djemia, F. Tétard, L. Belliard, D. Depla, Impurity-controlled film growth and elastic properties of CoCrCuFeNi thin films, *Surf. Coatings Technol.* 315 (2017) 475–483. <https://doi.org/10.1016/j.surfcoat.2017.03.014>.
- [18] Y. Ma, G.J. Peng, D.H. Wen, T.H. Zhang, Nanoindentation creep behavior in a CoCrFeCuNi high-entropy alloy film with two different structure states, *Mater. Sci. Eng. A*. 621 (2015) 111–117. <https://doi.org/10.1016/j.msea.2014.10.065>.
- [19] S. Fang, C. Wang, C.L. Li, J.H. Luan, Z.B. Jiao, C.T. Liu, C.H. Hsueh, Microstructures and mechanical properties of CoCrFeMnNiV_x high entropy alloy films, *J. Alloys Compd.* 820 (2020) 153388. <https://doi.org/10.1016/j.jallcom.2019.153388>.
- [20] C. Sha, Z. Zhou, Z. Xie, P. Munroe, High entropy alloy FeMnNiCoCr coatings: Enhanced hardness and damage-tolerance through a dual-phase structure and nanotwins, *Surf. Coatings Technol.* 385 (2020) 125435. <https://doi.org/10.1016/j.surfcoat.2020.125435>.
- [21] Y.J. Li, A. Savan, A. Kostka, H.S. Stein, A. Ludwig, Accelerated atomic-scale exploration of phase evolution in compositionally complex materials, *Mater. Horizons*. 5 (2018) 86–92. <https://doi.org/10.1039/c7mh00486a>.

- [22] A. Kauffmann, M. Stüber, H. Leiste, S. Ulrich, S. Schlabach, D.V. Szabó, S. Seils, B. Gorr, H. Chen, H.J. Seifert, M. Heilmaier, Combinatorial exploration of the High Entropy Alloy System Co-Cr-Fe-Mn-Ni, *Surf. Coatings Technol.* 325 (2017) 174–180. <https://doi.org/10.1016/j.surfcoat.2017.06.041>.
- [23] C. Dang, J.U. Surjadi, L. Gao, Y. Lu, Mechanical Properties of Nanostructured CoCrFeNiMn High-Entropy Alloy (HEA) Coating, *Front. Mater.* 5 (2018) 1–6. <https://doi.org/10.3389/fmats.2018.00041>.
- [24] Y.-C. Hsu, C.-L. Li, C.-H. Hsueh, Effects of Al Addition on Microstructures and Mechanical Properties of CoCrFeMnNiAl_x High Entropy Alloy Films, *Entropy*. 22 (2019) 2. <https://doi.org/10.3390/e22010002>.
- [25] L.L. Xiao, Z.Q. Zheng, S.W. Guo, P. Huang, F. Wang, Ultra-strong nanostructured CrMnFeCoNi high entropy alloys, *Mater. Des.* 194 (2020) 108895. <https://doi.org/10.1016/j.matdes.2020.108895>.
- [26] W. Huo, F. Fang, X. Liu, S. Tan, Z. Xie, J. Jiang, Remarkable strain-rate sensitivity of nanotwinned CoCrFeNi alloys, *Appl. Phys. Lett.* 114 (2019) 101904. <https://doi.org/10.1063/1.5088921>.
- [27] W. Huo, F. Fang, X. Liu, S. Tan, Z. Xie, J. Jiang, Fatigue resistance of nanotwinned high-entropy alloy films, *Mater. Sci. Eng. A.* 739 (2019) 26–30. <https://doi.org/10.1016/j.msea.2018.09.112>.
- [28] A. Akbari, T.J. Balk, Combinatorial thin film screening to identify single-phase, non-equiatomic high entropy alloys in the MnFeCoNiCu system, *MRS Commun.* 9 (2019) 750–755. <https://doi.org/10.1557/mrc.2019.53>.
- [29] J.Y. Zhang, Z.Y. Ding, F.C. Li, Y. Yang, Controlled synthesis of nanostructured glassy and crystalline high entropy alloy films, *Nanotechnology*. 31 (2020) 045601. <https://doi.org/10.1088/1361-6528/AB4A41>.
- [30] Q.S. Chen, C.H. Liu, J.P. Long, J. Wang, R.Q. Zhang, H.Y. Yang, W. Zhang, F.Y. Yao, S. Zhao, Q. Zhang, Microstructure and corrosion characteristics of CrCuFeMoNi HEA coatings with different compositions in high-temperature and high-pressure water, *Mater. Res. Express*. 6 (2019). <https://doi.org/10.1088/2053-1591/ab19ed>.
- [31] R. Chen, Z. Cai, J. Pu, Z. Lu, S. Chen, S. Zheng, C. Zeng, Effects of nitriding on the microstructure and properties of VAlTiCrMo high-entropy alloy coatings by sputtering technique, *J. Alloys Compd.* 827 (2020) 153836. <https://doi.org/10.1016/j.jallcom.2020.153836>.
- [32] S. Fritze, P. Malinovskis, L. Riekehr, L. von Fieandt, E. Lewin, U. Jansson, Hard and crack resistant carbon supersaturated refractory nanostructured multicomponent coatings, *Sci. Rep.* 8 (2018) 1–8. <https://doi.org/10.1038/s41598-018-32932-y>.
- [33] O. El-Atwani, N. Li, M. Li, A. Devaraj, J.K.S. Baldwin, M.M. Schneider, D. Sobieraj, J.S. Wróbel, D. Nguyen-Manh, S.A. Maloy, E. Martinez, Outstanding radiation resistance of tungsten-based high-entropy alloys, *Sci. Adv.* 5 (2019) eaav2002. <https://doi.org/10.1126/sciadv.aav2002>.

- [34] N. Tüten, D. Canadinc, A. Motallebzadeh, B. Bal, Microstructure and tribological properties of TiTaHfNbZr high entropy alloy coatings deposited on Ti–6Al–4V substrates, *Intermetallics*. 105 (2019) 99–106. <https://doi.org/10.1016/j.intermet.2018.11.015>.
- [35] S. Fritze, C.M. Koller, L. von Fieandt, P. Malinovskis, K. Johansson, E. Lewin, P.H. Mayrhofer, U. Jansson, Influence of deposition temperature on the phase evolution of HfNbTiVZr high-entropy thin films, *Materials* (Basel). 12 (2019) 10–17. <https://doi.org/10.3390/ma12040587>.
- [36] B. Song, Y. Li, Z. Cong, Y. Li, Z. Song, J. Chen, Effects of deposition temperature on the nanomechanical properties of refractory high entropy TaNbHfZr films, *J. Alloys Compd.* 797 (2019) 1025–1030. <https://doi.org/10.1016/j.jallcom.2019.05.121>.
- [37] X. Feng, J. Zhang, Z. Xia, W. Fu, K. Wu, G. Liu, J. Sun, Stable nanocrystalline NbMoTaW high entropy alloy thin films with excellent mechanical and electrical properties, *Mater. Lett.* 210 (2018) 84–87. <https://doi.org/10.1016/j.matlet.2017.08.129>.
- [38] Y. Zou, J.M. Wheeler, H. Ma, P. Okle, R. Spolenak, Nanocrystalline High-Entropy Alloys: A New Paradigm in High-Temperature Strength and Stability, *Nano Lett.* 17 (2017). <https://doi.org/10.1021/acs.nanolett.6b04716>.
- [39] S.B. Hung, C.J. Wang, Y.Y. Chen, J.W. Lee, C.L. Li, Thermal and corrosion properties of V-Nb-Mo-Ta-W and V-Nb-Mo-Ta-W-Cr-B high entropy alloy coatings, *Surf. Coatings Technol.* 375 (2019) 802–809. <https://doi.org/10.1016/j.surfcoat.2019.07.079>.
- [40] Y.Y. Chen, S.B. Hung, C.J. Wang, W.C. Wei, J.W. Lee, High temperature electrical properties and oxidation resistance of V-Nb-Mo-Ta-W high entropy alloy thin films, *Surf. Coatings Technol.* 375 (2019) 854–863. <https://doi.org/10.1016/j.surfcoat.2019.07.080>.
- [41] X. Feng, G. Tang, L. Gu, X. Ma, M. Sun, L. Wang, Preparation and characterization of TaNbTiW multi-element alloy films, *Appl. Surf. Sci.* 261 (2012) 447–453. <https://doi.org/10.1016/j.apsusc.2012.08.030>.

Acta Universitatis Upsaliensis

*Digital Comprehensive Summaries of Uppsala Dissertations
from the Faculty of Science and Technology 2222*

Editor: The Dean of the Faculty of Science and Technology

A doctoral dissertation from the Faculty of Science and Technology, Uppsala University, is usually a summary of a number of papers. A few copies of the complete dissertation are kept at major Swedish research libraries, while the summary alone is distributed internationally through the series Digital Comprehensive Summaries of Uppsala Dissertations from the Faculty of Science and Technology. (Prior to January, 2005, the series was published under the title "Comprehensive Summaries of Uppsala Dissertations from the Faculty of Science and Technology".)

Distribution: publications.uu.se
urn:nbn:se:uu:diva-489916



ACTA
UNIVERSITATIS
UPSALIENSIS
UPPSALA
2023